



POLITECNICO
MILANO 1863

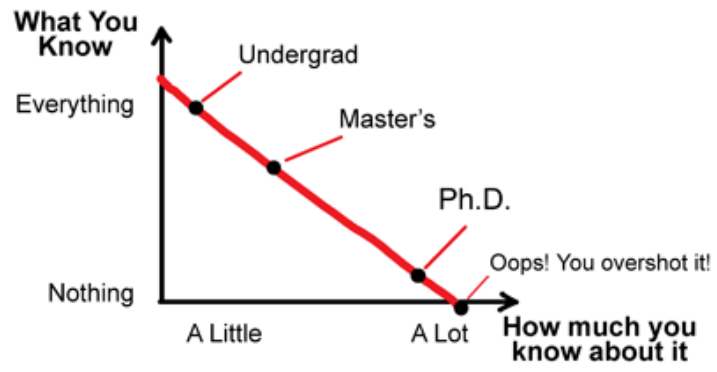
School of Industrial and Information Engineering
Laurea Magistrale (M.Sc.) in Engineering Physics

Reconfigurable integrated photonic circuits for quantum machine learning

Candidate:
Alberto Beccari
Student ID: 837923

Thesis advisor: **Dr. Roberto Osellame**
Co-advisor: **Dr. Andrea Crespi**

Academic year 2016/2017



Source: phdcomics.com

ABSTRACT

The field of machine learning consists of many techniques for learning and constructing models capable of interpreting and synthesizing unstructured data, as well as of performing new predictions. In the last few years, the possibility of developing and implementing machine learning algorithms on quantum computers and quantum devices has begun to be explored. Superior performances in terms of computational complexity with respect to classic formulations were indeed unequivocally discovered.

Recently, two quantum algorithms for Hamiltonian learning have been proposed, the first adopting *Quantum Likelihood Evaluation* (QLE) and the second employing *Interactive Quantum Likelihood Evaluation* (IQLE). These methods aim to infer a Hamiltonian model describing the observed dynamics of an unknown quantum system, borrowing heavily from the machine learning toolbox. A promising purpose of these procedures would be to provide a technique for validating the operation of quantum simulators and quantum gates, whose dynamics are expected to become eventually too complex to be reproduced with classical resources.

This thesis work deals with developing an integrated photonic platform to test experimentally these different Hamiltonian learning methods. Specifically, the platform consists of two integrated optics chips, that can be operated separately or in cascade, in which 5-modes multiport interferometers are inscribed by Femtosecond Laser Micromachining.

In both devices, 4 internal parameters can be actively controlled by operating thermo-optical phase shifters: a vast set of unitary transformations can be implemented in each reconfigurable optical circuit.

An extended characterization of the multiport interferometers is performed, revealing a behaviour faithful to the design specifications. The devices are currently ready to be used with quantum light, in order to test in-depth the two Hamiltonian learning algorithms.

RIASSUNTO

La disciplina del machine learning raccoglie numerose tecniche per l'apprendimento e la costruzione di modelli per interpretare e sintetizzare una collezione di dati preesistenti, ed effettuare nuove predizioni. Recentemente, le potenzialità di composizione ed implementazione di algoritmi di machine learning con dispositivi e computer quantistici hanno cominciato ad essere esplorate, rivelando in tutti i casi una superiore efficienza computazionale rispetto alle formulazioni classiche.

Due algoritmi di quantum machine learning per l'apprendimento di un modello Hamiltoniano descrittivo di un sistema quantistico incognito sono stati recentemente proposti. Le due procedure si distinguono in *Quantum Likelihood Evaluation* (QLE) ed *Interactive Quantum Likelihood Evaluation* (IQLE), in virtù della modalità di operazione del simulatore quantistico che richiedono. Un importante obiettivo di questi metodi è la validazione del funzionamento di simulatori e di circuiti quantistici, le cui dinamiche, si prospetta, diverranno in futuro troppo complesse per essere simulate con risorse classiche.

Scopo di questa tesi è dunque lo sviluppo di una piattaforma sperimentale per la dimostrazione delle diverse strategie di Hamiltonian learning. Il sistema si compone di due chip fotonici, che possono essere operati in serie o in parallelo, in cui sono stati realizzati interferometri a 5 modi, mediante la tecnica di scrittura di guide con laser a femtosecondi. I circuiti fotonici possono essere configurati dinamicamente grazie alla fabbricazione di 4 sfasatori termo-ottici, realizzati tramite altrettanti resistori d'oro, ricavati sulla superficie dei chip. Gli interferometri implementano una classe di trasformazioni unitarie sugli stati di luce classica e quantistica che vi vengono iniettati.

In una prima fase si è valutata, tramite simulazioni numeriche, la natura e la generalità della classe di trasformazioni unitarie che le quattro fasi riconfigurabili permettono di attuare. Successivamente, si è progettata nel dettaglio la geometria delle guide d'onda e degli sfasatori. Il processo di fabbricazione è stato poi ottimizzato per minimizzare l'influenza delle perdite di accoppiamento e propagazione. Una volta realizzati i circuiti fotonici riconfigurabili, sono state definite tecniche di caratterizzazione dei parametri interni e di calibrazione degli sfasatori termo-ottici.

I risultati di queste misure confermano il funzionamento dei circuiti fotonici in conformità alle previsioni e aprono la strada al loro utilizzo con luce quantistica. I dispositivi sono ora stati affidati al gruppo di ricerca in Ottica Quantistica dell'università "La Sapienza" (Roma), diretto dai Proff. Fabio Sciarrino e Paolo Mataloni, che realizza ed

opera le sorgenti di singoli fotoni necessarie alla dimostrazione degli algoritmi quantistici menzionati. Nel breve termine, i chip saranno predisposti per i primi esperimenti di Hamiltonian learning.

CONTENTS

1	SIMULATORS FOR QUANTUM MACHINE LEARNING	1
1.1	Photonic quantum simulators	2
1.1.1	Solving Schrödinger equation	2
1.1.2	Quantum chemistry	4
1.1.3	Quantum walks and tight-binding models	7
1.2	Quantum machine learning	11
1.2.1	Nearest neighbor classifier	13
1.2.2	Boosting	17
1.2.3	Hamiltonian learning	20
1.2.3.1	Bayesian inference	21
1.2.3.2	The likelihood function	22
1.2.3.3	Algorithm performance	26
1.2.3.4	Experimental demonstration	26
2	FEMTOSECOND LASER WAVEGUIDE INSCRIPTION	31
2.1	Overview	32
2.2	Femtosecond pulse interaction with dielectrics	33
2.3	Fabrication parameters	36
2.3.1	Focusing conditions	36
2.3.2	Writing configuration	37
2.3.3	Repetition rate	38
2.3.4	Other parameters	39
2.4	Photonic building blocks	39
2.4.1	Directional couplers	39
2.4.2	Mach-Zehnder interferometers	41
2.5	Integrated quantum photonics	43
3	MATERIALS AND METHODS	48
3.1	Waveguide inscription setup	49
3.1.1	General scheme	49
3.1.2	Laser source	50
3.1.3	Motion stages	51
3.2	Post-processing of the photonic chips	51
3.2.1	Glass polishing and cutting	51
3.2.2	Gold coating and resistor patterning	52
3.3	Characterization setups and techniques	54
3.3.1	Observation with optical microscope	54
3.3.2	Coupling coherent light into the devices	55
3.3.3	Losses measurement	56
3.3.4	Imaging of the mode profile	59

4	A PLATFORM FOR HAMILTONIAN LEARNING EXPERIMENTS	61
4.1	Motivation for the work	62
4.2	Reconfigurable unitary transformation	63
4.2.1	Interferometric layout	63
4.2.2	The set of accessible transformations	66
4.2.3	Approximation of a generic unitary matrix	70
4.3	Inverse evolution	72
4.3.1	Layout and symmetries	73
4.3.2	Simplification of the interferometric structure	74
5	ON-CHIP DIRECT AND INVERSE INTERFEROMETERS	78
5.1	Micromachining process and devices design	79
5.1.1	Waveguide inscription parameters	79
5.1.2	Directional coupler design	80
5.1.3	Integrated optical layout	83
5.1.4	Resistive heaters electrical design	86
5.1.5	Heaters arrangement and interconnection	88
5.2	Characterization of the integrated devices	98
5.2.1	Power distribution and beam splitter reflectances	98
5.2.2	Calibration of the internal phase shifters	102
5.2.3	Calibration of the connection phase shifters	106
5.2.4	Interfacing the chips	110
	Conclusions	112
A	BASIC QUANTUM INFORMATION CONCEPTS	113
B	INTEGRATED OPTICS PRINCIPLES AND COMPONENTS	118
	BIBLIOGRAPHY	123

LIST OF FIGURES

Figure 1	H ₂ molecule energy eigenvalues simulation . . .	6
Figure 2	Quantum walk probability distribution	8
Figure 3	Quantum walk implementation in integrated optics	9
Figure 4	3-nearest neighbors classification case	15
Figure 5	Quantum nearest neighbor algorithm logic structure	16
Figure 6	Growth of a classification tree on a two-dimensional feature space	18
Figure 7	IQLE circuital scheme	23
Figure 8	Backwards evolution and Loschmidt echo in a Lorentz gas	25
Figure 9	Experimental demonstration of Hamiltonian learning with a single parameter (Rabi frequency)	29
Figure 10	Processes of plasma creation by interaction between matter and femtosecond pulses	34
Figure 11	Longitudinal and transverse waveguide writing	37
Figure 12	Different directional coupler variants fabricated by FLM	42
Figure 13	Mach-Zehnder interferometers fabricated by FLM, and different ways to modulate the phase delay between the two arms	44
Figure 14	Keystone Integrated Quantum Photonics experiments with FLM	47
Figure 15	Waveguide inscription experimental setup . .	49
Figure 16	Picture of a reconfigurable chip with resistive heaters and new electrical connectors	53
Figure 17	Femtosecond laser-inscribed waveguide, top view	54
Figure 18	Methods for coupling coherent light inside photonic circuits	56
Figure 19	Figurative illustration of the different Hamiltonian learning configurations with the developed chips	63
Figure 20	Direct interferometer layout	64
Figure 21	Schemes for decomposing a unitary transformation with passive optical elements	68
Figure 22	Distance distribution studies for random unitary transformations	71

Figure 23	Distance growth with a variable number of controllable parameters	72
Figure 24	Inverse interferometer layout	73
Figure 25	Proof of the possibility of implementing an inverse transformation, by collapse of the interferometric structure	75
Figure 26	Directional coupler schematics, with the chosen geometrical parameters	81
Figure 27	Bending losses characterization	82
Figure 28	Reflectance studies on directional couplers with varying d and L	84
Figure 29	Integrated optical layout of the direct and inverse interferometers	85
Figure 30	$I - V$ characteristic curve of a resistive heater .	88
Figure 31	Straight and bent resistive heaters	91
Figure 32	Numerical studies of heater arrangements . .	92
Figure 33	Cross-sectional view of the interconnection phase shifters	94
Figure 34	Electric pads and resistors pattern for FLM . .	96
Figure 35	Pinout scheme	97
Figure 36	Reflectance characterization in the first chip . .	101
Figure 37	α calibration via optical power modulation . .	104
Figure 38	Experimental setup for interference fringes displacement observation	108
Figure 39	Far-field fringe pattern analysis	109
Figure 40	Photo of the characterization setup with both chips coupled in cascade	111
Figure 41	Bloch sphere representation of a qubit	114
Figure 42	Rectangular channel waveguide	118
Figure 43	Graphs of power modulation by evanescent coupling	121
Figure 44	Schematic layout of a directional coupler . . .	122

LIST OF TABLES

Table 2	Quantum nearest neighbor algorithm features	17
Table 3	Quantum boosting algorithm features	20
Table 4	Waveguide FLM parameters	81
Table 5	Resistances on the direct interferometer chip .	97
Table 6	Resistances on the inverse interferometer chip	97
Table 7	Power distribution out of the direct interferometer chip	99
Table 8	Power distribution out of the inverse interferometer chip	100
Table 9	Reconstructed beam splitter reflectances in the direct interferometer	102
Table 10	Reconstructed beam splitter reflectances in the inverse interferometer	102

RINGRAZIAMENTI

Paginetta faticosa ma doverosa...

Innanzitutto ringrazio il mio relatore, il Dr. Roberto Osellame, per avermi introdotto al mondo dell'ottica quantistica ed accolto all'interno del suo fantastico gruppo di ricerca, oltre che per essersi dimostrato pacato, equilibrato e sempre stimolante. Del gruppo di ricerca ovviamente devo i ringraziamenti più sinceri ad Andrea, per i suoi consigli preziosi scaturiti da un'esperienza apparentemente senza limiti, per le interminabili e proficue (per me) discussioni in laboratorio, e, non da ultimo, per un incredibile e puntuale lavoro di revisione di questa tesi. Ossequi a tutti i meravigliosi ragazzi con cui ho condiviso scrivanie e linee window/door in AQUA nell'ultimo anno; cronologicamente, Ruska, Simone A., Martina, Francesco, Simone P. Un plauso a Martina per aver assunto temporaneamente la mansione di coppiera ufficiale del weekly Traditional Tea. Menzione speciale anche al vetusto Giacomo e alle sue playlist estive, ad alto tasso di Carmen Consoli.

Impossibile rendere onore a tutti gli amici radunati o mantenuti in questi sei anni; fate dunque riferimento alla tabella 1, sapendo che senza di voi non ci sarebbe stato gusto.

	Università	Majno's	Erasmus	Paesello
Giammario	Ruska	Frigi	Camilla	Pera
Mike	Giacinto	Sberla	Ilona	Bosco
Aureglio	Thunder	Taba	Gaspër	Roffia
★Stella★	Carlo	Alphio	Julia	Shushu
Edohats	Perry		Aji	Fadi
Mavio	Beppe		Ben	Traldi
Barigazzi	Giada		Simone	Crastian
Chiara	<i>Tisi??</i>			Mich
<i>et al.</i>				

Tabella 1: Individui eccellenti

Grazie infinite ai miei genitori, che mi hanno supportato fin troppo in questi anni: non c'è modo di rendere onore, a parole, al vostro spirito di sacrificio e al silenzioso incoraggiamento che mi avete sempre offerto. Lo stesso vale per Ilaria e Daniele, che ultimamente hanno messo un sacco di carne al fuoco. Auguri!

PHOTONIC SIMULATORS FOR QUANTUM MACHINE LEARNING

This chapter is devoted to setting the background and describing the fundamental conceptual tools for the Hamiltonian learning experiment.

The first section reviews quantum simulators, specifically those implemented with photonic technologies, and the reasons why they cannot be efficiently realized with classical resources.

The chapter then goes on to describe how quantum computing has been recognized as a powerful framework in order to carry out learning tasks in an efficient way, and how its recurring paradigms are linked to the cardinal ideas in machine learning.

Finally, the main approaches to the problem of Hamiltonian learning will be briefly presented, and the deep connections with quantum machine learning methods and with quantum simulator certification will be explored.

1.1 PHOTONIC QUANTUM SIMULATORS

1.1.1 Solving Schrödinger equation

The field of quantum computation stems from a fundamental inadequacy of classical computers, famously pointed out by Richard Feynman in 1982 [1]. He proved that a classical, deterministic Turing machine would struggle enormously in simulating quantum mechanics and beyond a certain complexity, it would not be able to manage and represent, with reasonable temporal and spatial resources, the complex field central to all calculations in the theory, the wavefunction. The main reason for this conflict is the computational complexity of approximating a multivariate probability density function (which is the orthodox Born interpretation for the squared modulus of the wavefunction). A complete description of the probability of finding the system in a certain state needs the specification of the 3R coordinates $\vec{x}_1, \vec{x}_2, \dots, \vec{x}_R$ of the R particles involved. If the spatial region of interest for the quantum motion is discretized in N points, the wavefunction will have to take into account N^{3R} different configurations [1]. The scaling is therefore exponential, which renders the problem impossible to deal with beyond a certain size, in spite of technology advancements, without clever approximations that partially "decouple" the particle correlations.

Feynman himself proposed two alternative machines to successfully simulate Schrödinger equation: a *probabilistic* computer, capable of mapping the quantum system evolution from an initial to a final state to an internal transition undergone with the same probability, to sample statistically, and a *universal quantum simulator*, a quantum mechanical device over which we have full control, that can imitate the dynamics of every other discrete system with a finite number of degrees of freedom.

The latter was indeed the first task conceived for quantum computers: the simulation of quantum mechanics by approximation of the non-relativistic Schrödinger equation. The existence of such a speed-up with respect to classical Turing machines was subsequently formally proven. We will review in the following the simulation algorithm devised for a universal quantum computer [2].

In the single-particle, one-dimensional case, the spatial region of motion is discretized in 2^n intervals and represented by the Hilbert space of n *qubits* (see appendix A), encoding the presence or absence of the particle in each interval. In other words, the amplitudes of the computational basis vectors $|i\rangle$ stand for the simulated wavefunction ψ amplitude at the chosen discrete points.

$$|\tilde{\psi}(t)\rangle = \frac{1}{N} \sum_{i=0}^{2^n-1} \psi(x_i, t) |i\rangle, \quad (1)$$

where $N = \sqrt{\sum_i |\psi(x_i, t)|^2}$ is the normalization factor for ψ .

The Schrödinger equation is integrated formally by acting with the time evolution operator on the wavefunction along small time increments ϵ :

$$\psi(x, t + \epsilon) = e^{-\frac{i\epsilon}{\hbar}(\hat{T} + \hat{V}(x))} \psi(x, t) \quad (2)$$

where $\hat{T} = -\frac{\hbar^2}{2m} \frac{\partial^2}{\partial x^2}$ is the kinetic energy and $\hat{V}(x)$ the potential energy operator. Keeping the time increment small allows us to approximate the time evolution operator as the product of unitary matrices by discarding the higher powers of ϵ :

$$e^{-\frac{i\epsilon}{\hbar}(\hat{T} + \hat{V}(x))} \approx e^{-\frac{i\epsilon}{\hbar} \hat{T}} e^{-\frac{i\epsilon}{\hbar} \hat{V}(x)}, \quad (3)$$

which is generally wrong as \hat{T} and \hat{V} do not commute. This key passage simplifies greatly the calculations, because \hat{T} and \hat{V} are separately diagonal in the k and x -representations, so their associated time evolutions are also trivially computed by evaluating the exponential of the eigenvalues. This requires to take the Fourier transform (\mathcal{F}) of the superposition state, for which an efficient quantum algorithm has been devised [3]: the application of \mathcal{F} switches the state with its k -space representation, while \mathcal{F}^{-1} brings it back to x -space. A generic time evolution can then be performed by repeatedly applying the unitary operator

$$\mathcal{F}^{-1} e^{i \frac{\hbar^2 k^2}{2m} \epsilon} \mathcal{F} e^{-\frac{i\epsilon}{\hbar} V(x)} \quad (4)$$

Simulation of the Schrödinger equation is therefore reduced to an implementation of the Fourier transform and phase shift gates of the form $|x\rangle \rightarrow e^{icf(x)} |x\rangle$, where c is a real constant. These are constructed by employing an ancillary qubit register, on which one evaluates a discretized version of $f(x)$, and rotations of the angles $c \cdot 2^j$ around the z -axis for any qubit j (see appendix A for reference about rotation operations).

This discussion shows that simulation of the dynamics of generic quantum systems is conveniently performed on a digital quantum simulator, illustrating how a universal quantum computer possesses the set of gates needed for the task. Furthermore, the resources needed to represent the wavefunction are exponentially fewer than those that must be deployed on a classical machine (the run-time grows as a polynomial in $1/\delta$, where δ is the desired error in approximating the time evolution [4]).

Nevertheless, at the current stage of quantum hardware maturity, only the simplest systems can be emulated reliably with a limited number of qubits [5]. In the following sections, we will consider

more specialized examples of quantum simulators implemented in photonic technology. Some of the quantum simulators presented in the following are *analog* in nature, mapping the system Hamiltonian to the surrogate simulator Hamiltonian in an analog fashion instead of using a discrete sequence of quantum operations, as was discussed in this section.

1.1.2 Quantum chemistry

The problem of accurately calculating the energy spectra of molecules and the band structures of solid-state materials is of crucial interest for chemistry and material science. It allows, for instance, to predict whether a certain chemical reaction would release or absorb energy, or to point out the physical properties of novel materials.

The most employed numerical methods include density functional theory and tractable correlated-electronic-structure techniques. The most severe limit to the numerical solution of Schrödinger equation is the exponential scaling of the computational complexity with the number of elements in the orbital basis set in which a solution is sought.

In 2005, a quantum algorithm [6], characterized by linear scaling of the number of qubits and fifth order scaling of the number of quantum gates with the number of basis functions, was introduced. The key principle of the procedure is the estimation of the phase accumulated by an eigenstate under the action of the molecular time evolution operator

$$e^{-\frac{i}{\hbar}\hat{H}t}|\Psi\rangle = e^{-\frac{i}{\hbar}Et}|\Psi\rangle = e^{-i\phi}|\Psi\rangle \quad (5)$$

therefore,

$$E = \frac{\hbar\phi}{t} \quad (6)$$

The specific implementation of the time evolution operator relies on the small-time-increment approximation (Trotter formula) described in section 1.1.1.

The simplest possible circuit for quantum chemistry calculations was successfully built and operated in 2009 [7]. The problem consisted in deriving the electronic energy spectrum of the hydrogen molecule in the Born-Oppenheimer approximation (decoupling nuclear and electronic motion) and using a basis set of six molecular orbitals. This particular task is very simplified by symmetry considerations, forbidding the mixing of all but few molecular orbitals, in such a way that the Hamiltonian is factorized in two 2-by-2 matrices and two scalar diagonal elements. The resulting two-dimensional

subspaces of the Hilbert space could be represented by a single qubit and the controlled unitary operators implemented by a sequence of single-qubit rotations. In this particular experiment, the bits appearing in the binary expansion of ϕ were determined by an iterative phase estimation algorithm, run multiple times in order to perform majority voting for extracting a more robust phase expansion. For larger molecules, more sophisticated error correction techniques would likely be needed, as the error probability would be compounded by the contributions of many more quantum gates. The experimental setup and a graph of the calculated energy eigenvalues of H_2 are reported in figure 1.

Simulation of more complex systems by the application of this phase estimation algorithm would require a scalable photonic architecture, capable of supporting a polynomially growing number of elementary gates. The mentioned demonstration was performed with discrete optical components; on the other hand, integrated photonic techniques offer a greater potential for increasing the experimental complexity with a tighter degree of control. Specifically, the possibility of decomposing [8] and implementing [9] generic unitary evolution operators in interferometric beam splitter arrays (*multiport arrays*) has been proven. In particular, the properties of quantum states of light can be manipulated through active phase shifters [10] [11] and reconfigurable circuits. Future work in this direction could result in a simpler and more robust alternative approximation of time evolution operators for energy eigenvalues derivation.

Another quantum chemistry algorithm has been devised and experimentally assessed with an integrated photonic device [12]: the *Quantum Variational Eigensolver* (QVE). The algorithm capitalizes on the variational principle for the time-invariant Schrödinger equation [13], stating that the ground-state wavefunction is the complex function that minimizes the *Rayleigh-Ritz quotient*; i. e.:

$$R = \frac{\langle \psi | \hat{H} | \psi \rangle}{\langle \psi | \psi \rangle} = \frac{\langle \hat{H} \rangle}{\langle \psi | \psi \rangle} \quad (7)$$

The optical circuit allowed the estimation of the expectation value $\langle \hat{H} \rangle$ over the prepared photon pair wavefunction and the result was handed to a classical computer to engage in a minimization routine. The computer evaluated the variations in the Rayleigh-Ritz quotient to decide the wavefunction to employ in the next algorithm iteration, and controlled the device reconfigurable phases in order to implement the state and choose the observable quantities to measure. The expectation value of the Hamiltonian was estimated by a linear decomposition over Pauli operators products; these could be implemented in the measurement step of the photonic device. The linear combination was performed out-of-chip, by the classical computer.

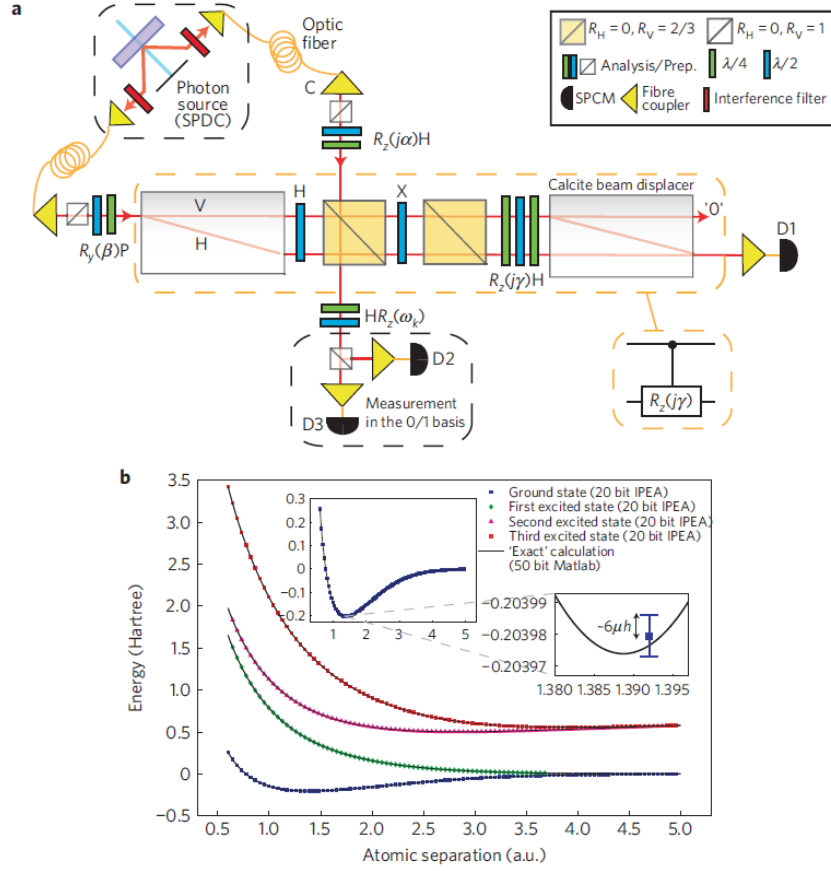


Figure 1: Quantum simulation experiment for estimating the energy of the hydrogen molecule in the minimal basis set. A pair of entangled photons generated via spontaneous parametric down-conversion implements an iterative phase-estimation scheme, where the register (R) photon represents a superposition state of two basis functions. The photons are manipulated via bulk beam splitters, $\frac{\lambda}{2}$ and $\frac{\lambda}{4}$ waveplates in order to implement single-qubit rotations around the Bloch axes (R_y and R_z), as well as Hadamard (H) and Pauli X gate operations. Coincident clicks of the single-photon counting modules herald a successful iteration, as well as produce an estimation for a single bit of the phase representation. Panel **b** shows the derived energy spectra as a function of the interatomic distance, calculated to 20 bits of discretization: a precision of 16 bits was sufficient in order to resolve energy differences relevant for chemical interactions. Image taken from [7].

The main advantage of QVE over the quantum phase estimation algorithm is that $\langle \hat{H} \rangle$ evaluation is performed by the application of few quantum gates to the candidate wavefunction: the products of Pauli operators can indeed be implemented in parallel. By contrast, the approximation of time evolution relying on the Trotter rule (section 1.1.1) requires typically a huge number of chained quantum operations and a low decoherence rate is necessary for simulation efficiency. Conversely, the most important disadvantage with respect to quantum phase estimation is the quadratically worse scaling of the total number of operations as a function of the desired precision δ (QPE requires $O(\delta^{-1})$ operations to extract the eigenvalue below an error of δ , whereas QVE requires $O(\delta^{-2})$ operations).

1.1.3 Quantum walks and tight-binding models

Quantum walks exhibit a completely different kind of probabilistic motion over a graph with respect to classic random walks: they cannot be related to the trajectory of a classical point particle but rather to the evolution of a wavefunction that can expand on a discrete set of sites, according to an internal degree of freedom (generally denoted as a *coin*, analogously to a coin toss that decides the direction to move along). Therefore, the motion will be affected by quantum interference due to the correlation between different positions, which will be removed only if a position measurement is performed. Indeed, measuring the position at each step of the quantum walk will collapse any correlation in the state, bringing the motion back to a classical random walk case.

Such an evolution can be formulated both in a discrete (step-wise) and continuous time framework. Here we concentrate on the discrete-time one.

The appropriate discrete time evolution operator that describes motion along a linear graph, in which each site is connected to its left and right neighbor, is:

$$\hat{U} = \hat{S} \cdot (\hat{C} \otimes \mathbb{1}) \quad (8)$$

This acts at first on the state of the coin degree of freedom only, with the operator \hat{C} , then performs a conditional translation in the position space according to the prescription:

$$\hat{S} = |\uparrow\rangle \langle \uparrow| \otimes \sum_i |i+1\rangle \langle i| + |\downarrow\rangle \langle \downarrow| \otimes \sum_i |i-1\rangle \langle i|, \quad (9)$$

displacing a state $|i\rangle$ to its right neighbor $|i+1\rangle$ when the coin faces up ($|\uparrow\rangle$) and conversely moving to the nearest left site when the coin

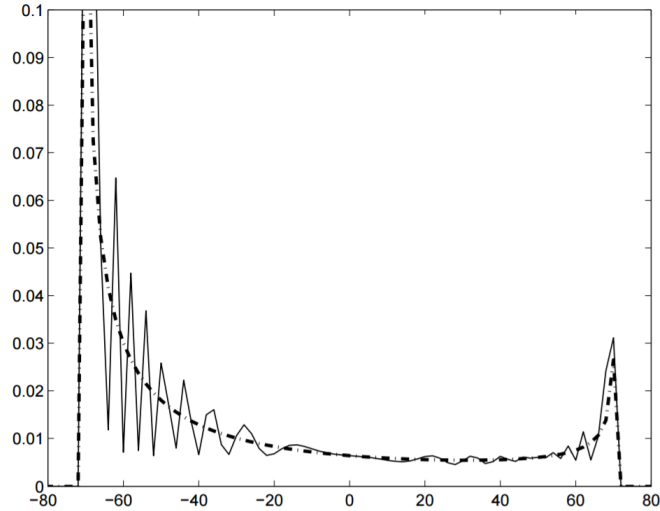


Figure 2: The simulated probability distribution of the quantum random walk with Hadamard coin and an initial state $|\downarrow\rangle \otimes |0\rangle$, after $T = 100$ steps. The probability at odd sites is not shown, as the wavefunction cannot occupy one of them during an even step. The dotted line keeps only the slowly-varying components of the distribution, showing clearly its bi-modal character. Image taken from [14].

points down. The "coin-flip" operator \hat{C} is very arbitrary, the possibilities leading to a vast family of walk behaviours; however the most commonly employed unitary evolution is the *single qubit Hadamard*

$$\hat{C} = \frac{1}{\sqrt{2}} \begin{pmatrix} 1 & 1 \\ 1 & -1 \end{pmatrix} \quad (10)$$

that leads to an unbiased $\frac{1}{2}/\frac{1}{2}$ distribution after the first step.

The probability distribution is strikingly different from the one describing a classical walker (in a classical lattice random walk, the object simply jumps to neighbouring sites according to some probability distribution). The propagation is quadratically faster: the distribution for the classical case approaches, after a high number of steps, a Gaussian function peaked on the starting position, with standard deviation $\sigma = \sqrt{T}$ (where T is the number of steps since the beginning of the random process), whereas it can be shown that the standard displacement of the quantum walker grows linearly with T . The probability distribution is not well described by a Gaussian profile, either: the pattern is intricate and asymmetric, presenting fast oscillations and a semi-uniform profile around the sites nearest to the starting position, and typically shows two maxima. All of these features are evident in figure 2.

Quantum walks with photons and coherent light have been realized in bulk optics and waveguides, although the latter allow a far

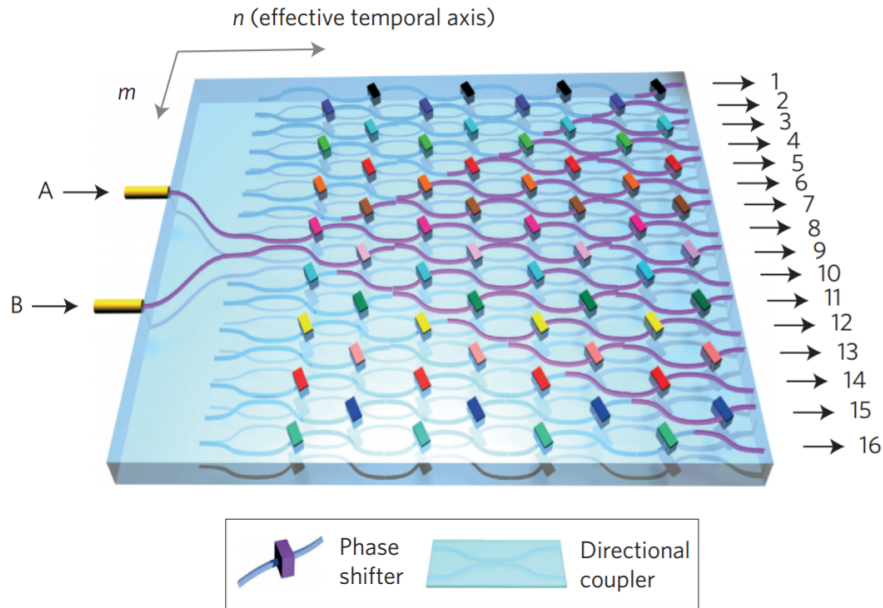


Figure 3: Scheme of a directional coupler network that implements an eight-step quantum walk. Following the horizontal axis in the rightwards direction corresponds to increasing the number of steps taken by the walker, while the 16 waveguides related to sites in the linear graph are discerned by moving in the vertical direction. The paths outlined in purple are those accessible to photons injected from the inputs A and B. Image taken from [15].

greater complexity, resulting in a higher number of sites and simulation steps: being enclosed in a monolithic device, they do not require an involved alignment procedure and permit a higher phase stability and control during propagation. In any of these two cases, the quantum walk is implemented as a cascade of beam splitters, arranged in a network of Mach-Zehnder interferometers. The beam splitter plays both roles of evolving the coin degree of freedom and enforcing the translation step, represented by the amplitudes for wavefunction propagation at the two output ports of the element.

If the quantum walk is implemented in a waveguide structure, beam splitters are usually replaced by a basic photonic building block, the *directional coupler*, a propagation tract where two waveguides are brought in close proximity, allowing power exchange to take place by evanescent field coupling. A complete analogy between a beam splitter, with generic reflectance and transmittance, and a directional coupler can be traced. A sketch of a waveguide and directional coupler array designed to perform a quantum walk is provided in figure 3.

Especially in the continuous-time version, the concept of quantum walk can be used to simulate tight-binding Hamiltonians, either as closed systems or under the influence of decoherence. In particu-

lar, they are used to study the transfer of excitations in biological macromolecules, where the coupling with the environment plays a significant role: it has been demonstrated that in certain classes of systems the transport efficiency can increase due to the dynamic interplay of the quantum walk Hamiltonian and of wavefunction dephasing introduced by environmental fluctuations. This is in contrast with purely coherent hopping, leading to localization in disordered systems [15]. The behaviour has been for instance studied in the Fenna–Matthews–Olson protein complex [16], in which each subunit has seven chlorophyll molecules spatially separated by several nanometers, as a prototype for larger photosynthetic energy transfer systems. The first simulation along these lines saw a single photon performing a six-step quantum walk in bulk optics, with tunable decoherence introduced by intentional misalignment of the beam displacers, allowing the observation of the transition from the quantum to a purely classic random walk regime [17].

A recent experiment [18] derived inspiration from these biological phenomena to study a walker travelling through a graph structured like a maze, and the efficiency of finding the exit node, both in a fully coherent stroll and with the addition of partial decoherence, indeed observing an efficiency improvement for a $p = 0.1$ rate of mixing with the environment. The simulation was performed in a three-dimensional array of waveguides fabricated with femtosecond laser inscription (which will be the subject of the following chapter); the dephasing noise was simulated by modulating the waveguide writing speed and its detuning to the neighboring ones.

Another effect that has been modeled and investigated with photonic quantum walks is *Anderson localization*: an absence of wave diffusion in disordered media. This interruption of matter and energy transport and wave localization happens in all sorts of environments described by a periodic potential, provided that a sufficient degree of randomness is added.

First formulated in the context of electronic motion in condensed matter systems, it was recognized as a general phenomenon of wave propagation and since observed for elastic waves, microwaves, photons, semiconductors, Bose-Einstein condensates, etc. In [15], the time evolution leading to Anderson localization was studied in a photonic quantum walk, with a static disorder term induced by a fixed deformation of the waveguide representing a given site in the graph, after each directional coupler tract. Additionally, the dependence of the localization properties on the symmetry of the initial walker wavefunction (bosonic, i.e. symmetric, or fermionic, i.e. antisymmetric) could be investigated by manipulating the entanglement of the photon pair injected in the interferometer.

1.2 QUANTUM MACHINE LEARNING

The concept of a quantum simulator, as described by Richard Feynman [1], was the seminal idea that made the quantum physics community wonder whether quantum mechanical systems could be useful for computation and solution of numerical problems, and which could be their specific advantages with respect to the already well-developed electronic calculators. In 1985 David Deutsch, borrowing from the intuitions of Feynman, described a *universal quantum computer* [19]. The notion of quantum simulator came full circle a decade later, when Lloyd proved that a universal quantum computer can be programmed to simulate efficiently any local quantum mechanical system [20].

The interest in the concept of quantum computer rose dramatically when a series of algorithm of high practical importance were proposed. The most important and influential ones are:

- *Grover search*, describing a method to look for a given item in an unordered dataset. The algorithm results in a quadratic speed-up with respect to the most efficient classical alternative. [21]
- *Shor's algorithm*, addressing the problem of factorizing an integer into prime numbers and converging to a solution with an exponential improvement in the number of operations with respect to the best known procedure running on classical computers [3]. The problem is of utmost practical interest, because many common cryptography schemes rely on the assumed inherent complexity of integer factoring for classical machines.

The main ideas underlying these quantum algorithms have become common routines and tools and were extended to many other algorithms, as will be described in the later parts of this section.

However, the experimental demonstration of a universal quantum computer with a significant advantage in performing such tasks is currently out of reach, due to several technological issues, e.g. limiting decoherence, performing efficient error correction and addressing individually a large number of qubits, that remain to be solved before the advantages of quantum computation can be exploited to their full extent. Nonetheless, the use of quantum hardware restricted to specific problems, without the claim of universal computation capabilities, is becoming feasible. In particular, it has recently been proven that the field of machine learning could benefit from the paradigms of quantum computation.

Machine learning is concerned with learning and constructing models from data. Typically, machine learning tasks are classified in two categories:

- In *supervised learning* a measurement outcome must be predicted as a function of a set of features; learning consists in

trying to adapt a model on a set of training observations in a way that allows to predict the outcome of future, unseen data instances with different feature values than the ones on which the model was trained, with an acceptable success rate.

- In *unsupervised* learning, only the features can be collected and characterized, and the task is to describe how the data are organized and clustered, often trying to separate them in different classes.

With respect to the nature of the measurement outcome or the learning feedback available to the algorithm, another distinction between machine learning tasks can be outlined, between:

- *classification* problems: data are divided into two or more discrete classes and the learner must construct a method to assign unseen inputs into one or more of these categories.
- *regression* problems: the output can span a continuous, rather than discrete, set of values.
- *clustering* problems: a set of inputs must be divided into groups. These classes are not known beforehand, therefore these problems belong to unsupervised learning.

Machine learning methods abundantly borrow their tools from the fields of statistics, linear algebra and constrained optimization: most learning procedures are mapped to the minimization of a multivariate function of the training data with respect to the choice of a decision model. This suggests the most immediate application of the quantum approach to learning problems: the tools of *adiabatic quantum computation* offer a rather physical procedure to minimize a multivariate function. The quantum system selected for implementing the computation is prepared in the ground state of a simple Hamiltonian, the function to minimize is mapped to a target Hamiltonian which can be imposed to the system and, finally, the Hamiltonian is evolved from the simple starting model to the target operator, as slowly as required by the adiabatic theorem (the timescale is proportional to the energy gap between ground and first excited state). It is then guaranteed that the system remains in the ground state of the instantaneous Hamiltonian that governs its dynamics. By choosing the target Hamiltonian model correctly, the final state of the system will encode the solution, the argument of the global minimum of the function thus implemented.

A forte of adiabatic quantum computation for optimization tasks is the possibility of running it on *non-convex* functions. Formulating a learning problem in terms of the optimization of a convex function is in general the preferred strategy in order to solve learning tasks,

as the solution will not sensibly depend on the initial guess, the algorithm cannot get stuck in a local optimum point and theoretical bounds on the convergence rate are easier to derive. However, non-convex formulations offer different advantages, being less sensitive to noise and outliers and at times granting better performance of the learned model on test data (i.e. data not belonging to the learning ensemble). Quantum algorithms reach the global optimum through physical evolution, in a completely different fashion from classical procedures (usually relying on gradient descent or iterative methods) therefore they are better suited to solve non-convex optimization problems.

Adiabatic quantum computation is not the only useful quantum paradigm for machine learning: quantum process tomography can be used to perform regression analysis and quantum neural networks, based on any physical implementation of a qubit, offer a useful level of abstraction. [22] The computational complexity advantage of quantum computation is also significant. Often, a polynomial improvement in the number of instructions to perform can be achieved, and an exponential speed-up over classical algorithms is available when it is acceptable to deal with quantum data both at the input and at the output of the computation. [23]

As a partial justification for the successful symbiosis between quantum computation and machine learning, we can remark that the framework of quantum mechanics, which combines probability theory and a natural geometric interpretation associated to the notion of Hilbert spaces, is indeed especially suitable and akin to the field of machine learning, that borrows many ideas from statistics and Euclidean geometry.

Several quantum machine learning algorithms have been described and physically demonstrated up to now, from a quantum implementation of neural networks [24], to handwriting recognition with a liquid-state nuclear magnetic resonance system implementing a quantum support vector machine [25], to a quantum classifier capable of labelling data instances with up to eight features [26].

In the following, we will expatiate on the quantum computational-theoretic concepts behind two machine learning algorithms devised to run on quantum systems: nearest neighbor classification and boosting. These two examples in particular show how machine learning tasks can be solved with vastly different quantum operations and protocols.

1.2.1 *Nearest neighbor classifier*

Nearest neighbor classification is an unstructured learning method: it is concerned with assigning an appropriate label in a discrete set of classes to previously unidentified data, without relying on the as-

sumption of any model. Therefore, the technique is not useful for understanding the nature of the relation between the features of data points and their consequent class, but by virtue of its *black-box* nature, its performance is among the best for real-world learning problems.

The algorithm concept is remarkably simple. Any data point is identified by a set of quantitative features, that can be collected in a vector \vec{x} . The training set consists of a list of examples of representative vectors coupled with their corresponding class. The assignment is performed by evaluating the *distance* of \vec{x} to each \vec{x}_r belonging to the training set, and identifying the k nearest data instances. The class is then chosen by a majority vote procedure, which simply amounts to picking the class which appears the most frequently between the k nearest neighbors.

It is naturally fundamental the choice of distance notion to employ in the learning problem. The Euclidean distance is frequently adopted; some implementations rely on adaptively changing the distance definition as learning progresses. In case some features are qualitative by nature, other kinds of definition must be tailored to the algorithm. Nearest neighbors classification is mainly successful in problems where each class is adequately sampled by the training set in the feature space. This is especially true when the geometric boundaries for discriminating between adjacent classes are very irregular, or when the learning paradigm can benefit from a simple classification criterion. An example of a classification problem approached with a Euclidean notion of distance is reported in figure 4.

A quantum algorithm for implementing nearest neighbor classification was proposed in 2014 [28]. The authors detail the exploitation of two possible notions of distance for assigning a class label to a data point: the conventional Euclidean distance and the *inner product* distance $|\vec{u} - \vec{v}|_{IP} = |\vec{u}||\vec{v}| - \vec{u} \cdot \vec{v}$, which produce exactly the same classification.

The algorithm leverages successfully the fact that training data sets are commonly representable as *sparse* vectors, i.e. vectors with a low number of nonzero components (features). If the input vectors do not contain more than d nonzero entries, the number of steps required to find the nearest neighbor will scale as $d^2 r_{\max}^4$, where r_{\max} denotes an upper bound on the maximum value which any vector component can take.

It is assumed that two *oracle* gates (that is, black box-like portions of the quantum algorithm circuit representation, whose implementation is not specified) can be constructed for the purpose of preparing the initial state for the minimum distance computation: an oracle \hat{O}

$$\hat{O} |j\rangle |i\rangle |0\rangle = |j\rangle |i\rangle |v_{ji}\rangle \quad (11)$$

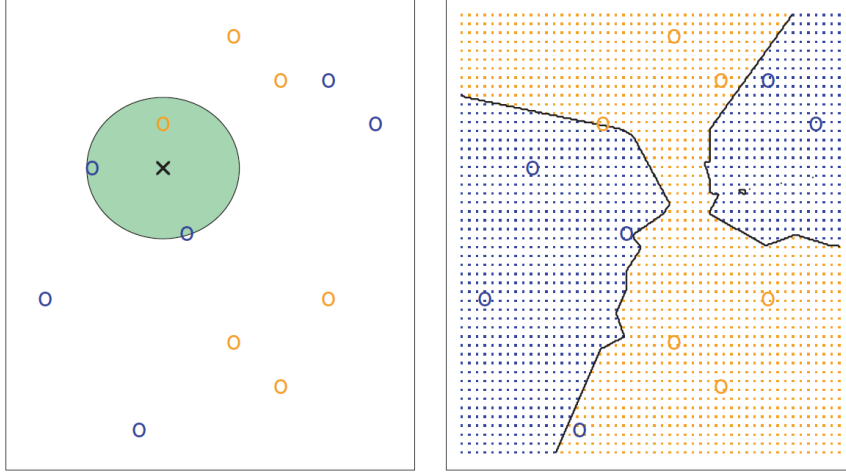


Figure 4: Three-nearest neighbors classification example, for two classes identified with the yellow and blue colours. The empty circles represent the data on which the learning method is trained. In the left figure, a data point marked with a black cross is assigned to the blue class, because two of its three nearest neighbors in the Euclidean distance are found to belong to it. In the right figure the boundaries for the assignment of any test point (coloured grids) based on the training set are shown. Image taken from [27].

to extract the i^{th} component of the training vector \vec{v}_j and to assign its value to a collection of ancillary qubits, and an oracle \hat{F}

$$\hat{F} |j\rangle |l\rangle = |j\rangle |f(j, l)\rangle \quad (12)$$

where $f(j, l)$ returns the location of the l^{th} nonzero entry in \vec{v}_j . The computational complexity is defined in terms of the number of queries to these two oracles in the algorithm, assuming that they dominate the overall run time.

The algorithm initially prepares the superposition state

$$\frac{1}{\sqrt{M}} \sum_{j=1}^M |j\rangle \left(\sqrt{1 - |\vec{v}_j - \vec{u}|} |0\rangle + \sqrt{|\vec{v}_j - \vec{u}|} |1\rangle \right) \quad (13)$$

where M is the number of training vectors, which can be obtained by multiple calls to the oracles and some single-qubit rotations (see appendix A for reference). The procedure differs according to which notion of distance is used to pick a class for the unlabeled vector \vec{u} . This state encodes the distance between the training vectors and \vec{u} , encoded indirectly in the amplitudes of the states $|j\rangle |1\rangle$.

The second step extracts the distance and stores it in the state of a qubit collection, by employing *amplitude amplification*, a broad technique in quantum computing that generalizes Grover search [21]. It consists in performing multiple rotations of the state vector in order to maximize the probability of having it belong to a desired subset

of the Hilbert space. In this case, the method is used to amplify the probability of measuring a 1 value for the last qubit listed in the state vector, i.e. to simplify the state to

$$\frac{1}{\sqrt{M}} \sum_{j=1}^M |j\rangle |\vec{v}_j - \vec{u}\rangle \quad (14)$$

Since no measurement has been performed yet, this provides a suitable initial state to run the *Dürr-Høyer minimization* algorithm [29], which probabilistically finds the minimum in an unsorted array of items, by exploiting Grover search as a subroutine. This finally delivers the index of the vector lying nearest to the unclassified data point, allowing to assign a suitable class label to it. The logical sequence describing the algorithm is recapped in figure 5.

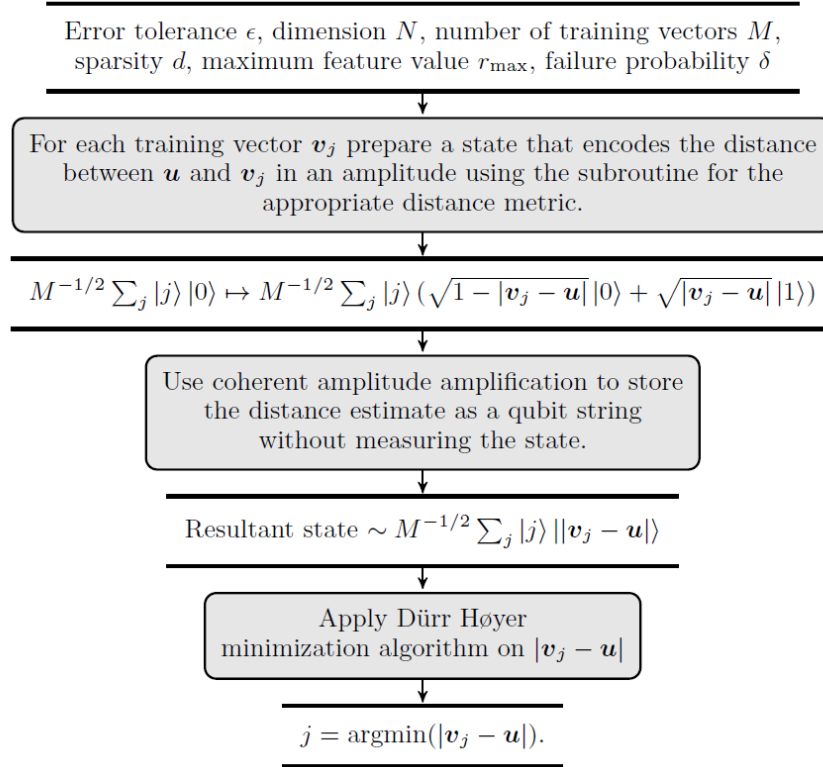


Figure 5: High level structure of the nearest neighbor quantum algorithm. The diagram is taken from [30].

The procedure can easily be generalized to a k-nearest neighbors classification logic by being run k times, removing each time the nearest training vector produced by the algorithm: in this case the class will be decided by a majority voting criterion. The Euclidean distance version of the algorithm naturally generalizes to a *centroid* classification scheme, where the new data are judged according to which class center of mass, $\sum_{j \in c} \vec{x}_j$, lies the nearest (the previous sum is run

only on training vectors belonging to class c). The advantage of this approach is however limited, as in real-world unsupervised learning tasks the classes are typically embedded in sets bounded by hyper-surfaces with a complex geometry, such that the sample centroid is not guaranteed to lie therein. The qualitative features of the quantum nearest neighbor algorithm are summarized in table 2.

Nearest neighbor algorithm	
Performance improvement	Quadratic
Other advantages	Exploitation of feature-sparse problems, complexity does not scale with feature number, noise robustness
Experimental demonstration	No

Table 2: Summary of the main features of the nearest neighbor algorithm. The performance improvement reported refers to the reduction in number of operations with respect to a competitor algorithm running on a classical computer. The last row reports whether the algorithm has already been implemented on a quantum machine.

An alternative take on nearest-neighbors classification consists in treating the centroid vectors as template states and trying to match the unknown state with the best template available, analogously to various forms of quantum state tomography [22]. The distance notion used to evaluate the degree of matching to a generic template is the state *fidelity*.

1.2.2 Boosting

Boosting is a powerful learning strategy for approaching both regression and classification problems. It combines the predictions of many weak, unreliable classifiers to produce a reliable "committee", capable of judging the class to which a data instance belongs with greatly improved success rate with respect to the performance of the single classifiers. Boosting learns a predictive model gradually, by fitting weak classifiers to the *residuals* of the current model, instead of fitting an excessively complex, multi-parameter model to the training set and risking overfitting, leading to an increase in the model variance and noise susceptibility. This way, the model is built and refined by iteratively compounding the derived weak classifiers and the following classifiers will rely on the information from previously extracted ones.

The weak classifiers contributing to the boosted model are typically regression or classification *trees*, which are among the simplest learning models ever devised: in the most common case, they prescribe

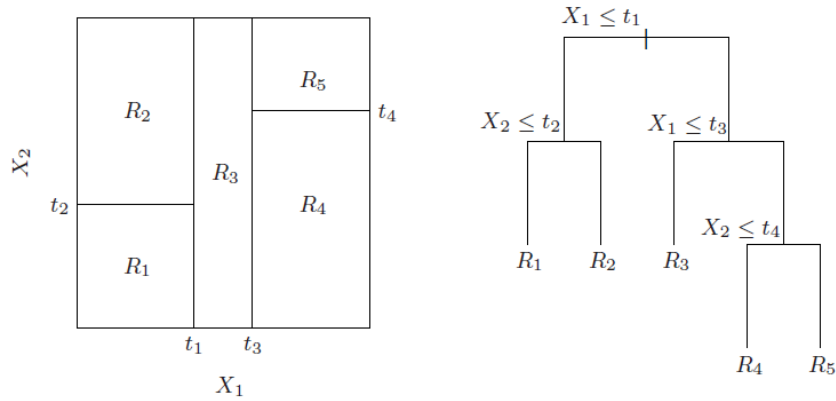


Figure 6: Partition of a two-dimensional feature space defined by growing a tree with 5 nodes on a given training set. The right panel shows a decision scheme representing such partition. Image taken from [31].

the partition of the feature space into a set of rectangles. Let us restrict our analysis to the description of a regression tree: the growth of a classification tree requires only a redefinition of the splitting criterion. Inside each rectangle the prediction is defined by the mean of the response of the training points that lie within, and the edges of rectangles, or the topology of the tree, are set by *greedy* minimization of the sum-of-squares fitting error (greedy algorithms make the optimal, local choice at each stage of an optimization task, never reconsidering the previous choices, hoping to approximate the optimal solution in a reasonable run-time. In this case, the edge of a rectangle is chosen by minimizing the sum-of-squares error and kept fixed for the successive partitioning steps, during which the outlined rectangles are split in the same way).

The complexity of the tree is usually defined through the number of subdomains, or *nodes* delineated at the end of the procedure. A key advantage of recursive trees lies in their interpretability: the fragmented topology of the feature space can be simply represented by a binary scheme such as the one reported in figure 6.

The most popular boosting algorithm, which we are going to describe in detail, is known as AdaBoost [32]. This algorithm prescribes an initially uniform weight for all the training observations; for each successive iteration $m = 2, 3, \dots, M$ the observational weights are individually modified based on the performance of the weak classifier extracted at the step $m - 1$, denoted by G_{m-1} : those observations that were misclassified will be assigned an increased weight; conversely the correctly classified observations will see a reduced weight. Thus, as the iteration proceeds, the observations that are difficult to classify will exert an ever increasing influence, forcing the subsequent classi-

fiers to focus on these in particular. The final model will combine the predictions from each tree through a weighted majority vote:

$$G(x) = \text{sign} \left(\sum_{m=1}^M w_m G_m(x) \right) \quad (15)$$

where the w_m coefficients, weighting each tree contributing to the boosted classifier, are computed by the algorithm in order to assign a greater influence to the trees with lower classification error on the (weighted) training set. The sign operation prescription is given since, in a binary classification problem, the two classes are generally represented via the ± 1 integers.

The weak classifiers employed in boosting methods are typically streamlined version of decision trees called *stumps*, with two nodes only. More complex tree variants, although requiring a more computationally intensive optimization, usually do not result in an improved classification success rate.

In the context of machine learning, a *loss function*, depending on the outcomes of the training data and the corresponding model predictions, is defined to encode some sort of cost associated to a misclassification, or mistaken prediction on behalf of the learner. A learning algorithm is usually related to minimization of a given cost function, which then results in the specification of its estimation parameters. The most common flavour of linear regression, for instance, arises from the minimization of the familiar sum of squared residuals. It was shown that the iteration step in the AdaBoost algorithm can be seen as the step-wise optimization of an exponential loss function

$$L(y, G(x)) = \sum_i \exp(-y_i G(x_i)) \quad (16)$$

producing the values of the training set and classifier weights to be used in the following fitting step.

The quantum algorithm that provides boosting of a set of weak learners arises from a different loss definition:

$$L = \left(\frac{1}{N} \sum_{i=1}^N \sum_{m=1}^M (w_m G_m(x_i) - y_i)^2 \right) + \lambda \|\vec{w}\| \quad (17)$$

where the w_m 's are still the target of the optimization procedure, and λ is a regularization term used to control the model *sparsity*, i.e. the number of weak classifiers contributing significantly to the final model and the resulting interpretability. The higher the number of simple classifiers, the more penalizing this term will become in the loss function. Classical results of theoretical statistical learning show that a sparser model generalizes better to new data instances, at equal

conditions on the training error. One could show that the regularization contribution λ makes the loss function *non-convex*, a situation that is generally avoided in machine learning because fast convergence to the minimum is not analytically guaranteed. However, adiabatic quantum computing can overcome this problem by its core working principle of an approximating Hamiltonian slowly converging to the objective function. Thus, it can benefit from the possibility, associated to non-convexity, of an exhaustive search in the parameter space, by-passing the risk of accepting a local minimum.

The problem of finding the w_m 's that minimize the loss function can be discretized and formulated in terms of *Quadratic Unconstrained Binary Optimization* (QUBO). This is a common pattern in machine learning that consists in finding the minimum of the quadratic form $\vec{x}^T Q \vec{x}$, where Q is a real matrix and the individual x_i 's are constrained to be either 0 or 1. This problem belongs to the NP-hard complexity class but, mapped to a Ising model, is well suited to be approached by simulated or quantum annealing. Adiabatic quantum computing plays the role of a minimization heuristic employed to find the optimal weights of the weak classifiers appearing in the model, at each step of the boosting iterative procedure.

The complete quantum algorithm will also update the weights assigned to the training observations according to the model classification performance and iterate over different values of the sparsity regularization parameter λ , and, once converged, will produce a classification model with the same form as previously described. The advantages provided by the quantum boosting algorithm are summarized in table 3.

Quantum boosting algorithm	
Performance improvement	Quadratic
Other advantages	Non-convexity, low bit depth, improved sparsity
Experimental demonstration	Yes

Table 3: Summary of the main features of the quantum boosting algorithm. The performance improvement reported refers to the reduction in number of operations with respect to a competitor algorithm running on a classical computer. The last row reports whether the algorithm has already been implemented on a quantum machine.

1.2.3 Hamiltonian learning

The field of quantum simulation has made great strides in the last years, encompassing many different physical platforms other than the photonic devices that were described in section 1.1 (superconducting

microwave resonators, liquid state nuclear magnetic resonance, ion traps, etc.). The behaviour of interacting quantum objects is so difficult to mimic on classical Turing machines that analog quantum simulators are approaching a regime that is challenging to access by supercomputers [33].

A major objection raised against the field is the doubt that quantum simulators could be untrustworthy and that the reliability of measured observables could be severely affected by disorder and noise [34]. The issue applies also to the task of quantum hardware validation: quantum computer scientists need tools to assess the operation of the gates used for complex computations and check their reliability against the tolerances imposed by fault-tolerant hardware architectures.

Recently, an algorithm for characterizing and validating Hamiltonian dynamics was proposed [35]. The procedure combines *Bayesian inference*, a vastly adopted technique in the field of statistical learning, and the operation of a trusted quantum simulator in order to infer iteratively the parameters of the Hamiltonian describing the dynamics of an uncertified quantum object.

1.2.3.1 Bayesian inference

Let us briefly review the Bayesian statistical inference method. This archetype and various related techniques have been broadly applied in various machine learning disciplines, such as pattern recognition, statistical classification and artificial intelligence [31]. The paradigm allows to update the probability of an initial hypothesis as more evidence or data supporting or contrasting with it are collected. The fundamental rule for probability updating is expressed in *Bayes' theorem* on conditional probability:

$$P(H|D) = \frac{P(D|H) \cdot P(H)}{P(D)} \quad (18)$$

To our intents, H is an initial hypothesis on the experimental conditions, whose probability can be affected by the data, and D is observed evidence.

$P(H)$ represents the *prior probability*, the probability that we assigned to our hypothesis before the outcome D was observed, and $P(D|H)$ is called *likelihood function*: it expresses the compatibility of the observed evidence D with the assumed hypothesis H and is derived by a stochastic model of the physical phenomenon. Finally, the left-hand side represents the *posterior probability*, or the updated probability for H after the evidence has been taken into account: equation 18, on the whole, provides a rule for assigning a probability to the initial hypothesis after it is checked against experimental data. Typically, $P(H|D)$ is adopted as a new prior probability for a following

inference run against newly-collected data: the legitimacy of the initial hypothesis is thus iteratively validated.

In practice, $P(D)$ is not directly estimated: the posterior probability is rather normalized as a final step of each iteration, by evaluating a set of mutually exclusive and exhaustive hypotheses H_1, H_2, \dots, H_M and considering the expansion

$$P(D) = \sum_{m=1}^M P(D|H_m) \cdot P(H_m) \quad (19)$$

Therefore, in order to update the probabilities of incompatible hypotheses, a set of weights is simply computed as $w_m = P(D|H_m) \cdot P(H_m)$ and their distribution is normalized to their sum.

Coming back to the specific case of Hamiltonian certification, we identify the incompatible hypotheses in Bayes' rule with different values of a collection of unknown parameters \vec{x} that determine the Hamiltonian inside a broad class:

$$H_m = \hat{H}(\vec{x}_m) \quad (20)$$

The procedure of updating from the prior distribution according to the experimental outcomes will output a (discretized) probability density function for \vec{x} , from which the experimenter can also extract the uncertainty in the identification of the final model for the untrusted quantum simulator.

1.2.3.2 The likelihood function

The most intricate step in Hamiltonian learning is providing a way to easily estimate the compatibility of a certain experimental outcome D (specifically, a quantum state) with the assumption of a set of values for the Hamiltonian parameters \vec{x}_i , called likelihood function in section 1.2.3.1. If the non-characterized quantum mechanical system was prepared in the initial state $|\psi\rangle$ and evolved under its peculiar Hamiltonian for a time t , the likelihood can be expressed as the squared projection

$$P(D|\vec{x}_i) = |\langle D | e^{-\frac{it}{\hbar} \hat{H}(\vec{x}_i)} |\psi\rangle|^2 \quad (21)$$

A naive approach to infer this quantity would be simulating the time evolution under the influence of the various $\hat{H}(\vec{x}_i)$ with a classical computer. However, the complexity of performing this simulation is the main reason of studying quantum simulators in the first place, thus the algorithm would become intrinsically inefficient. This basic strategy is called *classic likelihood evaluation* (CLE).

In *quantum likelihood evaluation* (QLE) a reconfigurable, trusted quantum simulator is used to compute the likelihood function: the simulator is simply evolved under the candidate Hamiltonians $\hat{H}(\vec{x}_i)$, and $P(D|\vec{x}_i)$ estimated as the fraction of times D is observed in a sufficiently large set of experimental runs. This estimation by statistical sampling is unfortunately viable only if the likelihood is significant for at least one of the posited models, otherwise the number of simulations needed to provide a good update of the prior distribution would be extremely large.

Actually, the computational issue is solved with a third flavour of Hamiltonian learning, *interactive quantum likelihood evaluation* (IQLE), outlined in the circuit diagram of figure 7.

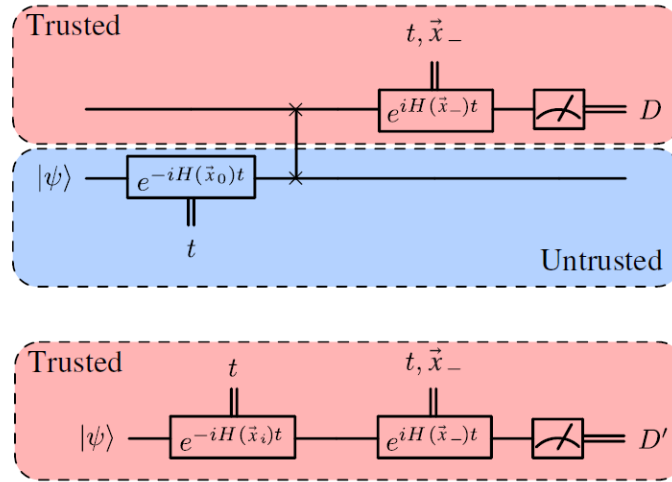


Figure 7: IQLE circuitual scheme. Upper panel: circuit diagram for drawing experimental outcomes. The quantum state evolved in the uncharacterized system is swapped to the trusted simulator to invert the time evolution under the picked $\hat{H}(\vec{x}_-)$. Lower panel: circuit diagram for likelihood evaluation, carried out completely in the quantum simulator. The pink and blue shapes represent the quantum simulator and the quantum object to be certified, respectively. The box depicted as an analog meter represents the measurement stage, which collapses the state into D (D'). Image taken from [35].

This variant employs temporal inversion in order to make $P(D|\vec{x}_i)$ easier to approximate. The quantum system is initially subject to its natural and unknown dynamics, as dictated by $\hat{H}(\vec{x}_0)$; thereafter, the state is transferred at the input of the quantum simulator. A set of parameters \vec{x}_- is extracted from the probability density of \vec{x} and used in the trusted simulator to provide a time-reversed evolution to the system. After this two-step evolution, the system will be described by the following final state:

$$|\psi'\rangle = e^{\frac{it}{\hbar}\hat{H}(\vec{x}_-)} e^{-\frac{it}{\hbar}\hat{H}(\vec{x}_0)} |\psi\rangle \quad (22)$$

The simulator states employed for likelihood estimation will be acted upon by the various candidate Hamiltonian models, then the same backwards evolution will be applied. This manipulation is employed to reduce the output evidence to two outcomes only: the systems can be revealed to be either in the same state as the initially prepared one $|\psi\rangle$ or in a different one. The reversed evolution will provide a sharp distinction between the hypotheses in the prior distribution, as if $|\psi'\rangle$ is measured to be in the initial state, the outcome strongly points to $\hat{H}(\vec{x}_-) \approx \hat{H}(\vec{x}_0)$.

In fact, the theory of quantum chaotic systems [36] assures that, for a complex quantum system, if time evolution is imperfectly reversed with a Hamiltonian operator \hat{H}_b , differing from the forward-evolution Hamiltonian \hat{H}_a by a large amount with respect to the characteristic eigenvalue gap, the overlap with the initial state

$$|\langle\psi| e^{-\frac{it}{\hbar}(\hat{H}_a-\hat{H}_b)} |\psi\rangle|^2 = P(\psi|\hat{H}_a) \quad (23)$$

will become exponentially small after a short timescale, saturating at an asymptotic minimum roughly evaluated as N^{-1} , where N is the dimension of the Hilbert space in which the systems evolve. The left-hand side quantity in equation 23 is called *Loschmidt echo*. In the same equation, the likelihood is deemed conditional only on \hat{H}_a because \hat{H}_b is kept fixed both for the unknown quantum system and for the reversal of all candidate Hamiltonian models.

This sensitivity to small Hamiltonian perturbations is showed in figure 8.

This assures that the worst-fitting models will return a negligible likelihood estimation, while ensuring that the best parameters will return easily-sampled likelihood values of order $O(1)$, allowing the uncertainty in the posterior distribution to shrink exponentially as new outcomes are collected and compared with the simulation. This computational regime requires adaptive adjustment of the measurement time

$$t = \frac{1}{|\vec{x}_1 - \vec{x}_-|}, \quad (24)$$

where \vec{x}_1 is also picked from the prior probability density: as the uncertainty in the estimated parameters shrinks, the sampling procedure will tend to pick longer times to ensure that informative experiments continue to be chosen as certainty about the unknown parameters increases. The Loschmidt echo becomes, in fact, more and more sensitive to small differences in the forward and reverse Hamiltonian as the evolution time increases.

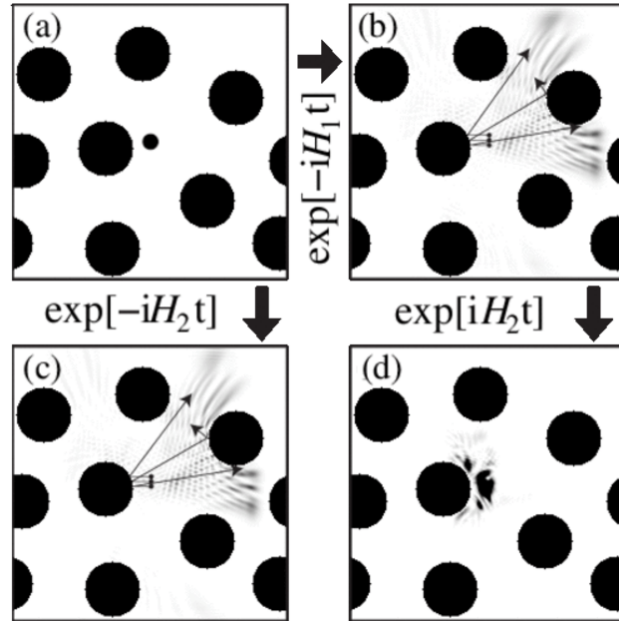


Figure 8: Wave-packet evolution in a Lorentz gas, a dynamical system where the motion is free outside of the black circular regions, where an infinite potential barrier forbids penetration by the wavefunction. **(a)** Initial state at $t = 0$; the momentum is pointing to the left. **(b)** State evolved under the unperturbed Hamiltonian \hat{H}_1 for a time \bar{t} . **(c)** State evolved under a slightly perturbed Hamiltonian \hat{H}_2 for \bar{t} . The perturbation is applied as a distortion to the diagonal components of the mass tensor. **(d)** State evolved backwards in time by $-\hat{H}_2$, starting from **(b)**. The squared overlap (Loschmidt echo) between the states depicted in **(a)** and **(c)** is only 0.09. Image taken from [37].

1.2.3.3 Algorithm performance

Bayesian inference requires experiments to be performed, in principle, for all possible values of the parameters of the Hamiltonian we seek to approximate. Being this a computationally intractable problem, some sampling strategy for the parameters space is needed: a possible solution comes from the *sequential Monte Carlo* method. This technique provides a rule to discretize the probability density function, as learning progresses, and to determine the settings for the quantum simulator experiments.

After each prior probability density update, the weighted number of discrete samples of the parameters space (also called *particles*, $N_{\text{eff}} = \frac{1}{\sum_j w_j^2}$), is compared to a given threshold. If the threshold is not met, new points are added to the discrete collection by randomly extracting particles from the posterior distribution. The prior weight of these new particles is uniformly set and they are considered part of the distribution from the next iteration of the algorithm on. This strategy enforces a motion of the particle density around regions of high probability, in order to sample correctly the experimental probability density.

The complete algorithm with interactive likelihood evaluation is described in panel 1.

The computational cost (in terms of number of runs of the quantum simulator) of the quantum Hamiltonian learning algorithm has also been estimated [35]. It is naturally expressed as the product of two terms:

$$\text{Cost} = N_{\text{exp}}(\delta) \cdot \text{Cost}(\text{update}; \epsilon) \quad (25)$$

Here, $N_{\text{exp}}(\delta)$ is the number of updates required to shrink the parameter uncertainty below δ and $\text{Cost}(\text{update}; \epsilon)$ is the number of runs of the trusted simulator needed to perform a single update; more precisely, the number of runs required to derive the posterior distribution of the weights with an error below ϵ .

$\text{Cost}(\text{update}; \epsilon)$ scales at most as $\frac{M}{\epsilon^2}$, M being the number of particles for the parameter space discretization. The update process will be efficient if the number of picked particles is quite small; additionally, the complexity is lowered if the posterior distribution is sharply peaked.

The bound for the total computational cost is harder to estimate and, once derived, more opaque; nevertheless, for a fixed number of updates, the cost of inference is exponentially lower for interactive quantum likelihood evaluation with respect to simple classical likelihood evaluation.

1.2.3.4 Experimental demonstration

The first experimental implementation of the Hamiltonian learning algorithm that has been described above was reported this year [38].

Algorithm 1 Quantum Hamiltonian learning
 with interactive quantum likelihood evaluation

Require: prior weights w_1, \dots, w_M , particle locations $\vec{x}_1, \dots, \vec{x}_M$, total number of distribution updates N_{exp} , number of samples to estimate the likelihood N_{samp} , state preparation protocol for $|\psi_0\rangle$, resampling SMC algorithm.

```

for  $i = 1 \rightarrow N_{\text{exp}}$  do
  Draw  $\vec{x}_-$  and  $\vec{x}'$  from the  $\vec{x}$  probability density
   $t = \|\mathbf{H}(\vec{x}') - \mathbf{H}(\vec{x}_-)\|^{-1}$   $\triangleright$  Choose  $t$  adaptively
   $D \leftarrow$  measurement of  $e^{\frac{it}{\hbar}\mathbf{H}(\vec{x}_-)} e^{-\frac{it}{\hbar}\mathbf{H}(\vec{x}_0)} |\psi_0\rangle$ 
   $\triangleright$  Perform IQLE experiment on untrusted system
for  $j = 1 \rightarrow M$  do
   $p_j = 0$ 
for  $k = 1 \rightarrow N_{\text{samp}}$  do
   $D' \leftarrow$  measurement of  $e^{\frac{it}{\hbar}\mathbf{H}(\vec{x}_-)} e^{-\frac{it}{\hbar}\mathbf{H}(\vec{x}_j)} |\psi_0\rangle$ 
   $\triangleright$  Perform IQLE experiments with trusted simulator
  if  $D' = D$  then
     $p_j = p_j + 1$   $\triangleright$  Update likelihood
  end if
end for
   $p_j = \frac{p_j}{N_{\text{samp}}}$ 
end for
   $Z = \sum_{m=1}^M w_m p_m$ 
for  $j = 1 \rightarrow M$  do
   $w_j = \frac{w_j p_j}{Z}$   $\triangleright$  Update posterior distribution
end for
if  $\frac{1}{\sum_j w_j^2} < \frac{M}{2}$  then
  resample  $\vec{x}_i, w_i$  with SMC procedure
   $\triangleright$  If number of samples is under threshold, extract new particles
end if
end for
return  $\sum_m w_m \vec{x}_m$   $\triangleright$  Return Bayes estimate of  $\vec{x}_0$ 

```

The work succeeded in validating a single-parameter Hamiltonian describing the electron spin dynamics of a negatively charged nitrogen vacancy (NV^- center) in a diamond sample, interacting with a microwave field. A magnetic field was generated along the axis of the nitrogen vacancy, in order to remove the degeneracy of its $m_s = \pm 1$ spin states. Optical initialization and read-out of the state were performed by laser light focused around the nitrogen vacancy by a confocal microscope setup, while delayed microwave pulses were used to prepare the electronic spin in the initial state of its temporal dynamics and to stop its time evolution.

After being driven out of the stationary state by the microwave pulse, the spin was subject to Rabi oscillations, described by the Jaynes-Cummings Hamiltonian:

$$\hat{H}(f) = \frac{f}{2} \hat{\sigma}_x, \quad (26)$$

where $\hat{\sigma}_x$ denotes the x Pauli matrix. The Rabi frequency f was the learning parameter whose value was to be inferred with the algorithm implementation.

The digital quantum simulator for this experiment was a *silicon photonics* chip, i.e. the waveguides were patterned out of a silicon layer and enclosed in a silicon dioxide cladding. The device layout is reported in figure 9.

The first devices encountered in the chip footprint starting from the left side of figure 9 are spirally-wrapped guides for generation of single photon couples through spontaneous four-wave mixing of the coupled coherent light. The black boxes on top of the segments where guides are brought in proximity represent *multi-mode interferometer* structures acting as balanced beam splitters. The golden strips are titanium thermal phase shifters (and their electrical contacts) for re-configuring actively the phase imbalance along different waveguides and implementing different unitary operators and quantum interference regimes. Two Mach-Zehnder interferometers, \hat{U} and \hat{V} , act as the cornerstone of the simulation: by governing the phase difference, it is possible to realize all the unitary operations determined by the Rabi Hamiltonian $\hat{H}(f)$. The Mach-Zehnder interferometer \hat{M} plays the role of a probabilistic filter, along with a post-selection strategy [39].

The likelihood evaluation was performed with an entanglement-based routine. By post-selecting on the detection of the second photon out of one of the upper waveguides, it possible to consider only entangled states of the form:

$$\frac{1}{\sqrt{2}} (|0_s\rangle \hat{U} |0_i\rangle + |1_s\rangle \hat{V} |0_i\rangle), \quad (27)$$

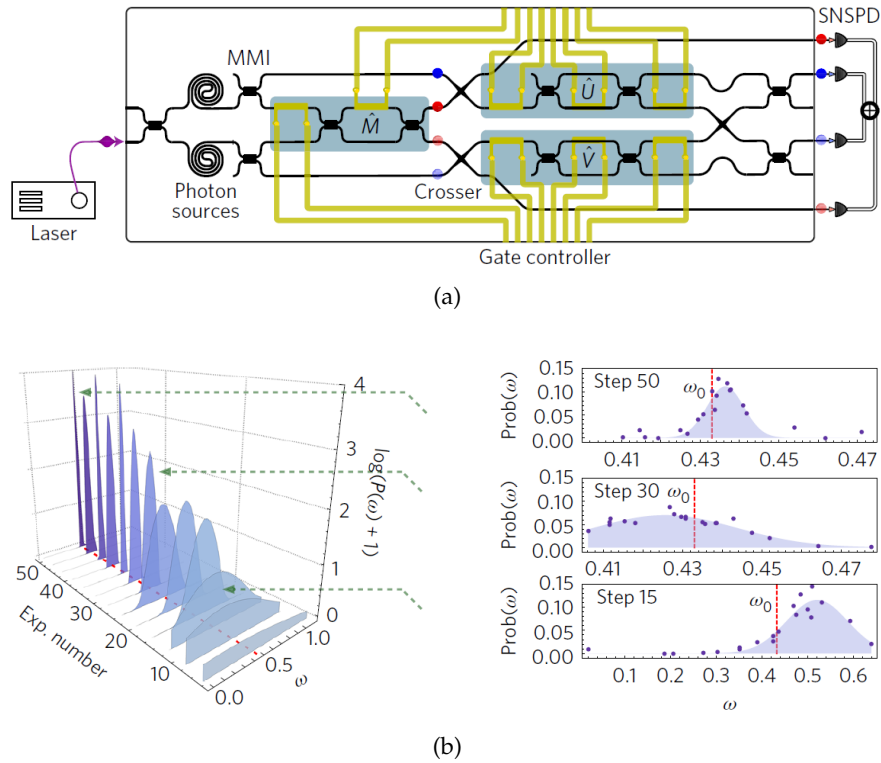


Figure 9: **(a)** Schematics of the silicon photonics quantum simulator. Spontaneous four wave-mixing of the coupled laser light generates a pair of idler (blue) and signal (red) photons at different frequencies. The unitary performed on the idler photon is coherently controlled by the signal qubit, and performing measurements \hat{M} on the signal photon enables likelihood evaluation. Single-photon counting is performed off-chip by superconducting nanowire detectors. **(b)** Posterior distribution of the normalized Rabi frequency along 50 iterations of the Bayesian learning procedure. The standard deviation of the probability density consistently shrinks until saturation sets in, after ~ 25 experiments. The red segmented line corresponds to the Rabi frequency value extracted from a fit of observed Rabi oscillations. Image adapted from [38].

where the s and i subscripts denote the signal and idler qubits. If projective measurements of $\hat{\sigma}_x$ are performed on the signal qubit, the probability p_+ of observing a $+1$ eigenvalue is:

$$p_+ = \frac{1 + \text{Re} \langle 0_i | \hat{U}^\dagger \hat{V} | 0_i \rangle}{2} \quad (28)$$

Conversely, if a $\hat{\sigma}_y$ projective measurement is performed, the probability p_{+i} of observing a $+1$ eigenvalue is:

$$p_{+i} = \frac{1 + \text{Im} \langle 0_i | \hat{U}^\dagger \hat{V} | 0_i \rangle}{2} \quad (29)$$

Thus, by combining these two statistically sampled probabilities, one can easily estimate the Loschmidt echo (see equation 23) as

$$|\langle 0_i | \hat{U}^\dagger \hat{V} | 0_i \rangle|^2 = (2p_+ - 1)^2 + (2p_{+i} - 1)^2, \quad (30)$$

if \hat{V} and \hat{U}^\dagger are specified as forward and backwards time-evolution operators and $|0_i\rangle$ is interpreted as the initial state of the simulation. For QLE, the backwards evolution was suppressed by simply setting $\hat{U} = \mathbb{1}$.

By identifying the Mach-Zehnder interferometers phase imbalance as $\theta = f \cdot t$, one can therefore implement all the simulations required by the Bayesian inference algorithm, with adaptive observation time.

This work reported QLE learning of the diamond nitrogen vacancy Rabi frequency and IQLE learning of an analogous Hamiltonian model implemented on-simulator, employing the silicon-on-insulator chip both as the uncertified quantum system and the trusted simulator. This last experiment suggests a fruitful application of Hamiltonian learning as a means of validating the correct functioning of quantum computing gates.

Both approaches led to a fast convergence of the mean estimated frequency to the implemented one, characterized separately by detecting the NV^- fluorescence signal for various delay times between the microwave pulses. An exponential shrinking of the posterior distribution variance, as learning progressed, was observed (see figure 9b). Qualitative evidence for the robustness of Bayesian inference to noise-affected measurements surfaced from the experimental data.

FEMTOSECOND LASER WAVEGUIDE INSCRIPTION

This chapter will briefly review the physics and the main techniques for the direct inscription of waveguides and photonic structures in transparent media with femtosecond laser pulses.

Section 2.1 will present the main features that set the technique apart from more traditional ones.

Section 2.2 will illustrate the physical phenomena underlying the permanent local refractive index increase, while section 2.3 will briefly list the parameters affecting the intensity profile of the radiation field focused inside the sample and the resulting refractive index modification.

Section 2.4 will provide a non-exhaustive overview of the integrated photonic devices that can be fabricated by direct waveguide inscription, with particular attention to those used during this thesis project.

Finally, in section 2.5 the applications of the technique in quantum optics, quantum information and computing will be shortly reviewed.

2.1 OVERVIEW

Femtosecond Laser Micromachining (FLM) is a fabrication technique exploiting a femtosecond pulsed light beam, generally emitted by a laser operating in mode-locking regime, to process a wide range of different substrates: radically different modifications are available, depending on the particular irradiation conditions.

In the last two decades the possibilities of versatile processing of transparent materials with femtosecond lasers have aroused great interest: in particular, it is possible to drill deep holes with micrometrically controlled dimensions [40] and induce gentle, permanent refractive index modifications in the sample volume [41].

The latter capability, in particular, has been exploited for the direct writing of high quality waveguides, by translating uniformly the sample as the femtosecond beam is brought to focus inside its volume. The refractive index is, in fact, altered in a micrometric region centered around the peak of the irradiation profile. This application was first demonstrated by the seminal contribution of Davis and coworkers [41].

Combined with high-precision motion stages, this process allows to fabricate a plethora of photonic devices, in passive and active substrates, with some important distinguishing features and advantages with respect to the lithographic techniques customarily adopted in the telecommunication and electronics industries:

- *Rapidity and cost-effectiveness.* FLM is a mask-less and single-step technique. The circuit design can be modified by just setting a new laser irradiation path, without the costs of producing new photomasks. In addition, it does not require a strict environmental control and auxiliary facilities like a cleanroom, and the fabrication setup is relatively simple. All these features contribute in making FLM a rapid and cost-effective technique for fabricating prototype devices and testing different designs, although it is not as suited as lithographic processes to large-scale production.
- *Flexibility.* Many different materials can be processed by femtosecond radiation exposure, from glasses to polymers and crystals [42], by simply tailoring the irradiation conditions without significant changes in the fabrication setup. Additionally, several different physical phenomena can be excited by femtosecond laser pulses in order to induce local and controlled modifications in an even broader class of materials, e.g. two-photon polymerization and bonding of different transparent substrates [42].
- *Unique 3D capabilities.* Due to the non-linearity of the processes involved in the localized radiation absorption, the substrate

modification is confined to a small volume around the radiation focus. Therefore, by simple translation of the beam along the depth of the sample, it is possible to write truly three-dimensional structures, according to geometries that would not be available to the fundamentally planar lithographic techniques. This additional degree of freedom enables the design of new devices and configurations, e. g. for the manipulation of light polarization.

The main disadvantages of femtosecond laser-inscribed photonic components compared to standard planar lightwave circuits are:

- Lower achievable index contrast between core and cladding (typical values of $\Delta n \sim 0.001 \div 0.01$, to be compared to $\Delta n = 0.025$ in planar lightwave circuits), leading to the necessity of very mild, longer bending sections which increase the device footprint for a given photonic structure.
- Significantly higher propagation losses than the typical figure of ~ 0.01 dB/cm of industry standardized photonic circuits.

However, we should note that this increased performance of lightwave circuits is limited to the fabrication of waveguides in standard substrates, with optimized technological processes. For less conventional materials or applications, lithographic techniques cannot provide satisfying light confinement and FLM can demonstrate a higher efficiency.

2.2 FEMTOSECOND PULSE INTERACTION WITH DIELECTRICS

To perform micromachining of transparent materials, an ultrashort laser pulse train is focused deep inside the volume of the substrate to process. Since linear absorption is undesired for FLM, the condition $E_g > h\nu$ always holds, E_g being the energy gap between the valence and conduction band in the electronic structure of the material, and ν the electromagnetic carrier frequency of the pulsed radiation. If the peak intensity of the pulse exceeds a few TW/cm^2 the promotion of electrons to the conduction band will be driven mainly by nonlinear effects and the physical and chemical processes leading to the permanent refractive index modification will be excited. In detail, the process can be divided in three steps: generation of a localized free electron plasma, energy relaxation and material modification.

The plasma formation is initiated by the interplay of two mechanisms: *multiphoton absorption* and *tunneling ionization*, illustrated in panels **a.** and **b.** of figure 10. We remark that these two mechanisms are not mutually exclusive but they can concur together to electron promotion to the conduction band. In the former case, dominant at

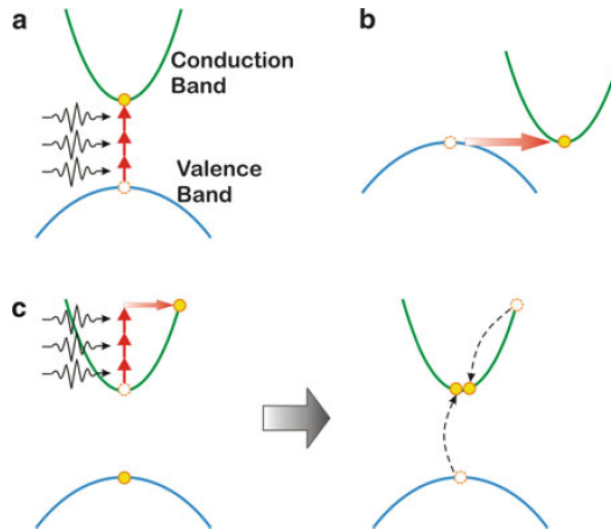


Figure 10: Main processes in the sequence leading to the creation of a free electron plasma by interaction with femtosecond radiation. **a.** Multiphoton absorption **b.** Tunneling ionization **c.** Inverse Bremsstrahlung and avalanche ionization. Image taken from [43].

high photon energy and low irradiance (longer laser pulses), an electron near the top of the valence band absorbs simultaneously m photons, satisfying the condition $m\hbar\nu \geq E_g$, allowing it to bridge the band gap and be excited to the conduction band. At higher peak irradiances (shorter laser pulses), the strong time-varying electric field distorts the band structure, enabling interband transitions by quantum tunneling of the electron from the valence to the conduction band. Evaluating the Keldysh parameter [44] for typical waveguide writing conditions, we derive $\gamma \sim 1$, indicating a combination of both processes for nonlinear ionization.

Once a seed of quasi-free electrons has been excited to the conduction band during the leading edge of the ultrashort laser pulse, they can freely absorb photons through linear processes and inverse Bremsstrahlung. When the electronic kinetic energy surpasses E_g , it can ionize new electrons in valence band states by direct collision, favouring the promotion of new electrons in the conduction band. This process gives rise to an avalanche electron excitation (panel **c.** of figure 10). The dominant role of this phenomenon explains the mild dependence of the optical breakdown threshold irradiance on the energy gap, allowing FLM to be useful on a wide range of different materials. In fact, nonlinear effects in this picture are needed only to generate an initial seed of quasi-free electrons.

Avalanche ionization causes a rapid growth of the free carrier density in the focal region, leading to an increase of the *plasma frequency*. Once this quantity approaches the laser frequency, linear absorption

of radiation by the electronic plasma becomes very efficient and the remaining pulse energy is mostly transferred to the electronic degrees of freedom. The subsequent plasma relaxation, in which its energy is ceded to the atomic lattice, on timescales longer (10^{-11} s) than the typical ultrashort pulse duration, is responsible for the observed material modifications, happening between 10^{-9} and 10^{-6} s from the pulse onset.

Different physical mechanisms may concur to the modification of the optical properties of the substrate. A number of studies performed in silica glasses [45][46] have found the dominant process to be the rapid temperature quench, after the trailing edge of the pulse, of the material lying in the focal region. The following *densification* is connected to a local refractive index increase. Other contributions have been recognized, e.g. colour center formation [47], ion exchange/migration effects [48], stress-induced changes and thermal accumulation phenomena, but the role of any of them depends strongly on the exposure conditions and material properties.

In general, three different regimes of morphological changes have been identified. Impinging with low-energy pulses results in a smooth and isotropic refractive index change in the focal region, suitable for waveguide fabrication [45]. Increasing the optical power, interference effects between the radiation and the generated electron plasma lead to birefringent periodic modulation [49], observed mostly in fused silica micromachining. At even higher pulse energies, micro-explosions and shockwaves ensue after the quasi-free electrons transfer their energy to the lattice, leaving behind a less dense or hollow core, surrounded by a region of increased refractive index [50]. For most photonic applications, the fabrication irradiance is kept close to the nonlinear ionization threshold, in order not to stray in the latter modification regimes and to keep further nonlinear effects, such as self-focusing, negligible [42].

A final remark about why sub-picosecond pulses are essential for waveguide inscription is needed. For longer pulses, the pulse energy required to reach the threshold irradiance for nonlinear photoionization would be exceedingly high: plasma formation by avalanche ionization would still occur, but from a randomly-distributed seed of free carriers excited thermally or confined around defects or impurities in the substrate. Nonlinear ionization provides instead a seed of quasi-free electrons very well-localized around the focus of the femtosecond beam, resulting in a deterministic and uniform energy absorption.

Furthermore, since plasma relaxation happens after a couple tens of picoseconds, ultrashort pulses deliver energy to the plasma on a completely different timescale. The temporal decoupling of absorption and relaxation results in a more sensitive and precise micromachining.

2.3 FABRICATION PARAMETERS

Besides pulse energy and duration, whose effects have already been mentioned, a number of other factors and inscription conditions influence the morphology of the induced material modification and the quality of the fabricated waveguides. The largest influence is acted by the pulse repetition rate, the focusing depth and numerical aperture (NA), the writing configuration chosen and the sample translation speed.

2.3.1 Focusing conditions

FLM requires focusing the incident ultrashort pulses inside the sample by means of some focusing optics, in order to achieve a small focal spot and the threshold irradiance for nonlinear effects. Generally, microscope objectives are preferred to simple lenses, as they compensate chromatic and spherical aberrations and induce less distortion of the beam in the proximity of the focus.

Neglecting nonlinear effects and spherical aberration, the spatial intensity profile of the beam emitted by a femtosecond laser can be approximated in a *Gaussian optics* model. The diffraction-limited minimum waist radius for a collimated Gaussian beam focused in a dielectric is given by:

$$w_0 = \frac{M^2 \lambda}{\pi \text{NA}}, \quad (31)$$

where M^2 is the Gaussian beam propagation factor and λ the laser free-space wavelength. This expression shows that a high numerical aperture objective allows to obtain a tighter focal spot.

The refractive index mismatch occurring when light enters the dielectric sample introduces additional spherical aberration, unless specific compensation optics or techniques are used. This results in a pronounced depth-dependence for femtosecond laser-written buried structures [51], especially for high NA focusing. This beam distortion can be mitigated by using an immersion objective, where an oil layer with a refractive index close to that of the glass substrate is inserted between the top surface and the microscope objective. However, these objectives have a limited working distance and available inscription depth range.

Another factor that influences the beam profile as it converges to focus is the nonlinear coefficient n_2 , relating a linear variation (generally of positive sign) of the refractive index to the intensity of the electromagnetic wave. The propagation of a tightly focused and intense laser beam inside a markedly nonlinear material, such as chalcogenide glasses, silicon crystals or metal oxides, can cause phenomena

like self-focusing and filamentation, resulting in axially elongated refractive index alterations that are not desirable as waveguide cross-sections.

2.3.2 Writing configuration

Two standard configurations for femtosecond laser writing of waveguides can be identified. These are schematically illustrated in figure 11.

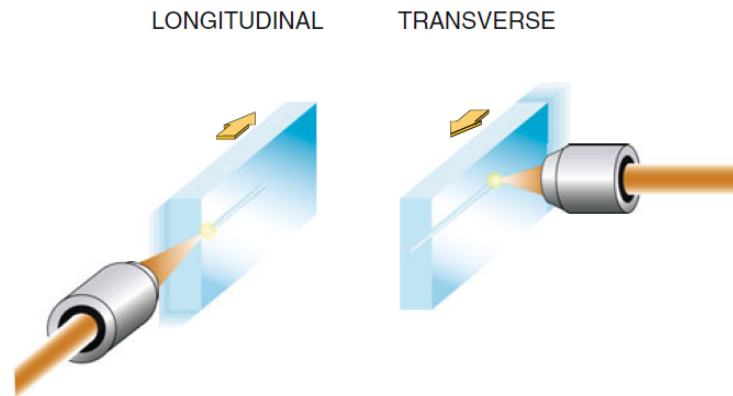


Figure 11: Longitudinal and transverse writing geometries. In the longitudinal (transverse) writing configuration the light impinges in a direction parallel (perpendicular) to the waveguide axis. Image taken from [43].

- *Longitudinal incidence.* In the longitudinal configuration, the sample lies in a plane parallel to the laser beam, as it is translated. The resulting waveguide structures are characterized by a cylindrical symmetry, owing to the rotationally-invariant transverse profile of zero-order Gaussian modes.

The main disadvantage is the low focusing range inside the sample, limited by the working distance of the microscope objective, which can hardly exceed a few millimeters.

- *Transverse incidence.* In the transverse writing scheme, the sample is translated in a plane orthogonal to the incident beam. The waveguide length is no longer limited by the working distance of the objective (but rather by the translation stages dynamic range), and the depth range provides usually sufficient flexibility in order to write three-dimensional optical circuits for most applications.

However, the waveguide cross-section will be asymmetric and elliptical, influenced strongly by the focal spot shape¹. Wave-

guides fabricated in the transverse configuration will therefore support elliptical electromagnetic modes, coupling less efficiently with standard optical fibers, and will introduce a further birefringence term.

In order to reduce these effects, beam shaping techniques have been introduced to fine-tune the focal spot geometry [52] [53]. Alternatively, multi-scan writing of waveguides permits to control with improved precision the cross-sectional shape [54].

2.3.3 Repetition rate

The repetition rate of the femtosecond pulse train is a crucial parameter, determining different fabrication regimes with distinct morphological features of the resulting waveguides.

In the low repetition rate regime ($1 \div 250$ kHz), typical of Ti:Sapphire regeneratively amplified lasers, the heat is released from the focal spot to the surrounding material by conduction before the arrival of the next pulse and the local temperature is quenched to the equilibrium value. Thus, the substrate modification is mainly determined by the energy deposited by single pulses, separately. The waveguide cross-section will be determined by the focusing conditions, as discussed in section 2.3.2, and, in the transverse writing configuration, beam shaping or multi-scan techniques will be required to induce a circular refractive index modification. In many cases, the processing speed has to be kept under some tens of $\mu\text{m/s}$ in order to transfer a sufficient amount of energy per unit volume to the sample.

If the repetition rate is increased to several MHz, such that the time between consecutive pulses is much shorter than the substrate thermal relaxation time, strong cumulative thermal effects may take place [55] [56]. These repetition rate values are typical of mode-locked lasers without an amplification stage: the ensuing low-energy pulses require a high NA, oil-immersion objective in order to exceed the irradiance threshold for nonlinear photoionization in the sample. The tight focusing conditions would suggest a tiny altered volume. Actually, a much larger isotropically modified region is observed, produced by thermal accumulation of multiple pulses: waveguides with a circular cross-section are thus inscribed without resorting to beam shaping.

¹ The focal region shape is described primarily by the ratio z_R/w_0 between Rayleigh length and beam waist radius. The Rayleigh length is defined as the distance from the beam waist at which the cross-sectional area of the Gaussian beam has doubled: the two quantities appearing in the ratio represent the two characteristic dimensions of the maximum laser intensity region in the sample volume. One can prove that $z_R/w_0 = n/\text{NA}$, n being the substrate refractive index: for typical conditions the ratio will be significantly greater than 1.

The intermediate regime (hundreds of kHz to few MHz) is very useful for material processing as well. Ytterbium-based laser systems deliver femtosecond pulses with energies up some tens of μJ s, so focusing with conventional dry objectives is sufficient to inscribe high-quality waveguides. The interplay between energetic pulses and thermal accumulation effects results in more uniform and circular waveguides with respect to those fabricated by low-repetition rate sources, with quite high processing speeds. This regime has been found to be particularly convenient for fabrication of photonic circuits in boron- and aluminosilicate glasses.

2.3.4 Other parameters

In the previous discussion, we have not included many factors that should be considered for the optimal micromachining of a substrate:

- The *translation velocity* of the sample through the laser beam determines the amount of energy deposited per unit volume, proportional to $\frac{f_R}{v}$ (v being the translation speed and f_R the repetition rate); therefore it concurs in determining the regime of material modification or damage and the refractive index alteration that is produced.
- The *laser wavelength* determines the particular nonlinear dynamics providing the electron seed for plasma generation.
- The *light polarization* may exert an influence in the structural morphology as well, especially in a modification regime which exploits birefringent modulation.

2.4 PHOTONIC BUILDING BLOCKS

Since the first demonstration [41] of waveguide writing, all kinds of active and passive photonic devices have been successfully demonstrated on a vast range of substrates, from fiber Bragg gratings [57] to waveguide amplifiers and lasers [58]. Due to the huge diversity of such functional devices, that played the role of a benchmark for the versatility of FLM and the creativity of its user community, we will focus here on the most relevant ones, employed also in the integrated circuits developed in this thesis.

2.4.1 Directional couplers

Directional couplers are widely employed to transfer optical power between two waveguides: these are brought in close proximity, such that the evanescent field extending in the cladding can excite the polarizability of the neighbour and establish optical coupling. The de-

tailed functioning of the device, in the weak perturbation approximation, is described in the framework of *coupled mode theory* [59] and briefly summarized in section B.2.

Directional couplers are, in general, preferred to Y-junctions for power splitting purposes, because they avoid the extra losses induced by the path split, although their performance is very polarization and wavelength-sensitive, so that additional engineering effort for the geometry and fabrication parameters must be spent.

The first demonstration of a directional coupler fabricated by FLM was due to Streltsov and Borrelli in 2001, involving an asymmetric design capable of a 1.9 dB splitting ratio for a wavelength of 633 nm.

Devices operating in the telecommunication wavelength range were reported later, in a series of works due to the group of Peter Herman. These couplers were inscribed at high scan speed in borosilicate glass samples, with repetition rates characteristic of the inception of thermal accumulation effects (1 MHz). Low insertion losses (~ 2 dB) were measured, and the size of the single supported mode was engineered to provide an efficient coupling with standard telecommunication optical fibers [60]. These results were extended by subsequent demonstrations of wavelength demultiplexers [61] and broadband directional couplers [62], obtained from the basic coupler design by careful tuning of the *coupling coefficient* κ , through the influence of inscription conditions and geometrical parameters.

The three-dimensional fabrication capabilities of femtosecond laser inscription were explored with non-conventional coupler designs, e.g. X-couplers, in which the waveguides are brought in close proximity at a single point but do not intersect, by virtue of being written at different depths [63], or structures in which more than two waveguides approach in the coupling region, sharing the propagating optical power [64].

Additionally, the polarization behaviour of the directional couplers can be carefully engineered by forcing the waveguides to interact out-of-plane, at a precise angle. In fact, the two linearly-polarized (horizontal and vertical) eigenmodes supported by a single-mode waveguide are not degenerate due to the waveguide birefringence, and come with small differences in the mode profiles and propagation constants. Since the coupling coefficient is proportional to the overlap integral between the electromagnetic modes centered on their carrier waveguide

$$\kappa \propto \iint \vec{E}_a^* \vec{E}_b \Delta n^2 \, dx \, dy, \quad (32)$$

the difference between the horizontal and vertical-polarized splitting ratios can be tuned by varying the coupling angle θ (portrayed in panel c. of figure 12), in order to fabricate directional couplers with

balanced splitting ratio for both polarizations [65], or polarizing beam splitters [9].

This exquisite polarization control is particularly relevant for the field of quantum photonics: in fact, the polarization of photons is an ideal degree of freedom for qubit encoding.

2.4.2 *Mach-Zehnder interferometers*

Mach-Zehnder interferometers employ directional couplers, Y-junctions [66] or multimode interference couplers [38], as their fundamental constituents. The input electromagnetic wave is divided at a first splitter along two branches, that travel in parallel and recombine on a second splitter or coupler. The output power depends on the phase difference established between the two beams as they were following different routes: constructive or destructive interference can happen via geometric imbalance of the optical paths or modulation of the refractive index by one of many physical phenomena. According to the specific application, Mach-Zehnder interferometers can be used to route the optical power in a reconfigurable manner between two ports or to accurately and unobtrusively sense temporal changes in a physical quantity of the environment through the displacement of interference fringes, employing the high sensitivity of the electromagnetic phase to external conditions.

The first demonstration of a Mach-Zehnder device fabricated with FLM was reported in 2002 [67] (see panel **a.** of figure 13). The simple layout saw two waveguides intersecting in two X-coupler sections at an angle of 2° , with a geometrical path difference of $10\ \mu\text{m}$ in the intermediate section. Such difference corresponds to that inferred from the interference fringes in the transmission spectrum measured at the output port when broadband light, emitted from a Ti:Sapphire laser, was introduced in the device. The functioning of the interferometer as a spectral filter was thus validated.

A combination of FLM and thermal poling of a fused silica substrate allowed to construct a Mach-Zehnder interferometer working as an electro-optical modulator [68]. The sample was subject to thermal poling in order to induce a second-order nonlinear susceptibility in the surface layers, and the Mach-Zehnder interferometric branches were brought in the nonlinear layer, at a depth of $11\ \mu\text{m}$ from the upper air interface, by exploiting the intrinsic three-dimensional capabilities of FLM. The remaining sections of the interferometer were in fact machined deeper in the substrate volume, at $48\ \mu\text{m}$, in order to minimize the effect of surface and edge defects, as depicted in panel **b.** of figure 13. Gold electrodes were patterned on top of the sample surface, aligned with the interferometer arm, by sputter coating followed by lift-off. By driving the electrodes with voltages of magnitude $\sim 100\ \text{V}$, the effective refractive index experienced by the elec-

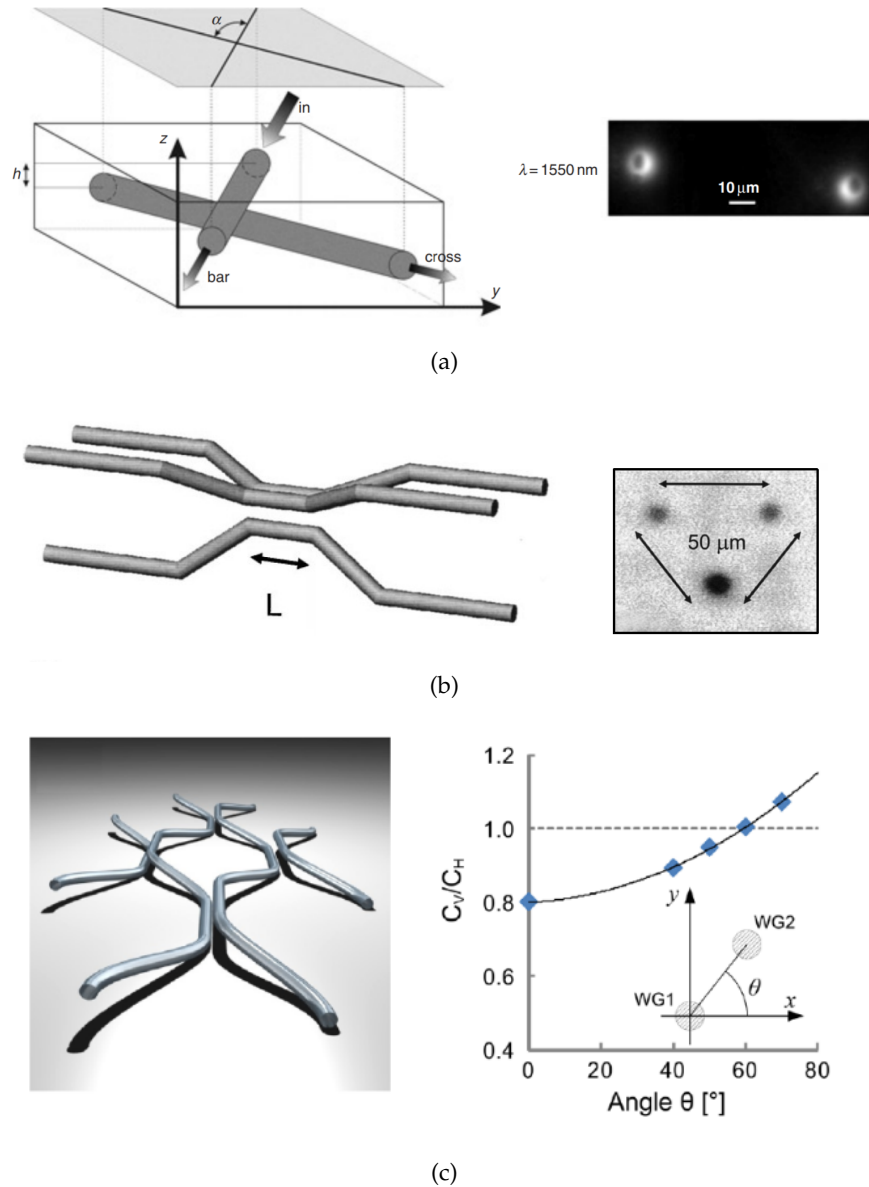


Figure 12: **(a)** Layout of an X-coupler with waveguides lying in different planes and near field imaged at the output facet, showing balanced splitting. Image taken from [63]. **(b)** Schematics of a 3x3 symmetric, three-dimensional directional coupler. The inset shows the balanced power splitting observed from a near-field image at the output facet. Image taken from [64]. **(c)** 3D rendering of an array of out-of-plane directional couplers. The right-side graph shows experimental data on the ratios of the coupling coefficients extracted for the horizontal and vertical polarization states, crossing the $\kappa_V = \kappa_H$ line for $\theta = 62^\circ$. The inset clarifies the definition of θ by showing the cross section of the waveguides in the transverse plane of the coupling region. Image taken from [65].

tromagnetic field in the interferometric arm could be modulated; the effect being readily measurable from small shifts in the transmission spectrum.

A further step towards practically-reconfigurable Mach-Zehnder devices was made in 2015, with the extension of *thermal phase shifters* to femtosecond laser waveguide inscription [11]. After the fabrication of a Mach-Zehnder interferometer in an alumino-borosilicate glass sample, a 50 nm-thick gold layer was sputtered on the upper surface and etched with the same femtosecond laser, in order to pattern thin resistors aligned with the interferometric arms. This fabrication process is illustrated in panel c. of figure 13.

When an electric current was forced in these resistive sections, electrical power was dissipated in the form of heat, by Joule effect. Being the thermal conductivity of glass much higher than that of air at standard conditions, most of the heat was dissipated in the sample volume, creating a temperature gradient decreasing radially from the axis of the heater. The refractive index of the glass is linearly dependent on temperature variations (at least in a limited dynamic range), therefore, power dissipation represented an efficient mechanism for modulating the phase imbalance in the interferometric ring. A measurement of interferometric fringes allowed to retrieve high-visibility oscillations in the output intensity, and to validate a linear modulation of the phase with the dissipated power. A proportionality factor of $\alpha = 13.43 \text{ rad/W}$ was extracted from a sinusoidal fit.

The thermo-optical technology discussed in this last paragraph was also employed in the present thesis work, in order to achieve reconfigurable multiport arrays.

2.5 INTEGRATED QUANTUM PHOTONICS

A seminal paper due to Knill, Laflamme and Milburn [69] proved the feasibility of universal quantum computation with only linear optics elements: single-photon sources, beam splitters, phase shifters and photodetectors. Optical nonlinearities, requiring selected materials and high excitation intensity, were believed to be necessary to build two-qubit gates; this new approach substituted them with an effective nonlinearity provided by post-selection on multi-photon coincidence events.

A surge of interest and experimental effort in adopting guided-wave optics for quantum information and communication originated after the first demonstrations of on-chip Hong-Ou-Mandel interference and integrated quantum gates in 2008 [70]. The perks of on-chip, integrated structures compared to bulk optical setups are in fact remarkable, from the enhanced phase stability to the natural insulation from environmental disturbances and improved electromagnetic mode overlap and selection.

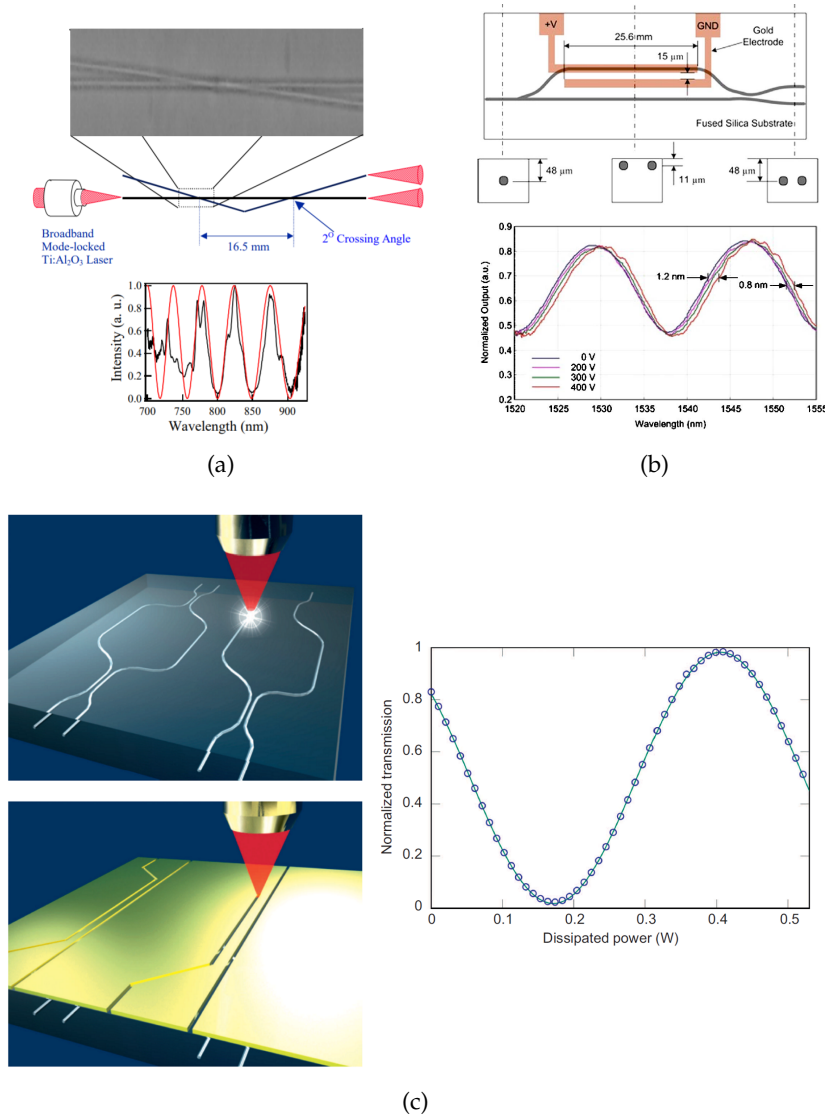


Figure 13: **(a)** Schematics of an interferometer composed of two X-couplers. The blow-up shows a phase-contrast micrograph of the coupling region. The lower graph illustrates the interference fringes measured in the transmission spectrum (black), compared with the theoretical expectations (red). Image taken from [67]. **(b)** Mach-Zehnder interferometer written in thermally-poled fused silica. Gold electrodes are aligned with the structure in order to drive the electro-optical effect. Cross sections of the device at different longitudinal coordinates are included, showing the three-dimensional layout of the device, allowing to enhance electro-optical modulation. The lower graph shows the spectral response of the device and the fringes shift for different driving voltages. Images taken from [68]. **(c)** Left: computer rendering of FLM patterning of thin gold thermal shifters, aligned with the arms of the Mach-Zehnder interferometers underneath. Right: Interference fringes of coherent light with $\lambda = 1550$ nm as electrical power was dissipated inside the shifter. Images taken from [11].

Femtosecond laser micromachining has been playing a prominent role as a platform for quantum photonics due to its versatility and the possibility of immediate translation from blackboard concept to fabrication process. Therefore, this technique proved to be very useful in producing diverse devices for such pioneering research applications, in a relatively short time span.

The first experiment suggesting the suitability of laser-written photonic devices for demonstrating quantum optics effects dates back to 2009 [71]. A single directional coupler (here adopted for its analogy with a beam splitter) was employed for a proof of two-photon interference, reproducing the classical Hong-Ou-Mandel experiment: if two identical and indistinguishable photons impinge at the two input ports of a balanced beam splitter, cancellation of quantum mechanical amplitudes forbids to measure them at the two distinct output modes; indeed, they will form an entangled two-photon Fock state. Pairs of photons were generated at 804 nm by a standard spontaneous parametric down-conversion source, coupled inside the femtosecond laser-written device, and the output branches of the directional coupler were connected through optical fibers to a couple of avalanche photodiode detectors. The delay between the photon wavepackets was scanned via an actuator (external to the integrated device), and a dip in the rate of coincidences of the two single-photon detectors was observed for the optimum temporal indistinguishability case: identical arrival time at the input ports of the beam splitter. The visibility of the dip in coincidence rates was greater than 95%.

Hong-Ou-Mandel interference was later experimentally demonstrated also with polarization-entangled photon couples [72]. The birefringence of femtosecond laser-written waveguides was specifically minimized by employing high pulse repetition rates in the fabrication process, leading to strong thermal accumulation effects and circular guiding cross-sections, resulting in a value about an order of magnitude lower than in lithographically-fabricated circuits ($B = 7 \cdot 10^{-5}$ in that particular work). This points out the superior faculties of FLM as a technological platform for faithfully preserving and encoding polarization. Related experimental data are reported in figure 14.

Advanced polarization control was also instrumental for the demonstration of an integrated CNOT polarization-qubit gate in a linear optical design [73]: the circuit layout contained in fact three partially polarizing directional couplers (i.e. couplers whose splitting ratio depends on the state of polarization of the photons there impinging). The importance of this experiment is remarked by the fact that the CNOT quantum gate, together with arbitrary single-qubit rotations, is sufficient for performing any conceivable quantum algorithm (see section A.2 for reference).

Single-qubit rotations are trivial to implement in bulk optics with birefringent waveplates, but more challenging to perform in guided-wave optics. Hence the importance of a recent demonstration of fixed but arbitrarily-tilted waveplates directly supported by FLM-inscribed waveguides [74]. The developed fabrication technique consists in underfilling a high NA focusing objective and displacing the femtosecond laser beam with respect to the optical axis: the objective will focus the light approximately in the same point, but with a certain tilt, that results in waveguides with an elliptical and rotated cross-section. Since the birefringence in the waveguide is subjected to a contribution from the asymmetrical core shape, the ordinary and extraordinary axes will be aligned with the inscription laser beam. The idea is summarized by the illustration of the fabrication process in figure 14. Another technique to fabricate integrated arbitrary waveplates was demonstrated almost simultaneously by the group of Alexander Szameit [75]. In that case, a reorientation of the principal axes of birefringence was obtained by inducing a mechanical stress field along the waveguide by inscription of a defect line nearby.

Complex interferometric arrays can also be realized with femtosecond laser micromachining, and provide a versatile physical platform for studying the properties of quantum objects, e. g., performing random walks, as already mentioned in section 1.1.3. Continuous [76] and discrete-time [65] quantum walks have been probed with distinguishable and indistinguishable photons, along with an example of correlated photons performing a quantum walk on a two-dimensional network of waveguides [77].

Examples of the level of maturity and flexibility reached by FLM for quantum photonics can be provided by the works of Crespi et al. [9] and Tillmann et al. [78], involving *boson sampling* experiments. Boson sampling is a quantum process reputed intricate for classical computers to simulate, due to the complexity of calculating matrix *permanents* [79]. In particular, in [9] boson sampling was performed at the output of a multiport interferometer designed to implement a unitary transformation extracted at random. The translation from complex unitary matrices to linear optical elements is unambiguous and complete when employing an algorithm like the one described in [8] (as will be clarified in the following chapters), requiring the use of beam splitters and phase shifters of arbitrary reflectivity and delay. In [9], the desired reflectivity could be reached by an out-of-plane rotation of one of the two guides in a directional coupler, thus modulating the coupling coefficient, and the phase shift was controlled by an appropriate geometrical distortion of the curved joining tracts between adjoining beam splitters. (See figure 14)

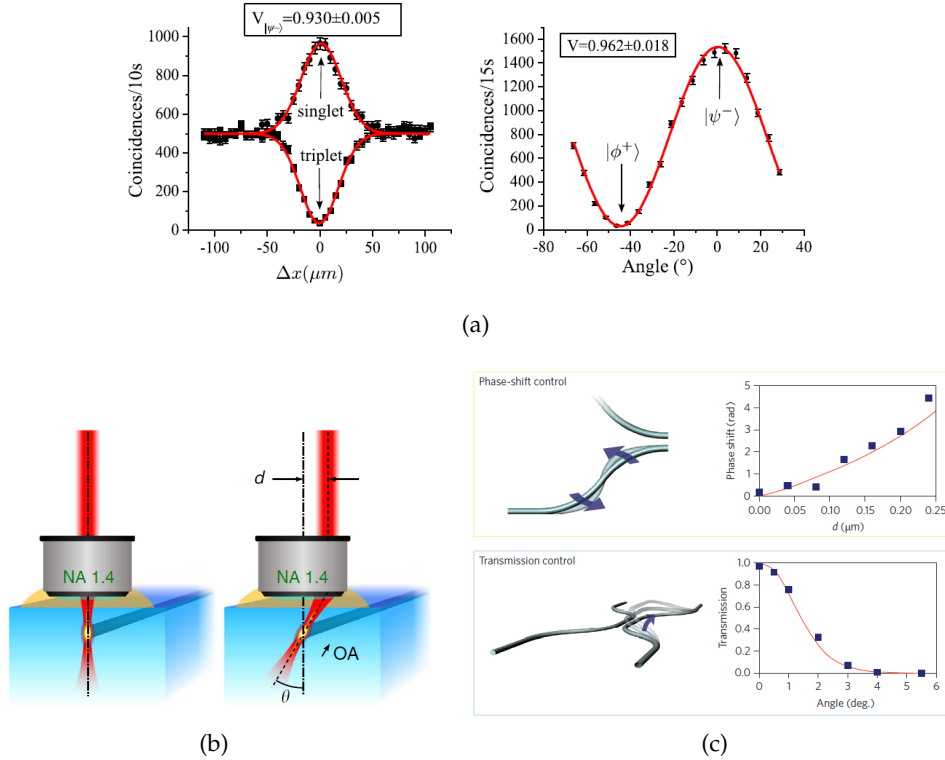


Figure 14: **(a)** Coincidence rates for polarization-basis Bell states interfering at the output ports of a directional coupler. Left: coincidence peak (dip) for antisymmetric (symmetric) input states. Right: sinusoidal modulation of the observed coincidence rate as a discrete waveplate inserted along one of the input modes was rotated. The control of the quantum phase allows to express, among others, the Bell states $|\phi^+\rangle$ and $|\psi^-\rangle$, entailing the minimum and maximum observed coincidences. Image taken from [72]. **(b)** Fabrication scheme for polarization-rotating waveguides. A laser beam entering the objective with an offset d with respect to the optical axis results in a waveguide cross-section tilted of an angle θ , with rotated anisotropy. Image taken from [74]. **(c)** Scheme for controlling transmissions and phase shifts for performing an arbitrary unitary transformation. Upper panel: phase shift control through waveguide deformation. Lower panel: transmission control through directional coupler deformation and κ modulation. Image taken from [9].

MATERIALS AND METHODS

This chapter will present the standard experimental techniques adopted in this work. Section 3.1 will describe the instrumentation and the laboratory setup for the inscription of photonic chips with an ultrashort pulsed laser. Section 3.2 will explain the additional processes performed on the photonic chips after waveguide inscription, including an explanation of the method for patterning thermo-optical phase shifters. Finally, section 3.3 will focus on the established procedures to characterize with coherent light the performance of the fabricated devices.

3.1 WAVEGUIDE INSCRIPTION SETUP

3.1.1 General scheme

The setup for femtosecond laser micromachining in dielectric materials is schematically depicted in figure 15. The output of a mode-locked Yb laser source (described in more detail in the following section), emitting pulses centered at the infrared wavelength $\lambda = 1030$ nm, is variably attenuated by passing through a turnable birefringent $\lambda/2$ waveplate and a polarizing beam splitter. Since the laser source is linearly-polarized, transmission can be very broadly modulated, according to the Malus law.

The beam is then carried, by a series of reflections on several dielectric mirrors, to the input aperture of a microscope objective, mounted above a three-dimensional, numerically-controlled, linear motion system where the sample to be processed is glued.

The microscope objective, which serves the purpose of focusing the femtosecond beam at the surface or inside the sample, can be substituted and chosen between multiple dry and oil immersion variants; for all the fabrications performed during this thesis a 50x, 0.6 NA dry objective with a working distance of 7.6 mm was selected.

The mirrors and a gimbal adjuster (Thorlabs GM100) provide enough degrees of freedom to precisely align the laser beam with re-

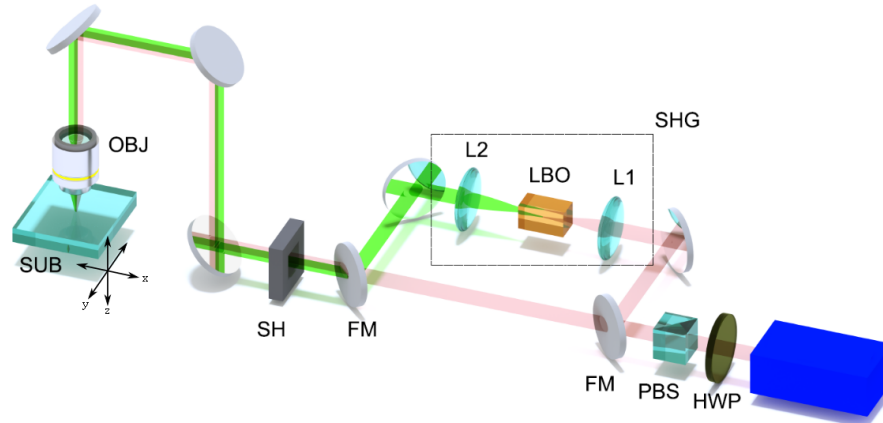


Figure 15: Scheme of the fabrication setup. The $\lambda/2$ waveplate (HWP) and the polarizer cube (PBS) allow to regulate the energy per pulse. The beam is brought to a microscope objective (OBJ) that produces a focus inside the sample (SUB), attached to the motion stages. Two flip mirrors (FM) optionally deviate the infrared beam to a second-harmonic-generation setup (SHG). There, the beam is focused inside a nonlinear crystal (LBO) by a 15 cm focal length lens (L1) and recollimated at the output by a 30 cm focal length lens (L2). The motion of the stages is synchronized with a mechanical shutter (SH). Image taken from [80].

spect to the sample, in the transverse writing configuration (which was adopted for all the waveguides mentioned in the remainder of this thesis). The planarity of the upper surface of the sample is monitored through the observation of the surface back reflection, recollimated by a second passage through the microscope objective, with a CCD camera collecting the small fraction of the back-reflected beam that is transmitted through a dielectric mirror. This alignment operation is carried out at the beginning of each writing session, to define the frame of reference of the sample and to correctly set the vertical offset of the motional stages with respect to the focus.

The motion stages are synchronized with a mechanical shutter (Thorlabs SH05, opening and closing time ~ 10 ms), to stop the inscription while the sample is repositioned, or to prevent the exposure of a given region.

The setup provides additionally the possibility of micromachining with the second harmonic of the ultrashort pulses ($\lambda = 515$ nm). By the rotation of two flip mirrors the beam can be brought to focus inside a lithium triborate (LBO) crystal, whose temperature is controlled with a crystal oven in order to establish noncritical phase-matching for the second-harmonic generation process. The beam width is regulated by means of a telescope system formed by two confocal lenses.

3.1.2 *Laser source*

The femtosecond laser source is a cavity-dumped, mode-locked oscillator [81] developed in a collaboration with the Heidelberg Max Planck Institut (Germany) and High Q Laser GmbH (Austria). The active medium, a $KY(WO_4)_2$ crystal doped at 5% concentration with Ytterbium, emits at a wavelength of $\lambda = 1030$ nm and is pumped by a multiemitter InGaAs laser diode bar with a 980 nm wavelength and a typical optical pump power of 15 W.

The cavity is folded by employing several mirrors, exhibiting a total optical length of 8.9 m compressed in a compact on-table footprint. A SESAM (SEmiconductor Saturable Absorber Mirror) is used as the terminal mirror of the cavity, driving the longitudinal modes in the passive mode-locking regime. The pulse train inside the cavity yields a repetition rate of about 17 MHz.

Mode-locking is combined with cavity-dumping of the pulses outside of the cavity, by the operation of a Pockels cell combined with a thin-film polarizer. An electronic driver, synchronized with the intracavity pulse train, controls the voltage applied to the Pockels cell with an adjustable magnitude and frequency. Due to the polarization rotation, induced by the electro-optical effect and modulated by the voltage level, part of the energy in the impinging pulse is reflected by the thin-film polarizer and extracted from the cavity. The repetition

rate of the voltage pulses and of the emitted pulse train can be tuned from a few kHz up to 1.1 MHz, spanning the integer submultiples of 17 MHz. Acting on the pump power and the dumping fraction, it is possible to adjust the pulse energy (up to 1 μ J) and duration, between 250 \div 400 fs, according to the different pseudo-solitonic regimes the cavity can sustain [82].

3.1.3 *Motion stages*

For the waveguide inscription process, the sample is moved with respect to the focus of the femtosecond beam. This is enabled by the following configuration: the sample is glued onto a gimbal support providing the rotation degrees of freedom around two perpendicular axes, and the support is fixed on a set of three-axes motion stages. These stages (Aerotech FIBERGlide 3D) combine air-bearings and brushless servomotors to provide exceedingly low friction between the moving parts, resulting in high translation smoothness. The position of the stages is constantly monitored as a feedback signal through optical encoders, with a nominal resolution of 1 nm. By this active control, the stages can reproduce a desired three-dimensional curved motion with an accuracy below 100 nm.

The stages are controlled through a computer and can be programmed in G-Code language (common for CNC machine tools). The maximum rate of instructions the stages can accept is 1 kHz. The mechanical shutter can also be controlled, synchronously to the sample motion, with the same software interface.

3.2 POST-PROCESSING OF THE PHOTONIC CHIPS

3.2.1 *Glass polishing and cutting*

The efficiency of launching light inside integrated optical circuits depends critically on the conditions of the input facet of the waveguides to be coupled. Quite often, the sides of the glass samples in which photonic structures are inscribed, containing the input and output cross-sections, present surface defects and roughness, or burn marks left by the laser-writing process.

In order to reduce the scattering losses and enhance the coupling to and from the waveguides, surface polishing of the sample side faces is typically performed. The polishing machine works by removing a thin surface layer of glass by contact with a moving abrasive disc. Several disks with decreasing outer roughness are employed during a single polishing process, allowing to expose high quality, smooth glass interfaces.

The glass samples can also be cut with a diamond wire saw, to select more convenient footprints or to obtain multiple copies of an

optical circuit, if the structure is longitudinally invariant. The cleaved surface is generally rough and opaque and necessitates a polishing step, if it contains input or output facets.

3.2.2 *Gold coating and resistor patterning*

The reconfigurable devices fabricated in this work employed the thermo-optical shifters introduced in [11] in order to actively control the phase delay between different optical modes and select different interference conditions. The working principle was described in section 2.4.2: thin resistors fabricated on top of an integrated photonic device are heated through Joule effect, driving a non-uniform temperature distribution in the sample. Consequently, a modulation of the refractive index, described by the thermo-optic coefficient, arises.

The fabrication of these electrical networks starts with the deposition of a thin gold layer on the top surface of the photonic chip by means of a sputter coater (Cressington 108auto). The gold film thickness, amounting typically to some tens of nanometers, is measured in real time by a thickness monitor (Cressington MTM-10).

The sample is then detached from the vacuum chamber and brought back to the same femtosecond laser fabrication setup used for waveguide inscription (section 3.1.1). A pattern of thin resistive elements terminating in broader electrical pads, with a significantly lower resistance, is etched by focusing the femtosecond laser on the golden layer.

In order to precisely align the electrical elements with the optical circuit lying in the substrate below, multiple markers, etched on the glass surface during the previous waveguide inscription process, are imaged by collecting the back reflection of the attenuated femtosecond beam (in order not to alter the thin gold layer) on a CCD camera. The retrieval of these markers allows to align the frames of reference defined in the separate fabrication steps.

For the patterning of the electrical network in the gold layer, the second harmonic of the mode-locked, cavity-dumped oscillator beam (see figure 15) was used. This choice is due to the fact that the CCD camera is significantly more sensitive at $\lambda = 515 \text{ nm}$, allowing to keep the average power of the beam much lower during the alignment procedure.

For the gold layer etching process, an average pulse energy of 100 nJ and a translation speed of 2 mm/s were found to be suitable. In order to safely insulate the electric contacts, the contours of the resistive elements were etched 6 times, with a 500 nm offset between each writing step; a final groove width of $\sim 3 \mu\text{m}$ was achieved. Furthermore, different electrical elements were separated by a 30 μm -thick, electrically floating gold region, to increase clearances in the laser pat-

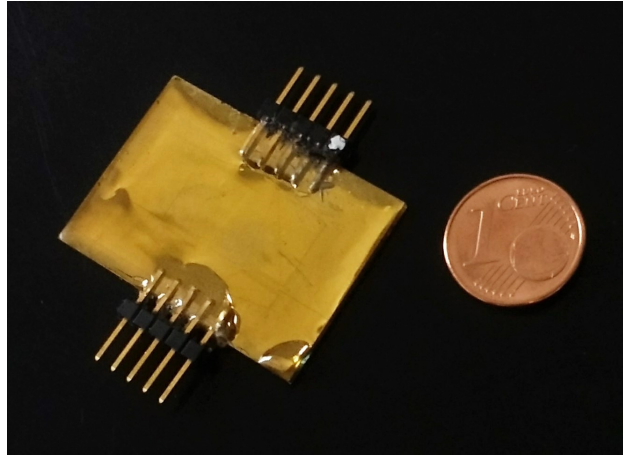


Figure 16: An integrated optics chip fabricated with FLM, with multiple thermo-optic shifters realized in a nanometric gold layer deposited on the upper surface. Sticking out of the edges, pin headers for the connection of the electric elements to external power supplies are visible. The gold layer was covered with UV glue for insulation, protection and additional robustness.

tering process and to halve the magnitude of the electric fields in the thin insulating gaps.

After the patterning process, electrical interconnections are realized by bonding the large pad sections with either copper wires or common industrial electrical connectors. During this thesis project, it was decided to employ standard *pin headers* with fixed pitch (2.54 mm), patterning the electric pads in a row, with the same width as the separation between the connectors in order to perfectly match them. The connectors were positioned on top of the pads, with the longer pins sticking out of the side of the chip, and bonded to the electrical network with an electrically conductive epoxy glue. Conventional soldering techniques were, in fact, found to irreversibly damage the delicate gold layer. Pin header connectors were preferred to copper wires due to their increased ruggedness, their simple matching with standard ribbon cables mounting insulation-displacement connectors (IDCs) and their improved insulation.

Finally, the upper surface of the chip is covered with an UV-cured resin. This step aims to protect the fragile gold electric network and to strengthen the bond with the connectors. A picture of a chip after the completion of the resistor patterning and interconnection processes is reported in figure 16.

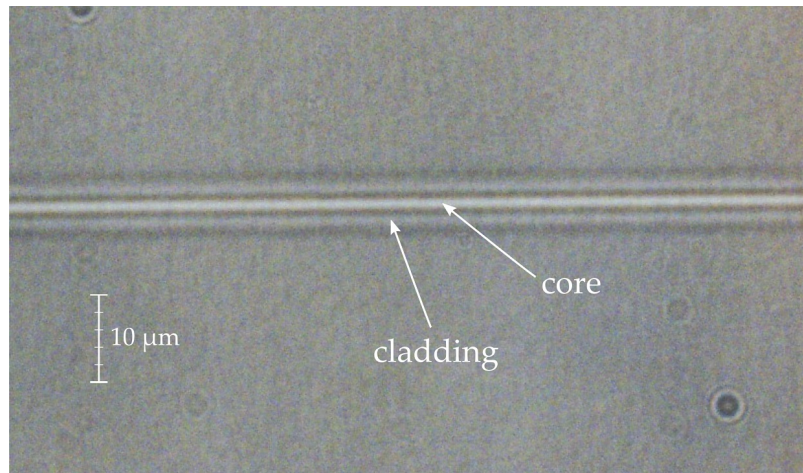


Figure 17: A waveguide written in the transverse configuration, imaged from the top with an optical microscope. Even though the refractive index profile is graded and hardly comparable to a step discontinuity, the picture shows a clear contrast between a central, core-like and an external, cladding-like region.

3.3 CHARACTERIZATION SETUPS AND TECHNIQUES

3.3.1 *Observation with optical microscope*

A first evaluation of the fabricated devices can be performed by observing the sample with an optical microscope. From the top surface of the device, by adjusting the focus to the inscription depth, the uniformity of the waveguides and the presence of interruptions or defects in the propagation direction can be assessed. An example of this kind of micrograph is provided in figure 17. The side-view of the sample allows to image the waveguide cross-section and infer qualitative information about the physical processes that contributed to the refractive index alteration (see section 2.3), as well as to check for scratches, burns and laser-induced damage on the input/output facet.

The instrument used for these analyses is a Nikon ME600 microscope, equipped with an optional Differential Interference Contrast (DIC) module, which enhances the imaging of small refractive index gradients by exploiting the interference of orthogonally-polarized rays displaced by a small offset (comparable to the microscope resolution). A high resolution CCD camera (PixeLINK B871) is mounted at the image plane and connected to a computer for digital image acquisition.

3.3.2 Coupling coherent light into the devices

To test the performance of the waveguides inscribed with the femtosecond laser, coherent light at the appropriate wavelength is launched inside the optical circuits and the modes radiating from the output facet are collected and analyzed.

For this thesis work, a distributed feedback laser diode emitting at a wavelength $\lambda = 784 \text{ nm}$ (Thorlabs L785P090 Laser Diode), with maximum optical power of 100 mW was employed.

There are mainly two configurations to couple light propagating in free-space into femtosecond laser-written waveguides. The simplest is called "*end-fire*" configuration and is depicted in figure 18a. The collimated coherent laser beam is focused with an aspheric lens or a microscope objective (OBJ) onto the input facet of the device (WG). In order to efficiently transfer the laser power to the mode guided by the device, the beam waist and the numerical aperture of the converging beam should closely match the mode mean radius and its numerical aperture ($NA \approx 0.1$).

Another possibility is given by the so-called "*fiber butt-coupling*" technique (Figure 18b). In this case, the laser light is focused through an appropriate lens or microscope objective inside a single-mode optical fiber (SMF). The other end of the fiber is cut and stripped of its protecting insulation, then peeled in order to expose the cladding and cleaved to expose a well-defined perpendicular cross-section. The exposed fiber tip is brought in close proximity to the input facet of the device, with the aid of an optical microscope. The coupling efficiency depends mostly on the matching of the profile of single mode carried by the fiber and of the one supported by the input waveguide.

The end-fire configuration is useful for quick characterizations and often presents a good coupling efficiency. Furthermore, it allows a straightforward control of the polarization of the free-propagating beam with bulk waveplates and polarizers, whereas fiber-butt coupling requires employing and regulating fiber polarization controllers. The latter technique, however, allows to evaluate the performance of the device when light is injected with an optical fiber, which is the main method for conveying nonclassical light to the chips for quantum optics experiments.

Both methods require the use of positioning systems for the coupling optics and the inscribed samples, capable of granting a stable, micrometric alignment: the coupling efficiency is in fact extremely sensitive to the geometrical matching of the input field profile and the waveguide mode. The objective (or the fiber) was mounted, in our setup, on a manual three-axes micromanipulator (Melles Griot NanoMAX), with a nominal resolution of 50 nm, while the sample was held by a four-axes manipulator (Thorlabs MBT402D/M), capa-

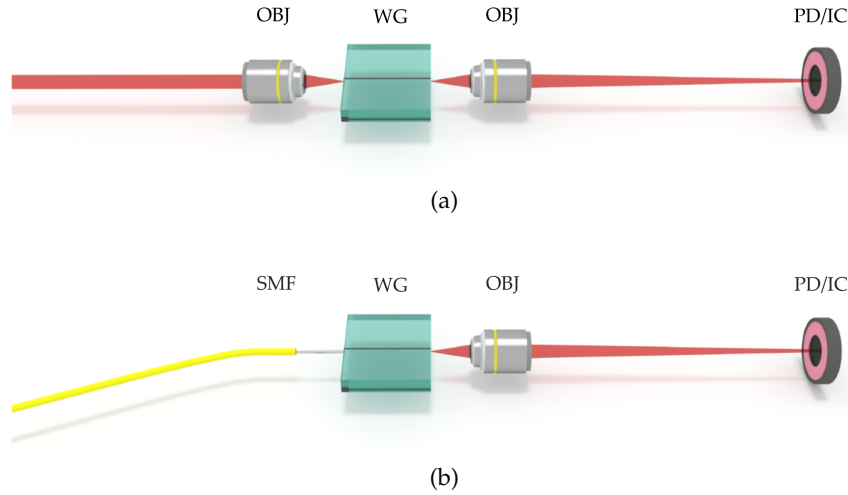


Figure 18: **(a)** End-fire coupling: coherent light is coupled in the photonic structure by focusing with a microscope objective (OBJ) onto the input facet of the waveguide (WG). At the output side, an image of the near-field modes is formed onto a power meter head (PD) or onto an imaging camera (IC). **(b)** Fiber butt-coupling: in this case, the light is fed into an optical fiber, which is cut at the other end and approached to the input facet. Image taken from [80].

ble of wider displacements in the plane transverse to the optical axis and of two tilt adjustments.

In both configurations, the output fields are collected by a microscope objective with a larger numerical aperture, mounted on a coarser two-axes manipulator, and imaged onto a CMOS camera (IC) or a photodetector (PD) connected to a power meter.

3.3.3 Losses measurement

Some of the most important figures of merit of an integrated optical device are related to the attenuation exerted to the propagating electromagnetic wave. Insertion losses (IL) are defined as the total attenuation to the optical signal due to the insertion of the device in the measurement chain. They are typically expressed in decibels, i.e.:

$$IL|_{\text{dB}} = -10 \cdot \log_{10} \left(\frac{P_{\text{out}}}{P_{\text{in}}} \right), \quad (33)$$

where P_{in} and P_{out} are respectively the optical power at the input and at the output of the device (P_{out} is the sum of the powers carried by each of the excited optical modes, if there exists more than one output port).

IL can be directly calculated in both coupling schemes of figure 18: the output light is collected on the photodetector in order to estimate

P_{out} , then the integrated optical device is removed and P_{in} is measured by focusing the light transmitted by the coupling objective or from the tip of the fiber onto the same photodetector.

IL can be decomposed in at least four different contributions: coupling losses (CL), Fresnel losses (FL), propagation losses (PL) and bending losses (BL).

- *Coupling losses* are due to the mismatch between the electric field distribution at the input facet of the waveguide, $E_{\text{in}}(x, y)$, and the electric field profile of the mode supported by the waveguide itself, $E_{\text{wg}}(x, y)$ (if no higher-order modes are supported). If the mode profiles are not identical, the light coupling will be less-than-ideal and part of the optical power will be transferred to non-guided, radiative modes. Mathematically, the coupling losses are thus expressed:

$$\text{CL}_{\text{dB}} = -10 \cdot \log_{10}(\text{OI}), \quad (34)$$

where OI is the overlap integral between E_{wg} and E_{in} ,

$$\text{OI} = \frac{|\iint E_{\text{wg}} E_{\text{in}} \, dx \, dy|^2}{\iint |E_{\text{wg}}|^2 \, dx \, dy \iint |E_{\text{in}}|^2 \, dx \, dy} \quad (35)$$

The experimental method for estimating the E_{in} and E_{wg} distributions will be described in section 3.3.4. Here, we just remark that E_{in} is easily retrieved both in the fiber-butt coupling and end-fire configurations. However, from the viewpoint of the user, the coupling efficiency when launching light from an optical fiber is more interesting, since this is the most frequent coupling method in most applications of the photonic chips. Therefore, the fiber-butt scheme is usually employed when a complete characterization of loss terms is desired.

- *Fresnel losses* are due to the mismatch between the refractive indices of the sample and of the surrounding medium (air), from which the beam is coupled and in which it is collected at the output. Any such refractive index discontinuity gives rise to a reflected wave, carrying away part of the optical power from the measurement chain (multiple reflections are very faint and are neglected in this analysis), as described by the *Fresnel equations*.

By approximating the impinging beam as a plane wave with a wavevector \vec{k} orthogonal to the interface, FL can be expressed as:

$$\text{FL}_{\text{dB}} = -10 \cdot \log_{10} \left(1 - \left(\frac{n_2 - n_1}{n_2 + n_1} \right)^2 \right), \quad (36)$$

where n_1 and n_2 are the indices of air and of the substrate, respectively (the effective refractive index of the waveguides

deviates from n_2 of a very small amount). For silicate glasses ($n_2 \approx 1.5$) and for the fabrication substrate employed during this thesis work, the Fresnel losses can be safely approximated as 0.18 dB/facet. This loss term can be suppressed in the fiber-butt configuration, at the input facet, by applying index-matching oil between the tip of the fiber and the glass surface.

- *Bending losses* arise when the waveguide is not straight but follows a curved trajectory. They are due to the distortion of the mode field profile caused by the curvature of the guiding structure; this distortion produces a partial power transfer to radiative modes in the outer side of the curve.

Bending losses increase exponentially with a decreasing radius of curvature R and are higher for waveguides with a lower index contrast Δn , due to the more gradual spatial attenuation of the evanescent field in the curved cladding regions. A simple, phenomenological discussion of the origin of bending losses is given in [83].

The estimation of BL is generally performed by fabricating a set of devices, with the same irradiation parameters, consisting of straight guides and waveguides containing curved sections, with different curvature radii R and equal longitudinal length, l_c . If the other loss terms are assumed to be equal for the different waveguides, only differences in BL influence the observed variation of the insertion losses:

$$BL|_{\text{dB/cm}} = \frac{(IL_i)|_{\text{dB}} - (IL_{\text{SWG}})|_{\text{dB}}}{l_c}, \quad (37)$$

where BL is expressed as bending losses per unit circumference trait, IL_i are the insertion losses for the waveguide with a curved section of radius R_i and IL_{SWG} are the insertion losses of straight waveguides, typically averaged on multiple devices.

- *Propagation losses* arise during the propagation of the coherent beam inside the integrated optical circuit. Since perfectly uniform waveguides in transparent dielectric materials are predicted to confine light without any power transfer to radiative modes [59], this contribution has to be ascribed to non-homogeneities in the profile of the guiding region, breaking the translation symmetry along the propagation direction and scattering part of the power of the confined mode into radiating waves. Absorption and scattering centres distributed in the substrate volume contribute as well to increasing the propagation losses.

Once the different loss terms have been estimated, the propagation losses (expressed per unit length) can be extracted as the residual contribution to the aggregate IL figure:

$$PL|_{\text{dB/cm}} = \frac{IL|_{\text{dB}} - CL|_{\text{dB}} - 2FL|_{\text{dB}} - l_c BL|_{\text{dB/cm}}}{l}, \quad (38)$$

where l is the length of the waveguide or photonic structure. Fresnel losses have been counted twice, once for each refractive index discontinuity.

3.3.4 *Imaging of the mode profile*

The spatial profile of the mode supported by the waveguides, $E_{\text{wg}}(x, y)$, carries crucial information about the confinement of light, is needed to assess the coupling losses (section 3.3.3), influences the magnitude of the bending losses and can be employed to indirectly evaluate the alteration of the refractive index produced by the femtosecond laser focusing. In particular, this last analysis can be performed by substituting the near-field mode profile in the Helmholtz equation [84]:

$$n^2(x, y) = n_e f f^2 - \frac{\lambda^2}{4\pi^2} \frac{\nabla^2 E_{\text{wg}}(x, y)}{E_{\text{wg}}(x, y)} \quad (39)$$

Additionally, this technique is used to validate the requirement that a single mode is supported by the waveguide at the wavelength of interest, by evaluating whether higher-order transverse modes are excited when the input field is slightly displaced. For most integrated quantum photonics applications, single-mode operation is necessary in order to properly engineer the device operation and to avoid additional bending and propagation losses.

In order to measure the intensity profile of the guided mode, the device is coupled in either of the configurations described in figure 18. Then, the end facet of the sample is imaged onto a high sensitivity, monochromatic CMOS camera (Edmund Optics EO-1312M, 8-bit, 1280×1024 pixels), with a microscope objective having a larger numerical aperture than the waveguide, in order to collect most of the light radiated from its output cross-section. Paying particular attention to exploiting the full extent of the camera dynamic range without saturating the most exposed pixels, the intensity profile I_{wg} is digitally acquired for later numerical elaboration.

If only a single mode is supported by the waveguide, the theory guarantees that the field profile will not show any sign inversion. Therefore, the field spatial distribution can be numerically retrieved from the intensity map:

$$|E_{\text{wg}}(x, y)| \propto \sqrt{I_{\text{wg}}(x, y)} \quad (40)$$

The proportionality constant, left out of equation 40, carries information about the total power of the output field and can be neglected for the evaluation of normalized quantities (such as OI in equation 35).

Estimating the coupling losses of the fabricated device (in the fiber-butt coupling configuration) requires the calculation of the overlap integral of equation 35, in which the input field appears. $E_{in}(x, y)$ is retrieved by removing the photonic device and bringing the tip of the fiber close to the imaging objective, so that an image of the near-field fiber mode is formed onto the camera. During this procedure, particular care has to be taken not to change the distance between the objective and the camera, so that the magnification ratio is kept fixed; then E_{in} and E_{wg} can be directly compared and substituted into 35.

AN INTEGRATED-OPTICS PLATFORM FOR HAMILTONIAN LEARNING EXPERIMENTS

This chapter will introduce the concept at the basis of the integrated optics devices developed in this thesis work, and provide a schematic description of their optical layout.

The work is part of a collaboration between the Femtosecond Laser Micromachining group of IFN-CNR in Milan, headed by Dr. Roberto Osellame, and the Quantum Optics group of Prof. Fabio Sciarrino and Prof. Paolo Mataloni, based at La Sapienza University in Rome, that constructs and operates the single-photon sources used for quantum experiments.

Section 4.1 will introduce the Hamiltonian learning experiments that we aim to perform with the devices. Section 4.2 will describe the interferometer generating the direct transformation (fabricated on a first photonic chip) and report numerical studies about the set of unitaries it can implement. Section 4.3 will disclose the structure of the interferometer capable of producing the inverse transformation (fabricated on a second photonic chip) and detail its working principles.

4.1 MOTIVATION FOR THE WORK

The development of quantum simulation and computation involves the control and exploitation of increasingly complex quantum mechanical system, with an increasing number of particles and degrees of freedom, and growing dimensions of the associated Hilbert space. These technological advances solicit the need of instruments for evaluating the effective dynamics of quantum systems and certifying the correct implementation of gates and unitary operations required for quantum computation.

The Hamiltonian learning algorithm [35] described in section 1.2.3 provides a computationally efficient procedure to infer the Hamiltonian of an uncertified quantum object. This work aims to produce a photonic quantum simulation platform able to demonstrate the various versions of Hamiltonian learning listed in section 1.2.3.2 and assess their performance. Specifically, we develop integrated optical circuits that implement unitary transformations on single- or multiple-photon states, akin to quantum computation gates or time evolution operators.

Our experimental platform consists of two separate photonic chips. Into the chips, reconfigurable multiport interferometers were fabricated with femtosecond laser micromachining. The device symmetry allows to conduct experiments with two distinct methods for *likelihood evaluation* (see section 1.2.3.2), schematically illustrated in figure 19:

- By operating the two devices in parallel, one can treat the first as a black-box transformation and employ the second as a simulator. The reconfigurable interferometers, thus operated, are capable of implementing the same set of unitary transformations. This configuration allows to characterize the likelihood function according to the QLE protocol.
- By flipping the second device, exchanging the input and output ports, one can use it in order to realize the *inverse transformation* of the first device. More details about the optical layout that makes this inversion possible will be provided in section 4.3.2. With this configuration, one can transfer directly the quantum state encoded by the first device to the second, allowing to evaluate the matching of direct (T^+) and inverse (T^-) evolution at the output. This scheme is closely related to the IQLE protocol.

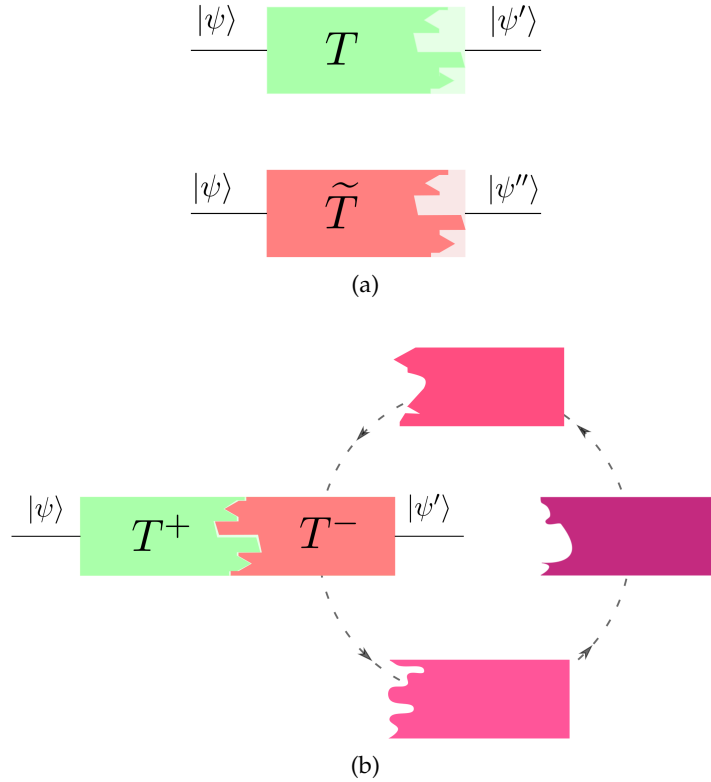


Figure 19: Two different configurations for the implementation of Hamiltonian learning with the same quantum photonic devices.

(a) Parallel operation of the devices; learning the unitary T with the reconfigurable simulator \tilde{T} performing quantum likelihood evaluation (QLE). **(b)** Serial operation of the devices: the inversion the forward evolution T^+ by T^- is sought by exploring a set of candidate unitary transformations. Light is coupled directly from T^+ to T^- .

4.2 RECONFIGURABLE UNITARY TRANSFORMATION

4.2.1 Interferometric layout

The direct unitary transformation T is performed by an interferometer fabricated in boro-aluminosilicate glass with femtosecond laser waveguide inscription. The interferometer consists of an array of waveguides and directional couplers (playing the role of beam splitters, see appendix B for reference), linked with a specific geometrical arrangement. The device encompasses five input and five output ports.

The number of waveguides in the interferometer was chosen in order to keep the structure simple enough to characterize. Furthermore, previous works with multi-mode interferometers suggested that FLM fabrication tolerances allowed a good control of the optical parameters up to this level of structural complexity.

Figure 20 depicts schematically the layout of the reconfigurable direct transformation. The interferometer contains eight beam splitters,

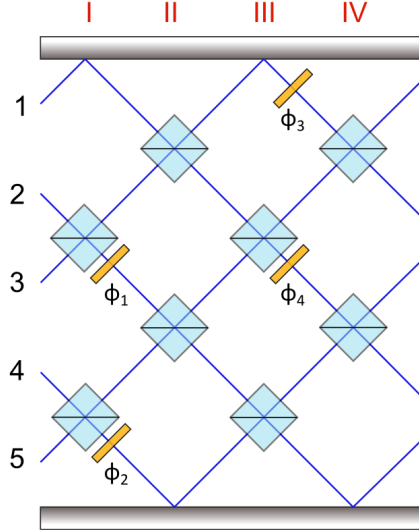


Figure 20: Pictorial layout of the interferometer performing the direct unitary transformation (T or T^+ in figure 19). The electromagnetic fields of modes 1-5 are mixed through the successive columns of beam splitters I-IV. Light blue diamonds represent balanced ($R = T = 50\%$) beam splitters (directional couplers) and yellow rectangles stand for reconfigurable phase shifts.

arranged in four successive steps (columns). At each step, four modes interact in couples, impinging on the input ports of two balanced ($R = T = 50\%$) beam splitters, while one of the outermost modes propagates unaltered. The couples of combining modes alternate in even and odd steps; along the propagation direction an optical mode interacts with its upper (lower) neighbor, then with its lower (upper) and so on. This beam splitter arrangement is the same as the one proposed in [85] for the realization of arbitrary unitary optical gates, granting advantages in terms of robustness to losses and footprint with respect to the older design by Reck et al. [8] that will be introduced in section 4.2.2. However, in order to implement arbitrary unitary operations, both the aforementioned designs require the ability of controlling and setting each beam splitter reflectance. In our case, all the beam splitters were designed to be balanced, for ease of fabrication and in order to keep the optical paths in the different waveguides uniform. Furthermore, a balanced optical splitting grants the maximum *visibility* for a Mach-Zehnder interferometer¹. Since the structure at hand contains many Mach-Zehnder-like interferometric rings, balanced beam splitters grant a high sensitivity of

¹ The interference visibility is defined as the ratio of the light intensity contrast, as phase is varied, over the total intensity launched in the interferometer: $v = (I_{\max} - I_{\min}) / I_{\text{tot}}$

the input/output power routing and splitting ratios to the controlled parameters $\varphi_{1,\dots,4}$. The consequences of this choice on the unitary operations performed are detailed in section 4.2.2.

We chose to control actively four phase terms. This is in fact the minimum number needed to address each interferometric ring in our layout (see figure 20). By interferometric ring we mean here the optical paths linking any couple of beam splitters, where light is split at the first and recombined on the second, resulting in constructive or destructive interference. It can be proven that any phase difference other than those depicted in figure 20 could be traced back to $\varphi_{1,\dots,4}$ or to phase terms at the input/output of the interferometer, that cannot influence any measurement outcome, either with classical or quantized states of light. Phase shifters are realized with resistive heaters, devices that are capable of influencing the refractive index profile inside the sample through temperature control, exploiting the *thermo-optical effect*. Such active elements were already introduced in section 2.4.2.

The operation of the circuit can be analyzed using a matrix formalism (see also appendix B). In detail, the effect of a balanced beam splitter on the impinging fields (in phasor notation) can be represented by the matrix:

$$\frac{1}{\sqrt{2}} \begin{pmatrix} 1 & i \\ i & 1 \end{pmatrix} \quad (41)$$

By extension, it is easy to write the matrices describing the mode mixing at even and odd steps of the interferometer, simply looking at which modes are exchanging power at a given cross-section. Even and odd steps are described by the block-diagonal matrices E and O, as follows:

$$E = \frac{1}{\sqrt{2}} \begin{pmatrix} 1 & i & 0 & 0 & 0 \\ i & 1 & 0 & 0 & 0 \\ 0 & 0 & 1 & i & 0 \\ 0 & 0 & i & 1 & 0 \\ 0 & 0 & 0 & 0 & \sqrt{2} \end{pmatrix}, \quad O = \frac{1}{\sqrt{2}} \begin{pmatrix} \sqrt{2} & 0 & 0 & 0 & 0 \\ 0 & 1 & i & 0 & 0 \\ 0 & i & 1 & 0 & 0 \\ 0 & 0 & 0 & 1 & i \\ 0 & 0 & 0 & i & 1 \end{pmatrix} \quad (42)$$

Phase shifts, controlled or intrinsic to the interferometer, between the interaction steps can be represented with diagonal unitary matrices of the form:

$$L = \begin{pmatrix} e^{i\phi_1} & 0 & 0 & 0 & 0 \\ 0 & e^{i\phi_2} & 0 & 0 & 0 \\ 0 & 0 & e^{i\phi_3} & 0 & 0 \\ 0 & 0 & 0 & e^{i\phi_4} & 0 \\ 0 & 0 & 0 & 0 & e^{i\phi_5} \end{pmatrix} \quad (43)$$

According to the layout of the reconfigurable phase shifts in figure 20, two such L matrices can be identified, interposed between steps I and II and between steps III and IV:

$$L_1 = \begin{pmatrix} 1 & 0 & 0 & 0 & 0 \\ 0 & 1 & 0 & 0 & 0 \\ 0 & 0 & e^{i\varphi_1} & 0 & 0 \\ 0 & 0 & 0 & 1 & 0 \\ 0 & 0 & 0 & 0 & e^{i\varphi_2} \end{pmatrix} \quad L_2 = \begin{pmatrix} e^{i\varphi_3} & 0 & 0 & 0 & 0 \\ 0 & 1 & 0 & 0 & 0 \\ 0 & 0 & e^{i\varphi_4} & 0 & 0 \\ 0 & 0 & 0 & 1 & 0 \\ 0 & 0 & 0 & 0 & 1 \end{pmatrix} \quad (44)$$

(neglecting potential passive phase shifts).

With these definitions, the overall transformation is written as

$$T^+ = EL_2OEL_1O \quad (45)$$

and the normalized distribution of optical power at the output ports can be derived from $\mathcal{Z} : \mathcal{Z}_{i,j} = |T_{i,j}^+|^2$. In fact, the i^{th} column of \mathcal{Z} represents the fraction of optical power in each output port, when light is coupled from the i^{th} input of the interferometer. In closed form:

$$T_+ = \frac{1}{4} \begin{pmatrix} 2e^{i\varphi_3} - \sqrt{2} & i(1 - e^{i\varphi_1} + \sqrt{2}e^{i\varphi_3}) & -(1 + e^{i\varphi_1} + \sqrt{2}e^{i\varphi_3}) & -i & 1 \\ i(2e^{i\varphi_3} + \sqrt{2}) & 1 - (e^{i\varphi_1} + \sqrt{2}e^{i\varphi_3}) & i(1 + e^{i\varphi_1} - \sqrt{2}e^{i\varphi_3}) & -1 & -i \\ -\sqrt{2}e^{i\varphi_4} & i(e^{i\varphi_4} + e^{i\varphi_1}(e^{i\varphi_4} - 1)) & e^{i\varphi_1}(e^{i\varphi_4} - 1) - e^{i\varphi_4} & i(1 + e^{i\varphi_4} - \sqrt{2}e^{i\varphi_2}) & -(1 + e^{i\varphi_4} + \sqrt{2}e^{i\varphi_2}) \\ -\sqrt{2}ie^{i\varphi_4} & -e^{i\varphi_1}(e^{i\varphi_4} + 1) - e^{i\varphi_4} & i(e^{i\varphi_1} + e^{i\varphi_4}(e^{i\varphi_1} - 1)) & 1 - (e^{i\varphi_4} + \sqrt{2}e^{i\varphi_2}) & i(1 - e^{i\varphi_4} + \sqrt{2}e^{i\varphi_2}) \\ 0 & -\sqrt{2}ie^{i\varphi_1} & -\sqrt{2}e^{i\varphi_1} & i(2e^{i\varphi_2} + \sqrt{2}) & 2e^{i\varphi_2} - \sqrt{2} \end{pmatrix} \quad (46)$$

5 of the 25 unitary matrix elements are fixed and are not affected by controlling the phase shifters. Moreover, the absolute value of 4 additional elements cannot be changed: only their phase depends on the controlled parameters. The matrix is symmetric under reflection along the secondary diagonal, provided that φ_1 is exchanged with φ_4 , and φ_2 with φ_3 . This correspondence expresses the symmetry of the interferometer upon rotations of 180° around an axis perpendicular to the plane of figure 20.

This ideal representation will be extensively used for the numerical simulations and studies presented in the following sections, and assumes balanced beam splitters, negligible losses and uniform optical paths of modes 1 – 5. These simplistic hypotheses will be critically examined in the device characterization process.

4.2.2 The set of accessible transformations

As mentioned, a general method for implementing a $N \times N$ unitary matrix with a multiport interferometer was proposed by Reck et al.

in 1994 [8]. The procedure consists of sequentially decomposing the $N \times N$ matrix into a product of unitary matrices of the same dimensions, but acting as the identity on all vector components but two. These basic factors represent a two-modes beam splitter with a precise reflectance followed by a phase shift on one of the output arms. Alternatively, the same transformation can be obtained with a Mach-Zehnder interferometer built with two balanced beam splitters and a tunable phase difference on the path split, again, followed by a phase shift (see panel c. of figure 21). Mathematically, the unitary matrix U is decomposed as

$$U = L \cdot \prod_{(m,n) \in S} U_{(m,n)}, \quad (47)$$

where L is a diagonal matrix, with elements $e^{i\phi_i}$ lying on the unit circle, representing phase terms at the output ports of the interferometer, $U_{(m,n)}$ is a unitary matrix mixing modes m and n only and S is a specific ordered sequence of two-modes transformations.

The decomposition by Reck et al. chooses S such that the interferometer is arranged in a triangular mesh of beam splitters and phase shifters. A more recent proposal [85] introduced a different, rectangular configuration, with some advantages in terms of robustness to losses and spatial extent. Both decomposition schemes require $\frac{N(N-1)}{2}$ beam splitters and phase shifters to construct U . The interaction layout and sequence of mode mixing for the two decomposition schemes is depicted in figure 21.

In our case, the interferometer consists of 8 beam splitters, whose reflectance is fixed to a specific value. Instead, 10 variable-reflectance beam splitters would be needed in general to generate any 5×5 unitary transformation (a fifth column of two beam splitters would suffice to reproduce the general rectangular layout). Furthermore, only 4 phase shifters will be operated, instead of the 10 arising from the Reck decomposition scheme. It is then clear that the subset of discrete, 5×5 unitary transformations that can be implemented with our interferometer design is not exhaustive, and many transformations will not be reached by simply acting on the four "knobs" $\varphi_{1,\dots,4}$.

A first, relevant path of inquiry was to investigate how the space of 5×5 unitary matrices is sampled by our reconfigurable interferometer. With four independent parameters, the set of transformations that can be implemented is of course four-dimensional. We tried to answer the question of how much two unitary evolutions can differ when we act only on these four knobs.

To this end, we extracted random values (with a uniform distribution in the $[0; 2\pi]$ interval) for the phase parameters $\varphi_{1,\dots,4}$, to generate random matrices in couples. These matrices were first reduced to a common form, with the first row and first column purely real, by pre- and post-multiplication with diagonal unitaries. The aim was to

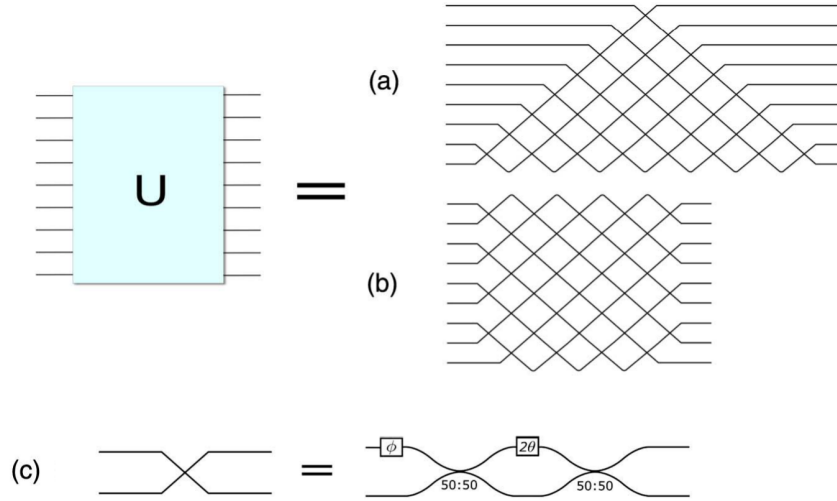


Figure 21: A universal N -mode multiport interferometer U can be implemented with a mesh of $N(N-1)/2$ beam splitters such as (a) the triangular layout proposed in [8] and (b) the rectangular layout illustrated in [85]. Lines represent optical modes, while crossings between modes correspond to variable beam splitters. The latter can be implemented by a Mach-Zehnder interferometer realized with balanced directional couplers, preceded by a phase shift on one of the input modes, as depicted in panel (c). Image adapted from [85].

make our analysis insensitive to arbitrary phase shifts at the input or output of the interferometer, which indeed do not affect the output probability distributions when injecting Fock states.² Then we evaluated how much the matrices differ by using two different mathematical notions of *distance*.³ In particular, we used both the element-wise *Frobenius norm*:

$$\|A\|_F = \sqrt{\sum_{i,j=1}^5 |a_{ij}|^2} \quad (48)$$

and the *variational distance* (also known as *trace distance*) [4] between the single-photon scattering probability distributions at the interferometer output. As mentioned in section 4.2.1, the single-photon scattering distribution, equivalent to the distribution of optical power when coherent light is coupled to one input port, is obtained by taking the square modulus of each matrix element. Once the two discrete

² Fock states are states of the electromagnetic field for which the number of photons in a certain mode has a well defined expectation value and no variance; eigenstates of the number operator $\hat{N} = \hat{a}^\dagger \hat{a}$.

³ The distance between two matrices A and B is the operation $\|A - B\|$, reliant on the definition of a norm $\|\cdot\|$ on the Hilbert space of 5×5 matrices.

probability distributions p_k and q_k are calculated, the variational distance is given by:

$$d = \frac{1}{2} \sum_{k=1}^5 |p_k - q_k| \quad (49)$$

In our case, we averaged the variational distance over the 5 possible input ports of the interferometer and their corresponding output distributions.

The random pick was repeated numerous times to obtain a distribution of distances between couples of matrices implemented by our interferometer. To establish a significant comparison, we assume that the maximum possible variability between extracted unitary matrices is either obtained by picking at random (uniformly) the parameters in the Reck layout or, with a more mathematical perspective, by sampling matrices according to the *Haar measure* [86], i.e. a method that permits to extract $N \times N$ matrices with a uniform probability. We employed both methods to assess the performance of our interferometer.

In the first case, we repeated our procedure for a Reck interferometer with 5 input/output ports, i.e., extracting randomly all the ten independent phase shifts and the ten independent beam splitter transmittances necessary for the construction. In the second case, we performed random sampling according to the Haar measure on 5×5 matrices. The numerical procedure is computationally simple, requiring the use of the orthogonal-triangular matrix decomposition [86]. Again, the resulting complex matrices were simplified to a form with all the elements on the first row and column purely real.

Figure 22a. shows the comparison between the distributions of Frobenius distance resulting from our class of interferometers and the Reck design. The Reck scheme shows a slightly larger average distance ($\bar{d}_T = 2.43$, $\bar{d}_R = 2.57$) and a more symmetrical distribution (probably due to higher number of independent parameters - 20 against 4). The Haar-sampled matrices show a yet slightly larger average distance ($\bar{d}_H = 2.59$), but the overall shape is almost identical to the Reck distribution.

Figure 22b. provides a similar comparison, but this time the simulations were run by evaluating the variational distance (see equation 49) between the probability distributions arising from the matrices. The results are similar: our interferometric layout corresponds to a variational distance distribution slightly displaced towards lower values ($\bar{d}_T = 0.36$, $\bar{d}_R = 0.46$, $\bar{d}_H = 0.44$). Surprisingly, this time the Haar-sampled matrices exhibit a slightly lower average distance compared to the Reck distribution. The Haar distribution is also characterized by a lower variance, being more peaked around its average value. We believe that these results overall show that the chosen layout with only four available phase shifters is able to sample adequately the

space of 5×5 unitary transformations, providing a good representation of its general structure.

We also investigated what happens if we vary the number of controlled parameters. Figure 23 shows how the average distance (with the Frobenius definition) increases by controlling a sequentially higher number of independent parameters. Specifically, this simulation was performed by allowing first only φ_1 to vary, then adding in sequence also φ_2 , φ_3 and φ_4 . The plot shows how the addition of the first three degrees of freedom increases dramatically the diversity of the matrices; by the time the fourth phase is released, the average distance is almost equal to the one obtained with the 20-parameters Reck interferometers and with random unitaries picked with a uniform probability distribution. For completeness, we also tried to add the phases $\varphi_1 \dots \varphi_4$ in a different order, with similar results. This further confirms that our layout is a good compromise between generality and simplicity of fabrication and operation.

4.2.3 Approximation of a generic unitary matrix

Another analysis was performed in order to gain a more complete understanding of the embedding of our accessible set of matrices in the space of all possible 5×5 unitary transformations. We assessed how well our reconfigurable design could approximate a generic random unitary transformation.

Random 5×5 unitaries were extracted according to the Haar measure. The matrices were all brought to a common form, with all the elements in the first row and column real (like in section 4.2.2), to make the analysis insensitive to differences that would not be experimentally observable. A maximization algorithm was then run, aiming to find those parameters $\varphi_1, \dots, \varphi_4$ that optimized the *fidelity* of the reconfigurable interferometer transformation to the extracted unitary.

The fidelity F is a scalar figure of merit bounded between $0 \leq F \leq 1$ commonly used in quantum information to evaluate the similarity between probability distributions, quantum gates or quantum states (expressed as density matrices, see appendix A) [4]. The higher the fidelity, the more similar are the examined transformations or distributions. In our case, the fidelity was computed with the prescription:

$$F = \frac{|\text{tr}(T^+(\varphi_1, \dots, \varphi_4) \cdot U^\dagger)|}{5}, \quad (50)$$

where T^+ is the custom interferometer transformation and U is the random unitary to approximate.

The optimization algorithm employed was a search method for unconstrained minimization (Nelder-Mead simplex method), less sensitive to local minima than derivative-based methods (e. g. gradient descent). The optimization run was preceded by the evaluation of the

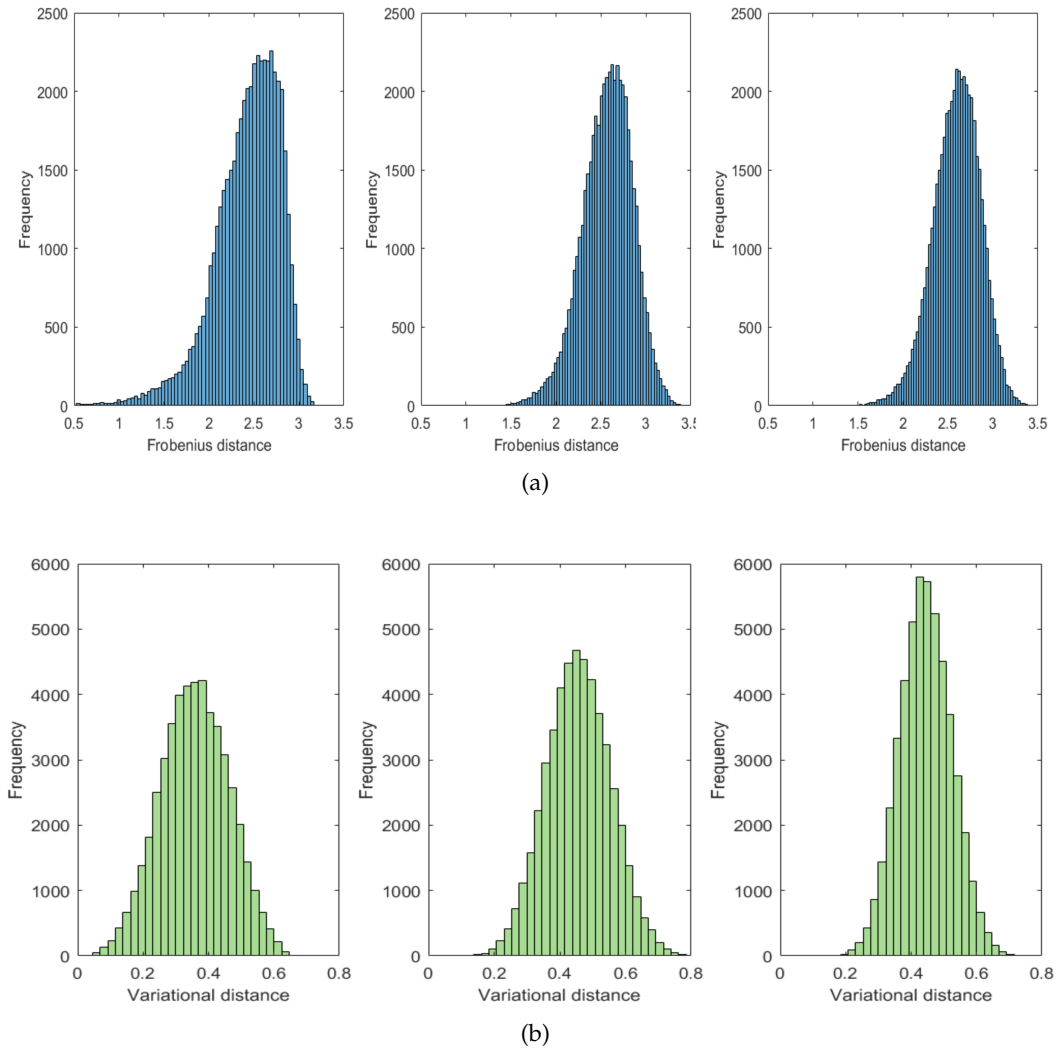


Figure 22: **(a)** Comparison of distance distribution calculated in the Frobenius norm. Left: our custom transformation, with four variable phase shifts. Center: Reck design, with ten variable transmittances and ten variable phase shifts. Right: Uniformly distributed unitary matrices extracted according to the Haar measure. **(b)** Comparison of variational distance distributions between the discrete probability distributions of single-photon scattering arising from the unitaries. Left: our custom transformation, with four variable phase shifts. Center: Reck design, with ten variable transmittances and ten variable phase shifts. Right: Uniformly distributed unitary matrices extracted according to the Haar measure.

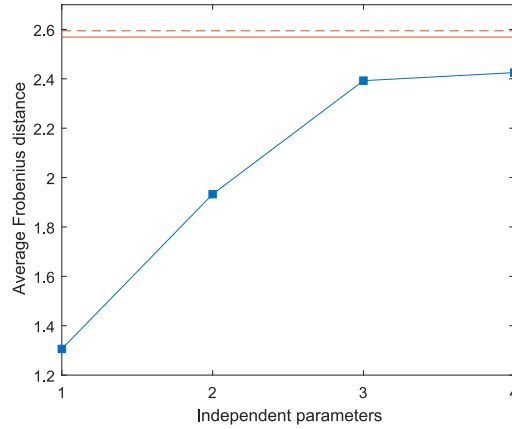


Figure 23: Growth of the average distance between random unitaries produced by our custom design as 1,2,3 and 4 parameters are allowed to change. The red continuous line indicates the average distance for random Reck unitaries, with ten variable transmittances and ten variable phase shifts ($\bar{d}_R = 2.57$). The red dashed line represents the yet higher average distance for random unitaries extracted according to the Haar measure.

fidelity on a coarse-mesh phase grid, aiming to find a good starting point for the minimization procedure.

As expected, the approximation power of our interferometer is limited. The average fidelity of the closest transformation, calculated on 10^4 starting unitary matrices, is $\bar{F} = 0.67$, indicating a rather poor approximation performance on average. This was expected, since our operational layout offers only 4 independent parameters, against the 20 that would be required to realize a generic 5×5 unitary.

In conclusion, these numerical studies allowed us to state that the set of unitary transformations that can be accessed with our interferometer design is of course non-universal, but rather quite limited in extent. Nevertheless, it provides a good sampling of the unitary matrices space: the available class of transformations describes well the overall features of the much vaster space of generic unitaries.

4.3 INVERSE EVOLUTION

Once established an interferometric structure for our direct unitary transformation, we seek a layout that can invert that evolution, implementing a version of the matrix inverse. Since we work with unitary matrices, we strive for a structure capable of achieving $T^- = (T^+)^{\dagger}$ for any possible choice of the internal phase shifts.

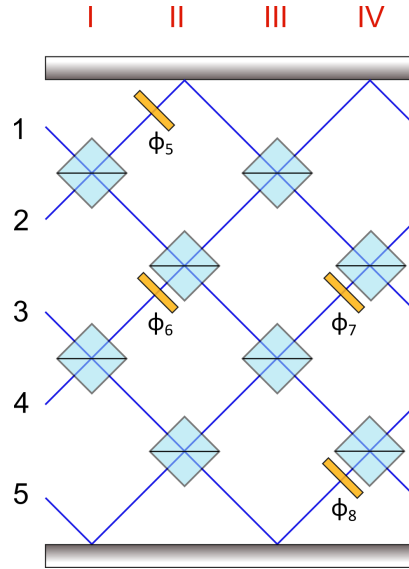


Figure 24: Pictorial layout of the interferometer performing the inverse unitary transformation (\tilde{T} or T^- in figure 19). The electromagnetic fields of modes 1-5 are mixed through the successive columns of beam splitters I-IV. Light blue diamonds represent balanced ($R = T = 50\%$) beam splitters (directional couplers) and yellow rectangles stand for reconfigurable phase shifts.

4.3.1 Layout and symmetries

As will be proven shortly, a multiport interferometer capable of implementing T^- is a version of the direct reconfigurable transformation, mirrored along the horizontal axis of figure 20. The layout still contains eight beam splitters and the same two-modes interaction alternation (see figure 24). The odd steps in this device have the same form of even steps in the direct interferometer and vice versa. Phase shifters are placed exactly in a position that mirrors their arrangement in the first device. In matrix notation:

$$T^- = OL_4EOL_3E \quad (51)$$

The reflection symmetry is naturally expressed by the matrix structure of T^- . Let us define Q as an orthogonal matrix that swaps mode 1 with mode 5 and mode 4 with mode 2, describing the act of flipping the interferometer layout along a horizontal axis:

$$Q = \begin{pmatrix} 0 & 0 & 0 & 0 & 1 \\ 0 & 0 & 0 & 1 & 0 \\ 0 & 0 & 1 & 0 & 0 \\ 0 & 1 & 0 & 0 & 0 \\ 1 & 0 & 0 & 0 & 0 \end{pmatrix} \quad (52)$$

T^- coincides with a T^+ transformation, after the modes are flipped both at the input and at the output ports (neglecting the active phase shifters, for simplicity):

$$T^- = QT^+Q^{-1} = QT^+Q, \quad (53)$$

because $Q = Q^{-1}$. Since the action of Q on T^+ coincides to simply permuting rows (when pre-multiplying) or columns (when post-multiplying), the overall structure of the two matrices is related by a point reflection about the central element $(3, 3)$, i. e. $T_{i,j}^- = T_{6-i,6-j}^+$.

Finally, let us note that the mirror symmetry implies that the inverse interferometer, if flipped of 180° and operated from the output ports, implements the direct unitary T^+ . This consideration validates the use of the inverse device also as \tilde{T} in a QLE learning experiment (see panel **a.** of figure 19).

4.3.2 Simplification of the interferometric structure

In order to perform IQLE Hamiltonian learning (panel **b.** of figure 19), $T^- = (T^+)^\dagger$ must hold for some values of $\varphi_5, \dots, \varphi_8$. We will show here the conditions for this situation to be realized, by showing how the two interferometers arranged in series (with light from the output ports of the direct device coupled into the input ports of the inverse device) can be rendered equivalent to an identity operation.

The correct inversion of the direct transformation requires $\pm\pi$ phase shifts either to all odd or all even modes in the joint region between the two photonic circuits. In the following chapter, we will describe how this shift is provided with thermo-optical shifters patterned above the initial waveguide segments upon the second device.

In fact, by approaching the array of beam splitters and phase shifters with its mirror image, two Mach-Zehnder interferometers, involving the central modes only, appear in the middle (25a.). By giving a π phase difference to adjacent modes, the Mach-Zehnders just replicate at their outputs the same field configurations that are excited at the input, with the addition of π phase shifts⁴. This simplification gives rise to another couple of Mach-Zehnder interferometers, already with the correct phase relation in order to collapse in the same way (25b.), provided that the reconfigurable phase shifts acting on the same modes cancel out ($\varphi_3 + \varphi_5 = 0$, $\varphi_4 + \varphi_6 = 0$).

⁴ Let us consider light launched on the first input mode of the first beam splitter mirror. The propagation inside the Mach-Zehnder interferometer with a π internal imbalance is described algebraically as:

$$\begin{pmatrix} \sqrt{R} & i\sqrt{T} \\ i\sqrt{T} & \sqrt{R} \end{pmatrix} \begin{pmatrix} -1 & 0 \\ 0 & 1 \end{pmatrix} \begin{pmatrix} \sqrt{R} & i\sqrt{T} \\ i\sqrt{T} & \sqrt{R} \end{pmatrix} \cdot \begin{pmatrix} 1 \\ 0 \end{pmatrix} = \begin{pmatrix} -1 \\ 0 \end{pmatrix}$$

We can see that this condition does not actually require 50 – 50 beam splitters, as long as the two have an identical reflectance.

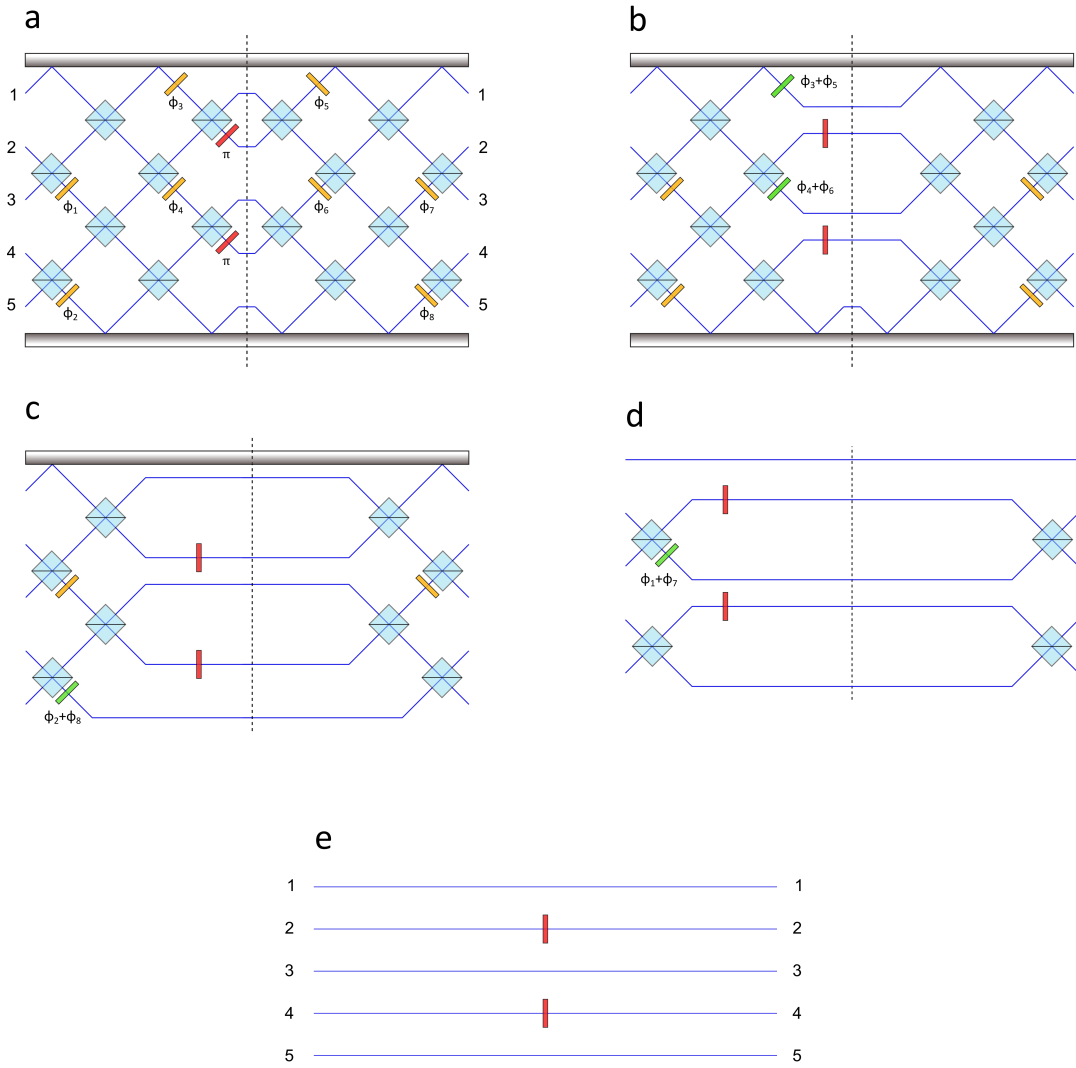


Figure 25: The cascade of the two interferometers is shown to be equivalent to an identity transformation: the insertion of π delays on the even-numbered modes causes all Mach-Zehnder rings to sequentially collapse.

This process continues in a cascade (25c. and 25d.), assuming that the remaining reconfigurable phase shifts are compensated by their mirror-symmetric term on the opposite device (green phase shifts in figure 25). The double array is finally simplified to a transformation equivalent to the identity, with just the addition of π phase shifts on half of the modes involved (25e.).

Recapitulating, the following conditions on the reconfigurable phases have to be enforced for the implementation of the inverse matrix:

$$\begin{cases} \varphi_5 = -\varphi_3 \\ \varphi_6 = -\varphi_4 \\ \varphi_7 = -\varphi_1 \\ \varphi_8 = -\varphi_2 \end{cases} \quad (54)$$

This pictorial intuition can be also proved more rigorously with linear algebra, extending the validity of the method for inverse construction to larger arrays, with n modes and k interaction steps. In particular, we will describe in detail here only the odd- n , even- k case for simplicity: in every other case, the definitions are slightly different but the proof proceeds in an identical fashion.

Let E and O be $n \times n$ block-diagonal transfer matrices representing the interaction between n modes in even and odd steps of the interferometric cascade, totalling k steps.

$$E = \frac{1}{\sqrt{2}} \begin{pmatrix} 1 & i & & & & \\ i & 1 & & & \emptyset & \\ & & \ddots & & & \\ & & & 1 & i & \\ \emptyset & & & i & 1 & \\ & & & & & \sqrt{2} \end{pmatrix} \quad (55)$$

$$O = \frac{1}{\sqrt{2}} \begin{pmatrix} \sqrt{2} & & & & & \\ & 1 & i & & \emptyset & \\ & i & 1 & & & \\ & & & \ddots & & \\ \emptyset & & & & 1 & i \\ & & & & i & 1 \end{pmatrix} \quad (56)$$

We define P as the diagonal matrix

$$P = \begin{pmatrix} 1 & & & & \\ & -1 & & \emptyset & \\ & & 1 & & \\ \emptyset & & & \ddots & \\ & & & & 1 \end{pmatrix} \quad (57)$$

describing the π phase difference introduced along the axis of symmetry.

It is easy to see, since the single blocks on the diagonals describe the components of a Mach-Zehnder interferometer with a π difference, that

$$\text{EPE} = \text{OPO} = \text{P} \quad (58)$$

Let L_m be a diagonal unitary matrix similar to 43 carrying a phase shift to each mode: $L_{m,ij} = e^{i\varphi_{m,j}} \cdot \delta_{ij}$. Since L_m is diagonal, it commutes with P and $L_m L_m^* = \mathbb{1}$. The transformations produced by the two facing interferometers (respectively T^+ and T^-) can be written as:

$$T^+ = \prod_{i=1}^{k/2} (L_{2i} E L_{2i-1} O), \quad T^- = \prod_{i=k/2}^1 (O L_{2i-1}^* E L_{2i}^*) \quad (59)$$

Here, the products are carried out right to left. Note that we have built the second interferometer so that it contains the opposite phase terms with respect to the first ones (see equation 54), i. e. for each L_m in the first interferometer there is an L_m^* factor in the second one.

When we cascade the transformations, the expression simplifies in a manner that is completely equivalent to the pictorial proof shown before, from the middle towards the edges:

$$\begin{aligned} T^- P T^+ &= \left(\prod_{i=k/2}^1 (O L_{2i-1}^* E L_{2i}^*) \right) P \left(\prod_{i=1}^{k/2} (L_{2i} E L_{2i-1} O) \right) = \\ &= O L_1^* E L_2^* \cdots E P (L_k^* L_k) E \cdots L_2 E L_1 O = \\ &= O \cdots O L_{k-1}^* (EPE) L_{k-1} O \cdots O = \\ &= O \cdots O P (L_{k-1}^* L_{k-1}) O \cdots O = \\ &= O \cdots E L_{k-2}^* (OPO) L_{k-2} E \cdots O = \\ &= \dots = \text{OPO} = \text{P} \end{aligned} \quad (60)$$

The final result is equivalent to the identity transformation, apart from phase shifts at the outputs.

We can observe that the inverse transformation closely resembles a time-reversed copy of T^+ : the phase delays are perfectly reversed and the π -shifts help mimicking the phase relation between the modes of an hypothetical time-reversed beam splitter [87].

In conclusion, we have described a structure capable of inverting the direct unitary introduced in section 4.2. Among the infinite operations that are available, the prescription 54 allows to find the one that reverses the forward evolution.

The results on the set of implemented transformations of section 4.2.2 can be extended directly to this new layout, by virtue of the strong symmetry connecting the two interferometers.

ON-CHIP DIRECT AND INVERSE INTERFEROMETERS

This chapter describes the various steps of fabrication and validation of the interferometric devices presented conceptually in chapter 4.

Section 5.1 reports on the optimization of the waveguide inscription parameters and the development and fabrication of the integrated-optics reconfigurable circuits. Section 5.2 describes the validation and characterization of the fabricated reconfigurable interferometers with classical light.

5.1 MICROMACHINING PROCESS AND DEVICES DESIGN

5.1.1 *Waveguide inscription parameters*

As discussed in section 2.3, there are numerous parameters in femtosecond laser waveguide inscription to set and optimize for each different substrate and application.

A first requirement, that we had already the chance to mention, is that the waveguides should support a single mode at the wavelength of this experiment. Furthermore, of particular importance for all integrated quantum photonic experiments are low losses figures and good matching of the mode supported by the waveguides with the spatial profile of the mode carried by the input optical fibers. Optical losses, in fact, affect the measurement time, especially when counting multi-photon coincidence events.

To address these first requirements, several different straight waveguides were fabricated with different process parameters and characterized with coherent light (see section 3.3). Since the final devices are meant to be injected with single or few-photons states from a Spontaneous Parametric Down-Conversion (SPDC) source emitting at 785 nm, a laser diode with peak spectral density at 784 nm was employed.

Being the parameter space is very broad, we focused on the two process variables that are easiest to control and fine-tune: the translation speed and the energy per pulse. For the other inscription specifications we referred to the indications in the literature or to previous experience of the research group on the same substrate and working wavelength.

All the devices were fabricated in alumino-borosilicate glass (Corning Eagle XG) using the apparatus described in section 3.1. The pulse train was focused inside the glass samples by means of a microscope objective with 50x magnification and a 0.6 numerical aperture. The repetition rate of the pulsed output was set to 1 MHz, corresponding to an intermediate regime between the single-pulse modification and the thermal accumulation regimes (see section 2.3.3 for reference). This repetition rate window was observed to lead to very good confinement properties of waveguides inscribed in alumino-borosilicate glass [88][60]. The transverse writing configuration was employed, with no beam shaping or multi-scan techniques: the waveguides were fabricated with a single pass of the focused femtosecond beam inside the substrate. The processing times were consequently quite rapid: only few seconds were needed for the inscription of a single waveguide.

A 30 μm inscription depth was chosen, as a trade-off between two opposing trends:

- The sensitivity of the fabricated photonic structures to surface defects, material stress and roughness is higher the shallower the writing depth. These give rise to increased propagation losses. It is also important to consider that a gold layer has to be deposited on the top sample surface, in order to pattern resistive heaters behaving as phase shifters. This implies that if the waveguides are too shallow, the evanescent field can penetrate substantially in the gold layer above, inducing further losses due to absorption or excitation of undesired phenomena (e.g. surface plasmon polaritons).
- The deeper the interferometric devices are fabricated, the higher must be the electrical power dissipated in the resistive heaters to modulate the refractive index, for a given spatial separation between the waveguides. Since the admissible heating is bounded by the limitations of the device, deeper structures could result in limited phase control possibilities.

Actually, this depth value was employed also in previous works [11] and resulted in an adequate thermal sensitivity while corresponding to inscription deep enough in the sample volume not to significantly incur in additional losses.

An analysis of the various loss contributions of straight waveguides machined with different parameters, was performed. The pulse energy was varied in the interval $170 \div 270$ nJ with 10 nJ energy increments; the writing speed was scanned between 20, 30 and 40 mm/s. The optimal fabrication parameters were found evaluating both the propagation losses of the resulting waveguide and the close matching of its mode dimensions with the mode carried by standard optical fibers at the wavelength of 785 nm, while making sure that only the fundamental transverse mode was supported.

These optimal parameters, employed for the fabrication of all the structures that will be described from now on, are reported in table 4. Correspondingly, we measured propagation losses $PL = 0.96$ dB/cm, coupling losses $CL = 0.36$ dB and $1/e^2$ mode dimensions 7.5×8.3 μm (for light polarized along the horizontal axis, parallel to the optical table). For a definition of these quantities see section 3.3.

5.1.2 Directional coupler design

After establishing the fabrication parameters, the evanescent coupling of the inscribed waveguides was studied, aiming to define a balanced directional coupler structure to employ in both the interferometers. The relevant geometrical parameters of the directional coupler are summarized in the scheme of figure 26, reporting the waveguide arrangement with a very dilated scale in the transverse direction, for clarity.

Fabrication parameters	
Substrate	Eagle XG
Laser system	Yb:KYW cavity dumped
Wavelength	1030 nm
Repetition rate	1 MHz
Pulse energy	250 nJ
Translation speed	30 mm/s
Microscope objective	50x, 0.6 NA

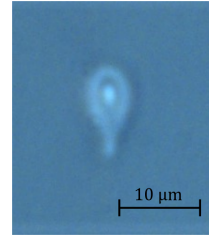


Table 4: FLM parameters optimized for waveguides guiding a single mode at 785 nm. An optical microscope image of the waveguide cross-section is included.

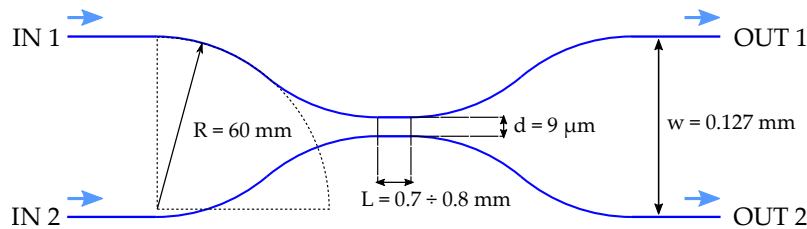


Figure 26: Schematic layout of the directional coupler design. R is the radius of curvature of the bent waveguide sections, w is the distance between input (output) ports, d and L are the interaction distance and length of the region where evanescent coupling takes place. The geometrical values chosen after the preliminary studies are also reported.

Aiming at the determination of the optimum value for the bending radius, a first experimental run of calibration devices involved straight segments joined by curved sections, employed for the measurement of bending losses (see section 3.3.3). The profile of the bends followed two symmetrical circular arcs, with a variable radius of curvature, connected to follow a 'S' shaped profile (see panel a of figure 27). The total length of the waveguides was kept fixed, while the radius of the bends was changed from device to device. A straight waveguide was also fabricated in the same sample, in order to drop the propagation and coupling loss contributions from the measured losses, using the formula 37. The measured bending losses as a function of the curvature radius are reported in figure 27. A value $R = 60$ mm was selected for curved sections, because it gives an acceptable value $BL = 0.32$ dB/cm (smaller than $PL = 0.96$ dB/cm). Larger radii of curvature in interconnection sections result in devices with a bigger longitudinal footprint and increased total propagation losses.

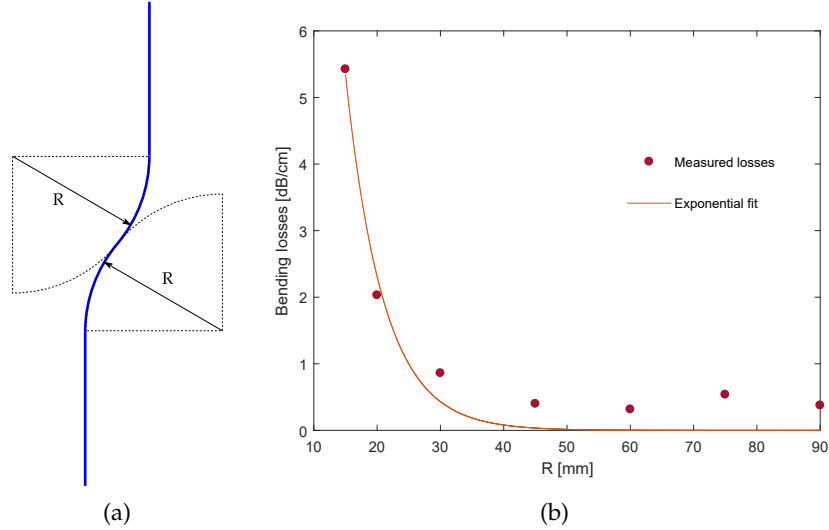


Figure 27: **(a)** Waveguide design for the estimation of BL. The middle bent section has a radius of curvature R ; waveguides with different values of R all had the same length (2 cm) of the bent section. **(b)** Measured BL as a function of the radius of curvature R of the bend. An exponential model was fitted to the data: BL descended below the level of the propagation losses per unit length for $R > 30$ mm.

Thereafter, the geometrical parameters of the interaction region were studied, i.e. the interaction distance d and length L . As explained in appendix B, the coupling coefficient κ is proportional to the overlap integral between the mode profiles centered on the two interacting waveguides. It is intuitive that κ should then depend very sensitively on d . In fact, often an exponential model of the form

$$\kappa \propto e^{-\frac{d}{d_0}} \quad (61)$$

is suitable [89]. d_0 is a parameter defining a characteristic scale for evanescent coupling decay. d_0 and κ depend also on the polarization. Here we report only data for light polarized linearly in the horizontal direction (in the laboratory frame of reference): this polarization state will be chosen, in fact, for the operation of the final devices.

κ defines (along with the detuning $\Delta\beta$) the spatial modulation frequency of power transfer in the interaction region. The effective reflectance and transmittance of the whole directional coupler are thus determined by the interaction length L . In the case of identical propagation constants in the two waveguides ($\Delta\beta = 0$), the reflectance and transmittance are given by (see equation 103):

$$R = \cos^2(\kappa L + \Phi), \quad T = \sin^2(\kappa L + \Phi) \quad (62)$$

Here, Φ defines the power exchange in the limit $L \rightarrow 0$ and is due to evanescent coupling in the curved sections preceding and following the interaction region.

A trade-off governed the choice of the distance d :

- The shorter the interaction distance, the shorter will be $L_{1/2}$, i. e. the interaction length required to have a balanced power splitting at the output ports, $R = T = 50\%$ (for most applications, $L_{1/2}$ will be chosen as the lowest value among the infinite values satisfying $R = T = 50\%$, all differing of π/κ). As a consequence, more compact couplers can be written.
- If d is too small, the process of writing the second waveguide could influence or damage the first, introducing a detuning $\Delta\beta$ or leading to an imbalance in the propagation losses. This could result in a different splitting ratio depending on the excited input port.

We studied the behaviour of various directional couplers, fabricated with the optimized parameters found in section 5.1.1. In particular, we tested an interaction distance $d = 9 \div 12 \mu\text{m}$, with an incremental step of $1 \mu\text{m}$, and we scanned $L = 0 \div 3 \text{ mm}$ with a step of 0.3 mm .

The splitting ratio measurements on these devices are reported in figure 28. The decay of the coupling coefficient with increasing d , predicted by equation 61, was confirmed. In fact, the characteristic length scale of power transfer can be observed to increase rapidly as d grows. The detuning was deemed negligible, even in the case $d = 9 \mu\text{m}$, since a minimum reflectance $R = 5.0\%$ was observed (severe detuning implies that the reflectance is limited from the bottom, see figure 43). The splitting ratio asymmetry with respect to the input port was also measured to be very low. Hence, the lowest interaction distance $d = 9 \mu\text{m}$ was selected for the complete devices, allowing for a short interaction length of balanced operation, $L = L_{1/2} = 0.7 \div 0.8 \text{ mm}$.

Actually, κ is, very sensitive on writing power fluctuations [90], and fabrication tolerances imply that optical properties cannot be perfectly reproduced with the same geometrical parameters between different fabrication runs. This issue was surmounted by keeping d and R fixed for the subsequent fabrications and writing several copies of the integrated optical circuits with a set of different values of L . This was sufficient to compensate for the drifts and noise affecting the fabrication setup, and, in our case, to obtain balanced directional couplers in different sessions.

5.1.3 Integrated optical layout

The schematic networks in figures 20, 24 were easily converted to the photonic circuit designs depicted in figure 29. The translation is immediate when substituting beam splitters for their integrated counterpart, the directional coupler. The separation between the waveguides

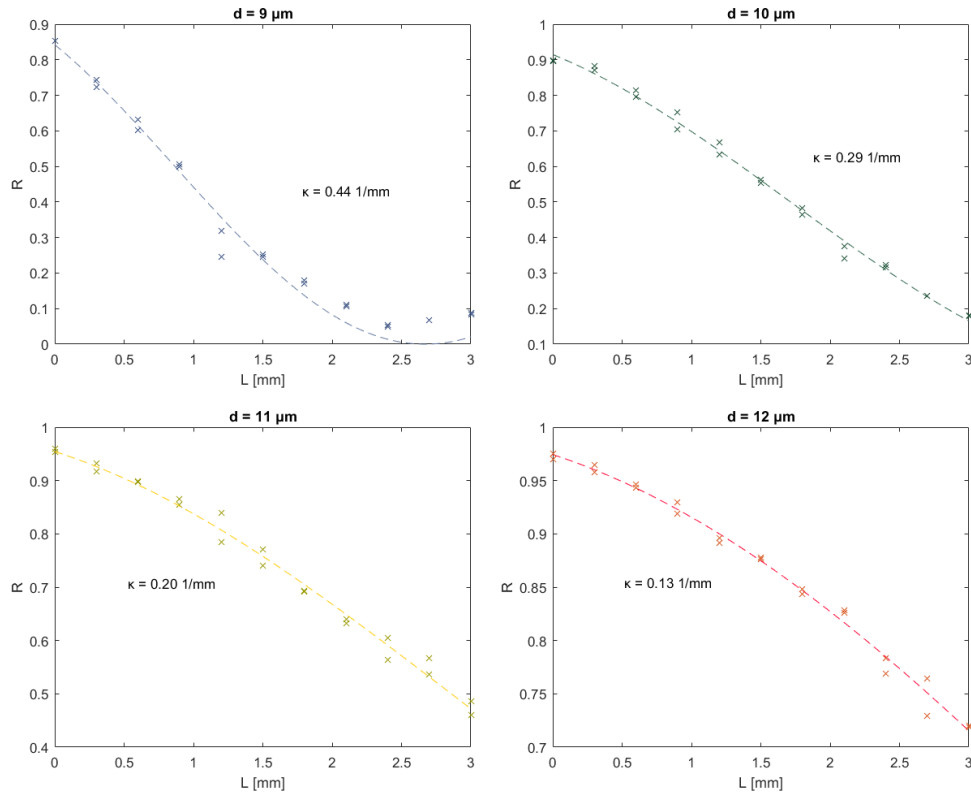
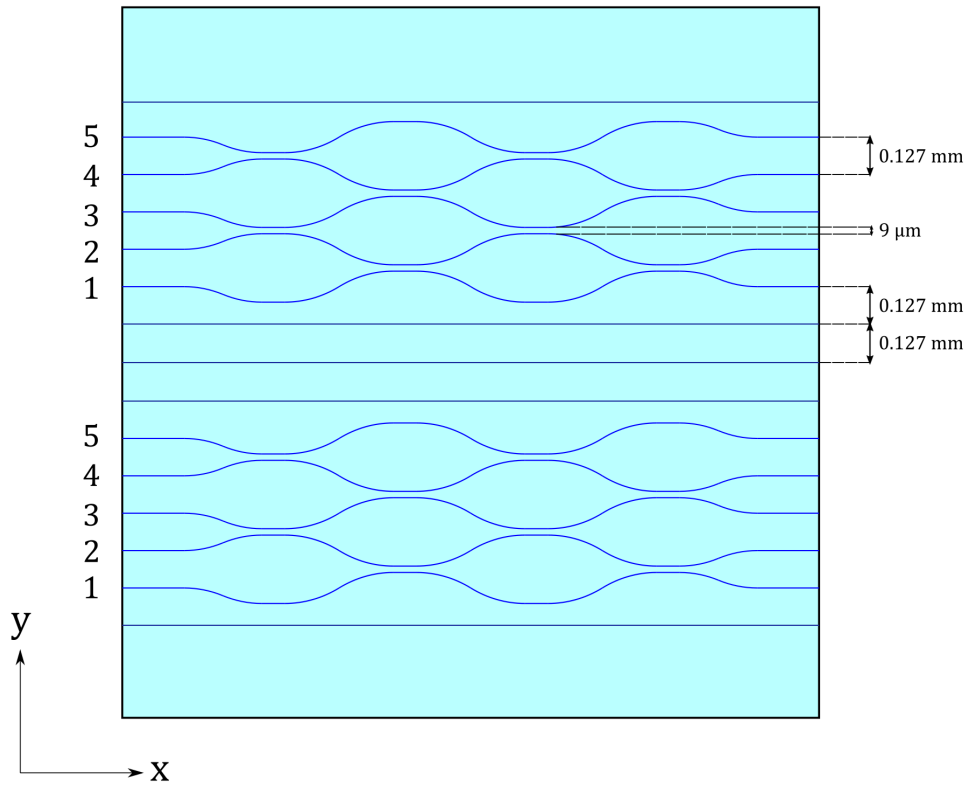


Figure 28: Reflectance (power fraction in the *bar* port) measured for sets of directional couplers having different interaction region distances d and lengths L . Two points are provided for each L value, corresponding to the splitting ratios measured by coupling light from the two distinct input ports of the same device. The difference between these measurements shows whether the coupler is symmetric or not. The curves were fitted with a sinusoidal model, in order to extract the coupling coefficient κ . A fast decay of κ with growing d is clear. No significant detuning was inferred.

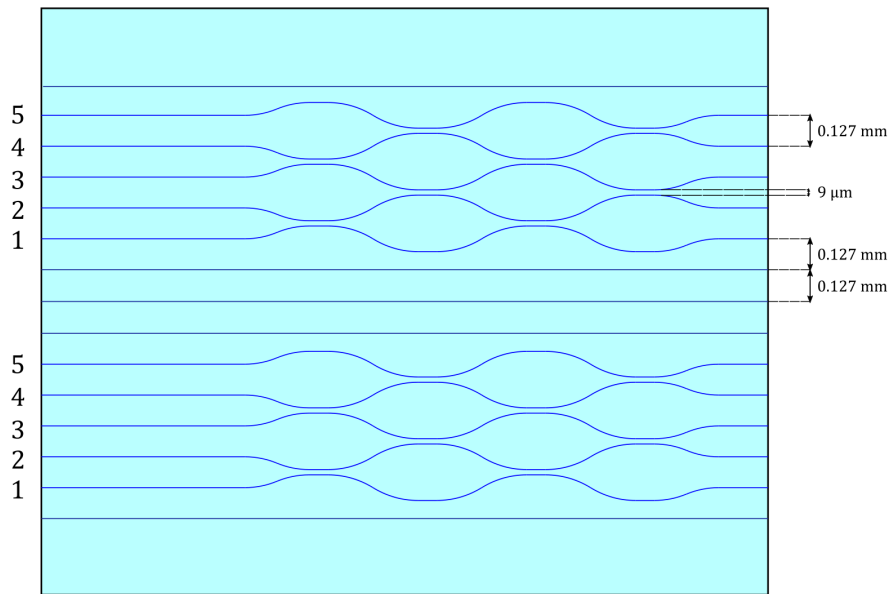
in their initial and final straight segments (also called *pitch*, w) was fixed to 0.127 mm. This corresponds to the pitch of the fiber arrays that will be used in the experiments to route and inject single photons inside the chips.

In the circuit design, particular care was given to keeping the optical paths of the different waveguides as balanced as possible. In fact, the single-photon states employed for the experiments are described by wavepackets, with a nonzero bandwidth and a limited duration. This implies that, were the optical paths unbalanced, photons at the output ports would show an increased *distinguishability*, or that quantum interference effects could be weakened.

The resulting longitudinal footprint of the device was about 26 mm, neglecting the straight segments at the beginning and end, which extend to the input and output facets.



(a)



(b)

Figure 29: Geometrical arrangement of the waveguides in the **a.** direct and **b.** inverse interferometers. The scale of the y axis was dilated for clarity of illustration. The guided modes are numbered from 1 to 5 on the input facet side. All the coupling regions maintain the same parameters of figure 26. The two interferometers are related by a reflection about the y axis.

From figure 29b, it can be observed that in the second interferometer, the initial straight segments are much longer (1.3 cm) than the ones written in the first chip. Further thermo-optic phase shifters will be placed upon these segments to adjust the phase differences required to simplify the structure to an identity transformation, when the two devices are cascaded, as mentioned in section 4.3.2.

As portrayed in figure 29, multiple devices were fabricated in a single chip, presenting the same layout and geometrical specifications, except for the length L of each interaction region. The latter was varied linearly between the different devices in order to compensate for fabrication tolerances, as mentioned in section 5.1.2. Each interferometer was enclosed between two straight waveguides, lying at the same distance $w = 127 \mu\text{m}$ as the structure pitch. These waveguides were inscribed to facilitate and monitor the alignment between the first and second chips, when they are operated in cascade. In fact, the straight guides can be addressed with the same fiber array used to inject photons inside the interferometers, and the total transmitted power can be measured while fine-tuning the relative displacement between the waveguides output and input facets at the interface between the two chips. By optimizing the transmission on both the straight waveguides at the same time, a good alignment of the inner interferometers is even more so guaranteed.

5.1.4 Resistive heaters electrical design

The design of the resistors functioning as thermo-optical phase shifters was carried out alongside with the planning of the integrated optical layout, before the actual machining of the devices. A general concept of the arrangement and dimensions of the resistors that would have been patterned on top of the optical circuits was in fact to be devised before their inscription.

The gold resistors are characterized by a thickness t , a width b and a length l , respectively across and along the direction of current flow. The thickness of the gold film deposited on the sample surface is determined by the duration of the sputter coating process. The width and length are instead patterning parameters, set by the ablation path of the femtosecond laser beam.

The total resistance \mathcal{R} is estimated with the formula $\mathcal{R} = \rho \frac{l}{bt}$, where ρ is the resistivity of gold. With respect to the resistivity reported in the tables of material properties ($\rho_{\text{Au}} = 2.4 \cdot 10^{-8} \Omega \cdot \text{m}$ at 20°C), the one measured on our resistive heaters is a factor ≈ 3 bigger. This could be due to the fact that the sputtered gold layer is polycrystalline and to the presence of additional dislocations, impurities or surface defects with respect to three-dimensional, bulk samples.

The choice of l and w is tied to damage threshold considerations. In fact, even if the length is not related to the provided phase shift [11],

the dimensions of the resistor determine the temperature increase in the gold film and in the glass substrate. In particular, for a given electrical power dissipated in the resistor, the heat generated per unit volume is bigger the shorter and thinner is the resistor. Since high temperatures might damage the devices, the resistor dimensions have to be selected accordingly.

For the resistors governing the unitary transformations implemented by the interferometers we choose $t = 65$ nm, $b = 0.13$ mm and $l = 5.32$ mm. This last value was fixed by the decision of patterning the resistors directly over the curved sections connecting two interaction regions. The resistors providing the intermediate phase shift, fabricated on the initial part of the second device, were thinner ($b = 0.1$ mm) and longer ($l = 8 \div 10$ mm). We opted for a more elongated shape in order to distribute the heat on a larger area: due to the more involved cross-talks in this phase shifter set, it is likely that the driving voltages and powers will be higher. However, the width of the resistors could not be increased since their separation was fixed to $w = 0.127$ mm.

These dimensions, along with the empirical factor ≈ 3 , correspond to the following nominal resistance values: $\mathcal{R} = 50$ Ω for the internal and $\mathcal{R} = 100$ Ω for the interconnection resistors. These figures were selected because they correspond to the resistance of common loads in electronics, therefore most power supplies should be able to interface and drive them effectively.

In figure 30 we report the experimental current-voltage characteristic curve, measured on a resistor fabricated on a separate sample in order to conduct electrical tests. The dimensions coincide with those of the short resistors on the first chip ($\mathcal{R} \approx 50$ Ω). The behaviour of the passive device is well approximated by a linear $I - V$ relation for low voltages, but it starts to deviate from linearity when the voltage (or the dissipated power, or the peak temperature induced) is increased too much. We identified a threshold for non-ohmic behaviour at a Joule power of approximately $\mathcal{P}_{\max} = VI = 0.7 \div 0.8$ W. Another limitation to the resistive heaters operation arises from permanent damage caused by high temperatures. In our $I - V$ diagrams, we identified such an occurrence with the deviation of the falling voltage curve from the rising voltage one (respectively, the red and blue series in figure 30). On the same resistor, we assessed that, when the Joule power was kept below \mathcal{P}_{\max} , the electrical response did not change, operating the resistors several times with different voltages. Still, when exceeding \mathcal{P}_{\max} significantly, damage to the protective resin layer started to be visible, and the behaviour of the resistor with decreasing voltage departed from the rising branch. In general, the permanent resistor alteration was associated with a decreased resistance and more pronounced nonlinear features in the $I - V$ characteristic curve.

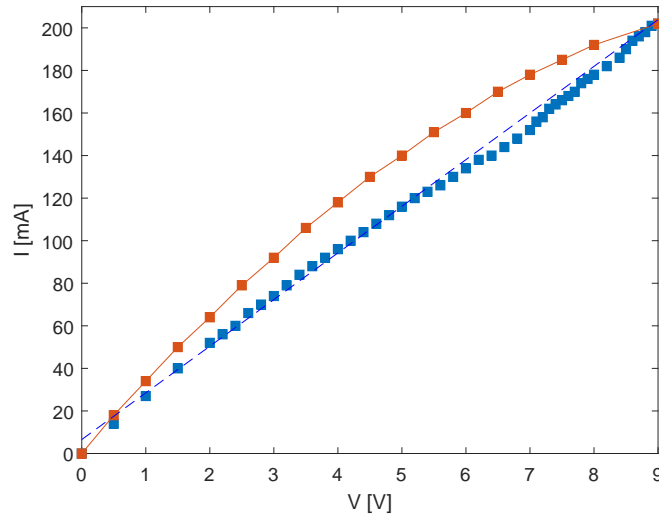


Figure 30: Current-voltage characteristic curve of a gold resistive heater with $\mathcal{R} = 43 \Omega$ (measured with a digital multimeter). The voltage imposed on the resistor is first increased (blue squares), then decreased (red squares), showing that the behaviour of the resistor has changed permanently by exceeding a certain damage threshold. The current response of the resistor before structural damage is well approximated with a linear (ohmic) model: such a linear fit is shown as the dashed blue line. The decreasing voltage curve is markedly nonlinear. A permanent 25% decrease of \mathcal{R} was observed during the measurement cycle.

Consequently, the threshold \mathcal{P}_{\max} was adopted for the operation of the resistive heaters as phase shifters ¹.

5.1.5 Heaters arrangement and interconnection

When an electric current is forced in the resistors, electrical power is dissipated in the form of heat, by Joule effect. Being the thermal conductivity of glass much higher than that of air at standard conditions, most of the heat is dissipated in the sample volume, creating a temperature gradient decreasing radially from the axis of the heater. The refractive index of the glass is linearly dependent on temperature variations (at least in a limited dynamic range), therefore, power dissipation allows to induce a linear phase difference on the light propagating into waveguides at different distances from the heater. Mathematically:

$$\varphi = \alpha \cdot \mathcal{P} + \varphi_0, \quad (63)$$

¹ Assuming that the temperature contributions from nearby heaters that are operated at the same time is negligible in the region beneath the one we are considering.

where φ is the total phase delay between two waveguides, \mathcal{P} is the heat dissipated in the resistor, α is a coefficient describing the linear relation between the two and φ_0 is an intrinsic phase difference to which the fields are subjected even in the absence of active control.

α depends primarily on geometric parameters, i. e. from the position of the waveguides relative to the resistor. Considering a wire-like heater with negligible width and disregarding the heat flowing into the air, an analytic expression for α is derived [11], given the distances ρ_1, ρ_2 of the interferometer arms from the resistor:

$$\alpha = \frac{2n_T}{\lambda k} \frac{L_{\text{arm}}}{L_{\text{wire}}} \ln \left(\frac{\rho_1}{\rho_2} \right), \quad (64)$$

where $\varphi = \varphi_2 - \varphi_1$, $n_T \approx 1 \cdot 10^{-5}$ is the thermo-optic coefficient of glass, $\lambda = 785 \text{ nm}$ is the wavelength, $k = 0.9 \text{ W}/(\text{m} \cdot \text{K})$ is the glass thermal conductivity, L_{arm} is the interferometric arms length and L_{wire} is the resistor length. This model assumes additionally that the heater and the waveguide are all straight and parallel.

A phase difference is established between each couple of waveguides travelling parallel to the resistor, as predicted by equation 64. Our interferometers include five waveguides and the heaters must be fabricated in couples on two different transverse sections, in order to control independently the four phase terms of figures 20, 24. Therefore, each heater does not only influence directly the phase shift within the nearest waveguide couple, but also between further waveguides lying beyond, through *cross-talk* terms. By collecting all the α 's in a matrix (denoted for simplicity with the same symbol), it is possible to relate the powers dissipated in each heater with the phase shifts in a linear system:

$$\vec{\varphi} = \alpha \cdot \vec{\mathcal{P}} + \vec{\varphi}_0, \quad (65)$$

where $\vec{\mathcal{P}}$ is the ordered collection of Joule powers, $\vec{\varphi}$ is the set of controlled phase shifts and $\vec{\varphi}_0$ is the set of intrinsic phases, in absence of active control.

Were the waveguides very distant and the heaters placed directly over them, α would be almost diagonal and its eigenvalues higher the larger the waveguide separation. However, this separation is constrained below a few hundreds of μm by the design of the interferometer. Therefore, we decided to optimize the control of the reconfigurable phases instead of seeking to suppress the out-of-diagonal α elements. More precisely, when deciding the arrangement of the heaters, we sought to minimize the Joule power needed to provide a certain set of phase shifts. Since this choice does not result in negligible cross-talk terms, a careful calibration of the action of the resistive heaters will be needed in order to operate them effectively.

It is necessary to study only the effect of two resistors on four waveguides. In fact, the four controlled phase shifts are divided in two couples, in the initial and final tracts of the interferometer, in which the

arrangement of the waveguides is perfectly mirrored. The two tracts are sufficiently distant (≈ 7 mm) to safely assume that no cross-talk term will relate their phases and resistors. The fifth waveguide carries an input/output phase term, so that it can be neglected for the analysis.

This study was performed by optimizing two figures of merit with respect to the positions of the two resistors on top of the glass sample:

- maximization of the determinant of the matrix α . A basic result in linear algebra states that if A is the matrix representing a linear map $f : \mathbb{R}^n \rightarrow \mathbb{R}^n$ and S is a subset of \mathbb{R}^n , the volumes of S and its image under f are related by:

$$\text{Volume}(f(S)) = |\det(A)| \cdot \text{Volume}(S) \quad (66)$$

Therefore, $|\det(\alpha)|$ indicates the extent of $\vec{\varphi}$ space that can be spanned with a given set of Joule powers $\vec{\mathcal{P}}$.

- maximization of the minimum singular value of α .² This quantity is related to the *operator norm* of the transformation represented by A .

The operator norm, denoted with $\|A\|_2$, is the minimum real value c satisfying the inequality

$$\|A\vec{v}\| \leq c\|\vec{v}\| \quad (67)$$

for all $\vec{v} \in \mathbb{R}^n$. If $\|\cdot\|$ represents the Euclidean norm of a vector, the operator norm of A is its largest singular value.

In our case, we are interested in the operator norm of α^{-1} : we seek to enforce the inequality

$$\|\vec{\mathcal{P}}\| \leq \|\alpha^{-1}\|_2 \cdot \|\vec{\varphi}\| \quad (68)$$

with the lowest possible constraint, in order to minimize the control effort required for a given set of internal phases. Since the singular values of α^{-1} are the inverse of those of α , minimizing $\|\alpha^{-1}\|_2$ is completely equivalent to maximizing the lowest singular value of α .

An initial analysis was performed by considering the phase shift affecting straight waveguides heated by straight heaters with the same length. This situation is depicted on the left side of figure 31. A separation equal to the interferometer pitch, $w = 0.127$ mm, was assumed. Equation 64 was employed to estimate all the elements of α . The resistors were approximated with infinitesimally thin wires, and their y position was varied to determine the optimal conditions.

² The singular values of a complex $m \times n$ matrix A are real, non-negative numbers that, when collected in a diagonal matrix Σ , allow for the decomposition $A = U\Sigma V$. U and V are both unitary matrices. This decomposition exists for any A . The singular values coincide also with the square roots of the eigenvalues of the $m \times m$, symmetric, positive-semidefinite matrix $A^T A$.

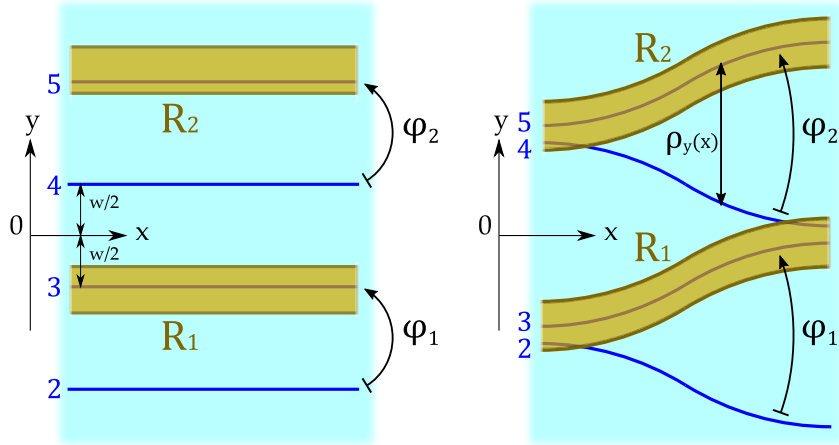


Figure 31: Two different geometrical configurations for exciting phase delays inside the interferometer. Left: Straight resistors patterned over a dedicated section where the waveguides are straight and parallel. Right: Bent resistors following the outline of the waveguide bends underneath, patterned exactly above the waveguide tract they must influence directly.

Figure 32 reports the results of the analysis on both figures of merit, $|\det(A)|$ and $\min(\sigma_1, \sigma_2)$. We observed that optimization using the two different parameters gives very similar results. In this case, the two methods agree in finding the maximum control efficiency for heaters placed directly above the waveguide whose phase delay they are supposed to drive directly. Specifically, the optimum is reached when the resistors lie on top of waveguides 2 and 4, or 3 and 5, with the convention of figure 31.

The numerical study actually outputs a set of small y offsets with respect to the waveguide positions, amounting to few tens of micrometers. Since these values are much smaller than the actual resistor width $b = 0.13$ mm, they can be neglected. The calculation yielded such an optimum α :

$$\alpha_{\text{str}} = \begin{pmatrix} 38.1 & 10.0 \\ -17.9 & 38.1 \end{pmatrix} \frac{\text{rad}}{\text{W}} \quad (69)$$

This first arrangement would require two dedicated regions where the waveguides are straight, parallel and appropriately distanced. Another possibility is to pattern the heaters directly over the bent interconnections, like in the right panel of figure 31. Knowing, from the straight heaters numerical analysis, that the optimum control is obtained when the resistors lie on top of waveguides 3 and 5, we restricted ourselves to this situation and compared it to the previous scenario.

The α theoretical estimation was performed integrating numerically equation 64 along the x coordinate (ρ is in this case dependent

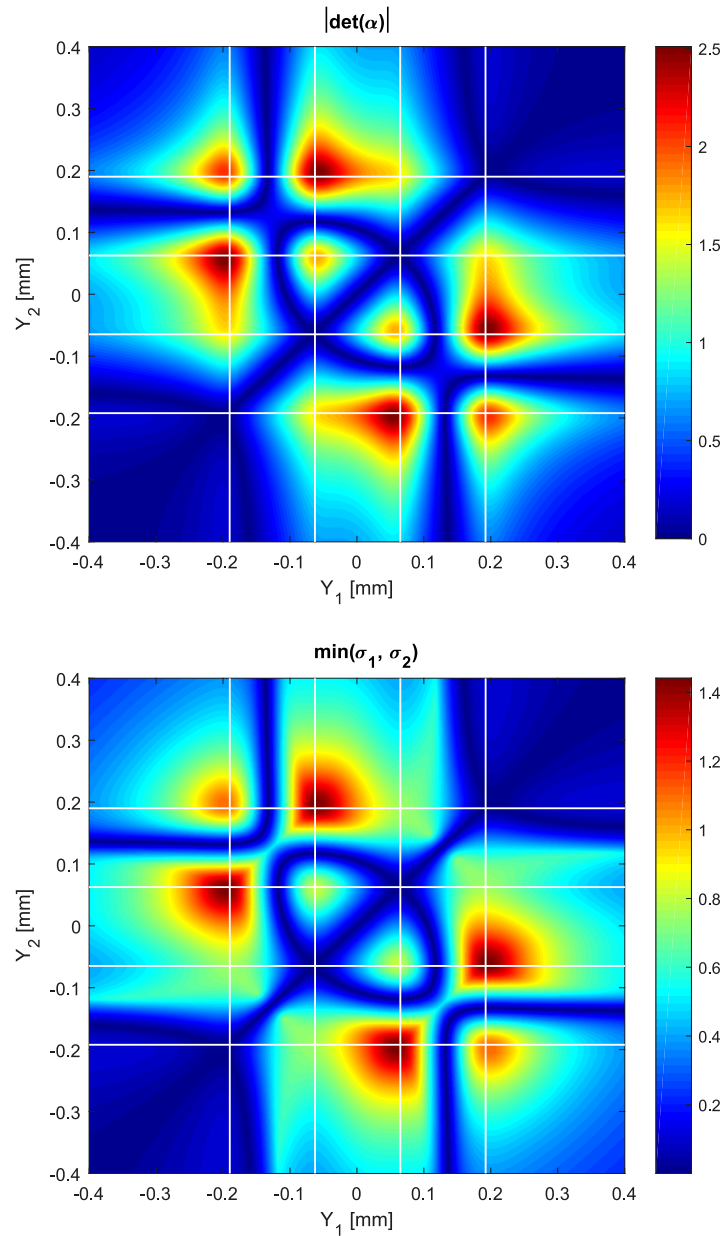


Figure 32: Numerical studies of the effectiveness of different heater arrangements over straight waveguides. Above: $|\det(\alpha)|$ map as a function of the positions of the two heaters. Below: $\min(\sigma_1, \sigma_2)$ map as a function of the positions of the two heaters. The frame of reference is the same that was depicted in figure 31. White lines denote the fixed positions of the straight waveguides. Both maps are symmetric with respect to the exchange of the positions Y_1 and Y_2 of the heaters. Their qualitative features are very similar; both the figures of merit are maximized by placing the heaters almost directly above the waveguides 2 and 4, or 3 and 5 (with the convention of figure 31). Secondary maxima are reached when the heaters lie above other couples of distinct waveguides. The diagonal line where both matrix quantities are null represents exactly overlapping resistors.

on x). The curves described by both the resistors and the waveguides have the same radius $R = 60$ mm optimized from the bending losses characterization. The numerical calculation yielded:

$$\alpha_{\text{bent}} = \begin{pmatrix} 31.9 & 9.6 \\ -22.7 & 31.9 \end{pmatrix} \frac{\text{rad}}{W} \quad (70)$$

α_{bent} presents indeed slightly lower diagonal terms and higher or comparable off-diagonal terms with respect to α_{str} , but the difference is not dramatic. In fact, the total electrical power that must be dissipated in order to provide a π phase shift to each of the four interferometric rings ³ is only 20% higher compared to the optimal case with straight resistors. Considering the fact that the design with curved resistors and no dedicated region in which the waveguides are straight and well separated allows to keep the longitudinal footprint and optical paths more compact (of ≈ 8 mm), this design appeared overall more attractive. In fact, the length of the device influences directly the magnitude of the losses inside the optical circuit, which are particularly critical for experiments with single or few photons. This heater and interferometer design was in fact adopted for the integrated circuits, as anticipated from the layout in figure 29.

Obviously, given the symmetry of the two devices, the results of the analysis above can be simply extended to both interferometers, performing the direct and inverse transformations. In this second case, we opted for patterning the resistors on the complementary couple of waveguides with respect to the choice made on the first interferometer (e. g. 2 and 4 instead of 3 and 5 for controlling φ_7 and φ_8). This results in changing the sign to all α elements: $\alpha' = -\alpha$. This expedient was employed in order to satisfy the inversion conditions of equation 54 with a milder temperature increase.

The central phase shifts, needed to simplify the interferometric structure when the two devices are operated in series, are provided by resistive heaters patterned on the initial segment of the inverse interferometer (hence the longer straight segments at the left edge of figure 29b.). The desired phase delays distribution consists of an alternation of 0 and π terms; therefore, if the 5th mode is chosen as a reference, four phases will have to be manipulated via four active thermal elements.

To decide the positions of the heaters, we performed the procedure described above on the geometry of this different system, portrayed in figure 33. This task is more involved, requiring the construction and manipulation of many 4×4 α matrices, but it is still computationally feasible.

For this larger system, whose control laws are complicated by the presence of many cross-talk terms, we decided to employ a more

³ Calculated as $\mathcal{P}_\pi = 2\pi \cdot \sum_{i,j=1}^2 \alpha_{ij}^{-1}$.

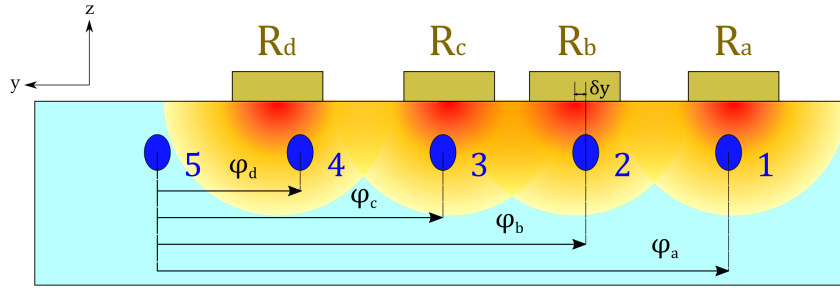


Figure 33: Cross-sectional view of the arrangement of the heaters on top of the initial straight waveguide segments in the second device. The sample is viewed from the input facet. Here and in all the subsequent calculations and measurements, the phase of the 5th mode is taken as a reference, and all other phases are directly influenced via the resistive heaters.

refined model to describe the thermo-optical coefficient α , in order to provide more accurate matrix estimations and fine-tune the optimization process. We decomposed the thick resistor in an array of infinitesimally thin heated wires, integrating the contributions of each (described by equation 64) to the temperature and phase delay profile. This method allowed us to take into account the finite width of the heaters ($b = 0.1$ mm); nonetheless, we still neglected border effects in the x direction and the power dissipated in the electric contacts.

Performing the aforementioned integration, the following functional form for α was derived:

$$\alpha = \frac{n_T}{\lambda k} \left[\frac{y_2}{b} \cdot \ln \left(\frac{y_2^2 + z^2}{(y_2 - b)^2 + z^2} \right) + \frac{y_1}{b} \cdot \ln \left(\frac{(y_1 - b)^2 + z^2}{y_1^2 + z^2} \right) + \ln \left(\frac{(y_2 - b)^2 + z^2}{(y_1 - b)^2 + z^2} \right) + \frac{2z}{b} \cdot \left(\text{atan} \left(\frac{y_1 - b}{z} \right) + \text{atan} \left(\frac{y_2}{z} \right) - \text{atan} \left(\frac{y_1}{z} \right) - \text{atan} \left(\frac{y_2 - b}{z} \right) \right) \right] \cdot \frac{L_{\text{arm}}}{L_{\text{wire}}}, \quad (71)$$

where b is the thickness of the resistor, z is the waveguides depth and y_1, y_2 are the transverse coordinates of the waveguides.

With this refined analytic formula for α , we proceeded to construct the α matrices of the system represented in figure 33, searching the highest $|\det(\alpha)|$ by moving the heaters on the top surface, along the y axis. Once again, the optimal positions were found in the vicinity of the waveguides, with micrometric offsets (reported with respect to the central axis of the resistor):

$$\begin{cases} \delta y_a &= -16 \mu\text{m} \\ \delta y_b &= -2 \mu\text{m} \\ \delta y_c &= -2 \mu\text{m} \\ \delta y_d &= -6 \mu\text{m} \end{cases} \quad (72)$$

For these resistors, however, we chose to adopt these optimal offsets in the final electrical network pattern, since the finite width was taken into account in the analysis.

The numerical maximization procedure produced the following optimal α matrix:

$$\alpha = \begin{pmatrix} 72.0 & 31.7 & 0.53 & -29.4 \\ 36.7 & 64.2 & 20.3 & -17.7 \\ 18.8 & 30.7 & 52.8 & 2.4 \\ 7.9 & 11.4 & 19.3 & 34.1 \end{pmatrix} \frac{\text{rad}}{W}, \quad (73)$$

by using the same constant values reported under equation 64. Once again we point out the fact that the matrix is far from being diagonal, even though the largest elements lie indeed on the diagonal. This implies that each resistor influences mainly the interferometric arm directly beneath.

Once the positions of the heaters were found, the remaining design task was to use the parts of the gold layer that were left over to complete the electrical network with pad sections, used for establishing electrical contact with the pin headers connectors (described in section 3.2.2) and ultimately supplying the resistors with external sources.

Two main constraints influenced this task. The electrodes had to be aligned with a 2.54 mm pitch at the edges of the samples, in order to match the spacing between the pins of the commercial connectors. In addition, the gold pads had to be characterized by a much lower resistance than the heaters they were connected to, so that most of the electrical power was dissipated in the latter elements. This requirement was met by making sure that the width of the electric pads was considerably larger than the one of the resistors. Figure 34 illustrates, by way of example, the electrical network fabricated over the direct interferometer. The design of the electric elements and interconnections on the other device was indeed similar.

We report in tables 5, 6 the measured values of the heater resistances on the complete chips. The resistances are comprehensive of the (much lower) contribution of the electric pads. The characterized values are quite close to the design figures, i. e. 50 Ω for the bent resistors and 100 Ω for the long interconnection resistors. All these resistance values permit to dissipate up to \mathcal{P}_{max} with a driving voltage below 10 V, which is a reasonable value for most commercial DC power supplies. Two different devices, denoted by 8 and 9, were electrically connected on each sample. In the following section it will be shown how this couple of interferometers exhibit indeed the most faithful performances to the design specifications, among the multiple replicas fabricated in the sample.

The complete pinout scheme of the two final devices is also provided in figure 35.

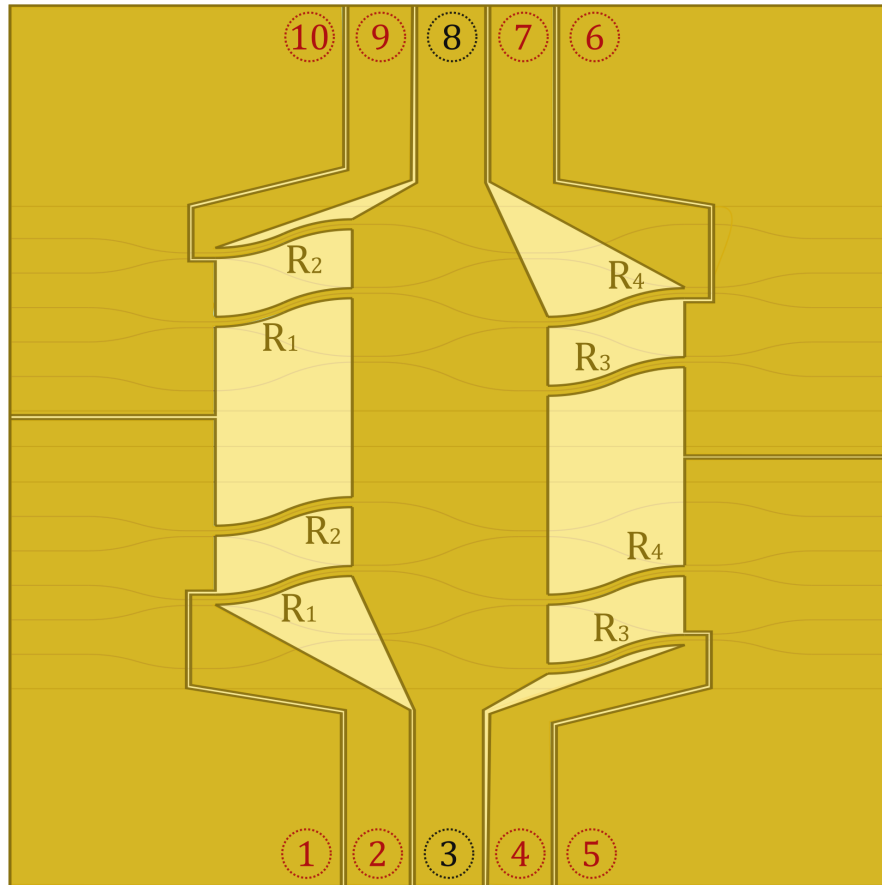


Figure 34: Pattern of laser ablation traces defining the resistors and the electric pads that are used to connect them with external supplies. The picture corresponds to the electrical network patterned on top of the first (direct) device, which is visible under the partially transparent gold layer. The lighter-shaded region corresponds to the electrically-isolated, floating region between the contacts. Two devices, differing only for the length L of the interaction regions, were electrically connected on the same sample. The electrode identified with black numbers is a cathode in common to resistors R_1, \dots, R_4 , while the other electrodes are controlled independently in DC. The drawing is not in scale.

1 st chip (Direct transformation)				
Device #	\mathcal{R}_1 [Ω]	\mathcal{R}_2 [Ω]	\mathcal{R}_3 [Ω]	\mathcal{R}_4 [Ω]
8	55	50	53	50
9	50	51	53	53

Table 5: Resistance values measured on the direct interferometer chip for two different photonic devices, 8 and 9. The naming conventions are the same of figure 34.

2 nd chip (Inverse transformation)				
Device #	\mathcal{R}_5 [Ω]	\mathcal{R}_6 [Ω]	\mathcal{R}_7 [Ω]	\mathcal{R}_8
8	50	50	55	51
9	47	46	48	52
Device #	\mathcal{R}_a [Ω]	\mathcal{R}_b [Ω]	\mathcal{R}_c [Ω]	\mathcal{R}_d
8	109	124	129	137
9	130	129	119	113

Table 6: Resistance values measured on the inverse interferometer chip for two different photonic devices, 8 and 9. $\mathcal{R}_1, \dots, \mathcal{R}_4$ denote the heaters that control the degrees of freedom of the reconfigurable transformation. $\mathcal{R}_a, \dots, \mathcal{R}_d$ denote the heaters employed for controlling the intermediate phases when the two chips are interfaced. Their resistance is much larger since their shape is narrower and longer.

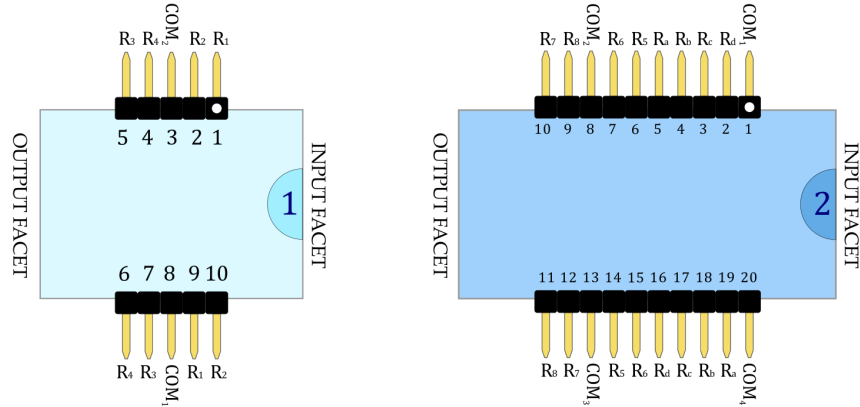


Figure 35: Pinout scheme for the two chips. The lower (upper)-side pins address the 8th (9th) device. The COM pins denote a cathode common to all the integrated resistors and are connected on-chip by a low-impedance path.

5.2 CHARACTERIZATION OF THE INTEGRATED DEVICES

Once the optical circuits were fabricated via FLM, characterization and calibration tests and measurements were devised and performed in order to assess the operation of the interferometers with respect to the expected behaviours.

All measurements reported here were performed with coherent light from a laser diode emitting at 784 nm; the power distribution obtained at the output of the interferometric devices coincides theoretically with the probability of detecting a single photon at the same output ports.

A first characterization of beam splitter reflectances and power distribution (section 5.2.1) was performed before the gold coating and resistor patterning process. The devices with the best performance were in fact identified at this stage, and the resistors were successively patterned on them.

5.2.1 Power distribution and beam splitter reflectances

A first, overall indication about the good performance of the interferometers is given by the measurement of the output distribution at the output ports. Light was coupled in each single input port, separately, and the power carried by each mode at the output of the photonic circuit was sequentially measured with a power meter. Background light (ambient light, laser light that did not couple in the input waveguide) was subtracted from the readings and the resulting distribution was normalized to the total output power. This power splitting distribution was then compared to the theoretical distribution (calculated assuming, as in chapter 4, balanced directional couplers and optical paths in the different interferometer arms) to identify the best devices and obtain a first indication of the suitable interaction length for 50% reflection, 50% transmission ⁴.

We report in tables 7, 8 the distributions of the devices that fitted the theoretical transformation the closest. Two separate measurements were carried out with orthogonal, linearly-polarized beams (H (V) stands for horizontal (vertical) polarization, in the laboratory frame of reference). The two distributions are quite different because of the waveguide birefringence, that splits the degeneracy between fundamental modes with different polarizations. This phenomenon results in different mode profiles and directional coupler splitting ratios (namely, $\kappa_H > \kappa_V$: $L_{1/2}$ is larger for V-polarized light). Since we are not concerned with photon polarization for these experiments, we chose to adopt the H polarization for subsequent characterizations and experiments. The proximity of the experimental to the theoretical

⁴ We recall that an interaction length scan was performed in order to compensate the FLM process drift and variability.

1 st chip (Direct transformation)									
Device	Pol.	L [mm]	In #	Out1	Out2	Out3	Out4	Out5	F
10	V	0.83	1	7.7%	68.6%	12.1 %	11.7%	0.0%	0.988
			2	19.3%	8.5%	7.4%	53.3%	11.4%	
			3	60.3%	11.8%	4.4%	10.8%	12.8%	
			4	6.1%	5.9%	7.2%	13.7%	67.1%	
			5	4.8%	5.0%	67.7%	13.8%	8.6%	
9	H	0.76	1	1.0%	68.5%	13.7 %	16.7%	0.0%	0.996
			2	14.0%	15.1%	2.2%	51.2%	17.5%	
			3	69.7%	3.6%	7.7%	5.1%	13.9%	
			4	8.3%	6.3%	2.5%	17.8%	65.1%	
			5	8.0%	7.7%	73.7%	7.6%	3.0%	
Theoretical distribution									
			1	2.1%	72.9%	12.5%	12.5%	0.0%	
			2	12.5%	12.5%	6.3%	56.3%	12.5%	
			3	72.9%	2.1%	6.3%	6.3%	12.5%	
			4	6.3%	6.3%	2.1%	12.5%	72.9%	
			5	6.3%	6.3%	72.9%	12.5%	2.1%	

Table 7: Power distribution out of the best devices in the first chip. L is the length of each interaction region, Pol. is the linear polarization state, In # is the input waveguide and F is the fidelity of the experimental to the theoretical probability distribution.

power distribution was estimated through the fidelity F (already introduced in section 4.2.3). For the case of the probability distributions at hand, the appropriate definition is:

$$F = \frac{1}{5} \sum_{i=1}^5 \sum_{j=1}^5 \sqrt{p_{j|i} q_{j|i}} \quad (74)$$

where p_j and q_j are the experimental and theoretical distributions, i runs between the different input modes and j between the output modes, that is, the stochastic process outcomes. F is averaged over the distributions collected for all input ports.

Once the more promising devices were found, we fabricated the resistors, as explained in the previous section. Subsequently, we performed a more detailed characterization, aiming to find the internal parameters of the interferometers. Namely, we devised a procedure to extract the internal beam splitter reflectances R_1, \dots, R_8 from splitting ratio measurements already performed at the device output. We use the same naming convention introduced in the schemes of figures 20, 24.

The main concern for this characterization step was avoiding to employ observable quantities affected by interference effects. In fact, to improve the estimation accuracy, we avoided any assumption about the intrinsic phase imbalances in the interferometric arms. This was

2nd chip (Inverse transformation)

Device	Pol.	L [mm]	In #	Out1	Out2	Out3	Out4	Out5	F
13	V	1.04	1	4.8%	7.5%	70.7 %	7.6%	9.4%	0.992
			2	65.5%	16.9%	4.9%	5.9%	6.8%	
			3	11.6%	2.8%	8.6%	0.5%	76.5%	
			4	16.9%	56.3%	2.4%	18.7%	5.7%	
			5	0.0%	17.3%	14.5%	66.8%	1.4%	
9	H	0.76	1	4.9%	9.0%	69.7%	7.4%	9.0%	0.996
			2	65.5%	15.8%	5.6%	6.0%	7.0%	
			3	13.4%	3.6%	8.1%	1.3%	73.6%	
			4	16.0%	54.9%	3.8%	15.2%	10.1%	
			5	0.0%	16.4%	13.6%	68.8%	1.3%	
Theoretical distribution									
			1	2.1%	12.5%	72.9%	6.3%	6.3%	
			2	72.9%	12.5%	2.1%	6.3%	6.3%	
			3	12.5%	6.3%	6.3%	2.1%	72.9%	
			4	12.5%	56.3%	6.3%	12.5%	12.5%	
			5	0.0%	12.5%	12.5%	72.9%	2.1%	

Table 8: Power distribution out of the best devices in the second chip. L is the length of each interaction region, Pol. is the linear polarization state, In # is the input waveguide and F is the fidelity of the experimental to the theoretical probability distribution.

achieved by observing only the modes that were split just before the output facet, without having the possibility of recombining, exhibiting interference. We note that the procedure we adopted cannot be scaled to integrated optical setups with a wider optical depth (number of interaction steps). However, it could still be used to estimate the splitting ratio of some peripheral directional couplers, enabling a first validation of the integrated device.

We report here the full characterization procedure employed for reconstructing the parameters of the direct interferometer. In the list of steps below, P_j is the power carried by the j^{th} mode after propagation in the optical circuit.

1. Coupling from $IN1$: $R_8 = \frac{P_3}{P_3+P_4}$
2. Coupling from $IN5$: $R_7 = \frac{P_2}{P_1+P_2}$
3. Coupling from $IN1$: $X = T_3 T_5 = \frac{P_3+P_4}{\sum_{j=1}^4 P_j}$
4. Coupling from $IN5$: $Y = T_2 T_4 T_5 = \frac{P_1+P_2}{\sum_{j=1}^5 P_j}$
5. Coupling from $IN1$: φ_3 is varied between $[0; 2\pi]$ driving the heaters 3 or 4. The amplitude A of the splitting ratio $\frac{P_1}{\sum_{j=1}^4 P_j}$ oscillations is extracted.

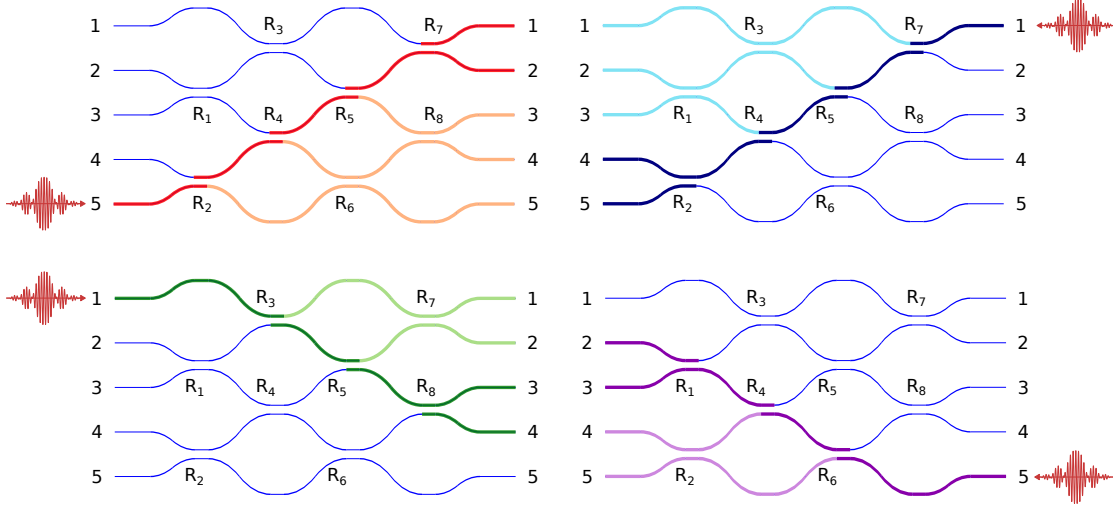


Figure 36: First chip; characterization of the splitting ratios of the outermost directional couplers: R_1 (bottom-right), R_2 (top-right), R_7 (top-left), R_8 (bottom-left). The paths traversed by the light in the photonic structure are outlined in colours, with the darker branches corresponding to the modes whose power we measured to estimate one reflectance term.

6. The chip is flipped: light is coupled in the output ports and collected from the inputs.

7. Coupling from OUT_1 : $R_2 = \frac{P_4}{P_4 + P_5}$

8. Coupling from OUT_5 : $R_1 = \frac{P_3}{P_2 + P_3}$

9. Coupling from OUT_5 : $Z = T_4 T_6 = \frac{P_2 + P_3}{\sum_{j=2}^5 P_j}$

10. $R_3 = \frac{1-X}{2} + \frac{1}{2} \sqrt{(1-X)^2 - \frac{A^2}{R_7 T_7}}$

11. $R_5 = 1 - \frac{X}{1-R_3}$

12. $R_4 = 1 - \frac{Y}{(1-R_2)(1-R_5)}$

13. $R_6 = 1 - \frac{Z}{1-R_4}$

The path of coherent light in the interferometer corresponding to steps 1, 2, 7, 8 is depicted in figure 36. We remark that, in order to estimate the amplitude A , the results of characterization with active phase shifts (described in section 5.2.2) are needed. The values of $R_{1,2,7,8}$ are however readily calculated from the passive power distributions reported in tables 7, 8.

The beam splitter characterization procedure for the inverse interferometer was readily devised as a consequence of the reflection symmetry, expressed by equation 53. Namely, it was sufficient to repeat

1 st chip (Direct transformation)									
Device #	R ₁	R ₂	R ₃	R ₄	R ₅	R ₆	R ₇	R ₈	<R>
8	51.8%	-	50.5%	-	50.3%	-	47.6%	49.3%	49.9%
9	45.4%	50.2%	40.9%	38.6%	48.4%	48.4%	49.1%	45.0%	45.8%

Table 9: Table of beam splitter reflectances for the two best devices found in the first chip. <R> is the average between the reflectance values measured on the same device. The characterization was performed with H-polarized coherent light.

2 nd chip (Inverse transformation)									
Device #	R ₁ '	R ₂ '	R ₃ '	R ₄ '	R ₅ '	R ₆ '	R ₇ '	R ₈ '	<R>
8	47.1%	49.2%	51.3%	53.3%	46.5%	45.1%	50.4%	52.3%	49.4%
9	42.4%	46.5%	42.4%	39.5%	42.0%	50.4%	45.4%	45.0%	44.2%

Table 10: Table of beam splitter reflectances for the two best devices found in the second chip. <R> is the average between the reflectance values measured on the same device. The characterization was performed with H-polarized coherent light.

steps 1-13 by exchanging mode i with mode $6 - i$, renaming the beam splitters according to the rules:

$$\begin{aligned} R_2 &\rightarrow R'_1 & R_1 &\rightarrow R'_2 & R_3 &\rightarrow R'_4 & R_4 &\rightarrow R'_3 \\ R_5 &\rightarrow R'_6 & R_6 &\rightarrow R'_5 & R_7 &\rightarrow R'_8 & R_8 &\rightarrow R'_7 \end{aligned}$$

Tables 9, 10 show the results of the characterization procedure described above. We selected at this stage the 8th and 9th interferometers from the bottom of the sample (on both chips) for subsequent calibrations and experiments. The devices are meant to be operated with horizontally-polarized light, which gives the best results in terms of power distribution and balance of the reconstructed reflectances and transmittances.

5.2.2 Calibration of the internal phase shifters

Since the described photonic devices are multiport interferometers, interference effects are readily observable as a modulation of the optical power associated to the output modes, when the internal phases are varied. By taking the square moduli of the elements of matrix 46, it is easy to identify suitable observable quantities to reconstruct the phases $\varphi_{1,\dots,4}$.

In principle, since the resistors are all enclosed in a limited area, the power dissipated in each heater could influence every phase term inside the interferometer. However, the four resistors are arranged in two couples, longitudinally separated by a ≈ 7 mm distance. Therefore, the temperature profile arising from the heaters 1 and 2 hardly affects the distant interferometer branches corresponding to the phase

terms φ_3 and φ_4 . Vice versa, the resistors 3 and 4 are not significantly coupled to the phase terms φ_1 and φ_2 . These cross-talk terms, in fact, could not be observed experimentally, being lower than the power meter noise level and the temporal drift of the coupling efficiency. This finding simplifies greatly the structure of the overall α matrices for the direct interferometer: instead of 16 terms, only two 2×2 diagonal blocks contain 8 nonzero elements.

By virtue of the superposition principle applied to the heat equation, assuming a linear response of the refractive index to (moderate) temperature increases [11], we evaluated the effect of the heaters on the internal phase delays by driving them one at a time (indeed, α could not be written as a matrix, were the thermo-optical response nonlinear).

The calibration was carried out by choosing a combination of an input and an output mode, injecting coherent light from the input and collecting the optical power routed to the selected output as the heaters dissipated different amounts of power. All the elements of α were extracted by fitting the optical power oscillations (P) with a sinusoidal function:

$$P = \mu - A \cdot \cos(\alpha_{ij} \cdot \mathcal{P} + \varphi_0), \quad (75)$$

where \mathcal{P} is the electrical power dissipated as heat, A and μ are the amplitude and mean value of the oscillations and φ_0 is the intrinsic phase difference in the absence of active electrical control. This functional shape is predicted by the theoretical form of the power fractions as a function of the internal phases, collected in matrix \mathcal{Z} : $\mathcal{Z}_{i,j} = |T_{i,j}^+|^2$. T^+ is the direct unitary transformation, whose analytic form was stated in equation 46.

Measurements were automatized by synchronizing the voltage provided by a DC power supply with the acquisition of the radiant flux by the power meter. Both instruments were controlled digitally by the same computer.

The observation of the following set of intensity oscillations allowed the full reconstruction of $\vec{\varphi}$ and α for the direct reconfigurable transformation. In the list below, P_{mn} refers to the power radiated from port m when light is coupled from the n^{th} input mode. P_{mn} is proportional to the square modulus of the corresponding unitary matrix element: $P_{mn} \propto |T_{mn}^+|^2$.

- P_{11} , reconstruction of α_{33} , α_{34}
- P_{12} , reconstruction of α_{11} , α_{12} , α_{33} , α_{34}
- P_{45} , reconstruction of α_{21} , α_{22} , α_{43} , α_{44}
- P_{55} , reconstruction of α_{21} , α_{22}

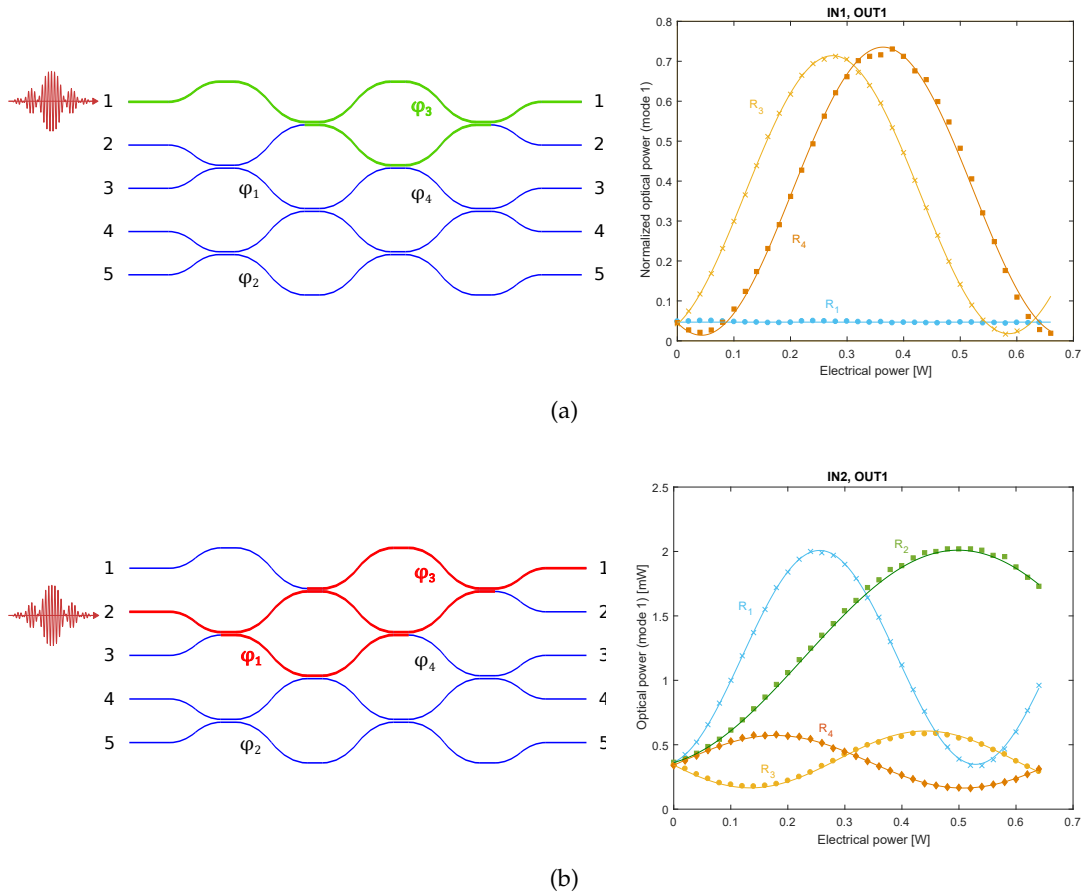


Figure 37: **a.** Influence of φ_3 on P_{11} . Left: paths traversed by light scattered from IN₁ to OUT₁. Right: experimental power ratios (data points) for device #8 fitted with sinusoidal models (solid lines), as the temperature profile is modulated with different heaters. \mathcal{R}_1 and \mathcal{R}_2 do not appreciably influence φ_3 and the output power. **b.** Influence of φ_1 and φ_3 on P_{12} . Left: paths traversed by light scattered from IN₂ to OUT₁. Right: experimental power ratios (data points) for device #8 fitted with sinusoidal models (solid lines), as the temperature profile is modulated with different heaters. \mathcal{R}_1 and \mathcal{R}_2 (\mathcal{R}_3 and \mathcal{R}_4) influence φ_1 (φ_3) alone, giving rise to power oscillations with the same visibility but different beating frequency (α 's).

Figure 37 shows the interference fringes traced by P_{11} and P_{12} when different resistors are activated. Alongside, the interferometric rings involved in the intensity modulation are highlighted.

Once again, the characterization procedure for the inverse interferometer was connected to the one employed for the first by the prescription of exchanging mode i with mode $6 - i$. Namely, the observation of the subsequent quantities allowed the calibration of the thermo-optical characteristics:

- P_{11} , reconstruction of α_{55}, α_{56}
- P_{21} , reconstruction of $\alpha_{55}, \alpha_{56}, \alpha_{77}, \alpha_{78}$
- P_{54} , reconstruction of $\alpha_{65}, \alpha_{66}, \alpha_{87}, \alpha_{88}$
- P_{55} , reconstruction of α_{88}, α_{87}

Here, the subscripts do not refer to the position in the α matrix but rather they specify a phase term/resistive heater couple.

The retrieved α matrices are:

$$\alpha_8 = \begin{pmatrix} 11.5 & 5.8 & 0 & 0 \\ -12.53 & 12.47 & 0 & 0 \\ 0 & 0 & 10.16 & -9.7 \\ 0 & 0 & 3.7 & 11.5 \end{pmatrix} \text{rad/W} \quad (76)$$

$$\alpha_9 = \begin{pmatrix} 11.8 & 5.9 & 0 & 0 \\ -11.78 & 11.41 & 0 & 0 \\ 0 & 0 & 10.45 & -8.93 \\ 0 & 0 & 4.3 & 10.43 \end{pmatrix} \text{rad/W} \quad (77)$$

for the two connected devices in the first chip, and

$$\alpha_8 = \begin{pmatrix} -10.3 & -4.4 & 0 & 0 \\ 9.8 & -10.55 & 0 & 0 \\ 0 & 0 & -9.4 & 9.87 \\ 0 & 0 & -4.5 & -10.09 \end{pmatrix} \text{rad/W} \quad (78)$$

$$\alpha_9 = \begin{pmatrix} -10.56 & -4.8 & 0 & 0 \\ 9.8 & -11.04 & 0 & 0 \\ 0 & 0 & -10.63 & 9.65 \\ 0 & 0 & -4.92 & -9.59 \end{pmatrix} \text{rad/W} \quad (79)$$

for the ones in the second. As anticipated in section 5.1.5, the opposite signs for the matrices describing the thermo-optical control on the direct and inverse interferometers are due to complementary placement

of the resistors. This expedient aimed to achieve the inversion condition with milder induced temperatures.

The measured coefficients are consistent within an order of magnitude with the prevision of equation 70. Deviations from the theoretically predicted values are mostly due to having neglected the resistor widths in the calculations or to imprecise estimation of the coefficients k and n_T in equation 64. However, the relative magnitudes between the on- and off-diagonal elements are consistent with the simplified model.

The retrieved intrinsic phases in the actively-controlled interferometric arms are:

$$\vec{\varphi}_8^0 = \begin{pmatrix} \varphi_1^0 \\ \varphi_2^0 \\ \varphi_3^0 \\ \varphi_4^0 \end{pmatrix} = \begin{pmatrix} 0.45 \\ -0.89 \\ 0.37 \\ -0.08 \end{pmatrix} \text{ rad}, \quad \vec{\varphi}_9^0 = \begin{pmatrix} \varphi_1^0 \\ \varphi_2^0 \\ \varphi_3^0 \\ \varphi_4^0 \end{pmatrix} = \begin{pmatrix} -0.44 \\ -0.34 \\ 0.22 \\ -0.03 \end{pmatrix} \text{ rad} \quad (80)$$

for the first chip, and

$$\vec{\varphi}_8^0 = \begin{pmatrix} \varphi_5^0 \\ \varphi_6^0 \\ \varphi_7^0 \\ \varphi_8^0 \end{pmatrix} = \begin{pmatrix} -0.38 \\ -0.08 \\ 0.22 \\ -1.37 \end{pmatrix} \text{ rad}, \quad \vec{\varphi}_9^0 = \begin{pmatrix} \varphi_5^0 \\ \varphi_6^0 \\ \varphi_7^0 \\ \varphi_8^0 \end{pmatrix} = \begin{pmatrix} 0.54 \\ 0.13 \\ -0.03 \\ -0.15 \end{pmatrix} \text{ rad} \quad (81)$$

for the second chip.

5.2.3 Calibration of the connection phase shifters

The procedure described above cannot be used to calibrate the phase shifters on the first segment of the second chip, employed to set the interconnection π phase delays. In fact, these phase terms at the interferometer input do not influence the power distribution collected from the output ports. A different technique, similar to Young's experiment, was devised to assess the operation of these four heaters.

The devices were coupled from the outputs, so that the input ports were illuminated and radiated spherical waves in free space, whose amplitudes were determined by the internal phases and splitting ratios. The input ports acted as five point-like sources, spaced by $w = 0.127$ mm, with a constant phase term dictated by the shape of the unitary transformation and a variable term that could be actively controlled by power dissipation in the resistors. The interference pattern generated in *far field* carries information about the phase difference between the point-like coherent sources. In fact, assuming to observe intensity fringes in far field ($L \gg \frac{25w^2}{\lambda} \approx 0.5$ m, where L is the distance between the facet and the imaging plane) and under

small angles with respect to the optical axis, the following form for the intensity profile can be stated.

$$I \propto \sum_{j=0}^{N-1} \left(\sum_{k=j}^{N-1} \left(E_k E_{k-j} e^{i(\varphi_k - \varphi_{k-j})} \right) e^{i(2\pi j \frac{w}{\lambda L} y)} \right) + \text{c.c.}, \quad (82)$$

where E_k is the real field amplitude of point source k , φ_k is its phase, N is the number of point sources, y is the coordinate parallel to the facet, on the imaging plane, and c.c. identifies the complex conjugate of the sum.

$I(y)$ is therefore a finite Fourier series, with the contribution of $N - 1$ different spatial frequencies, $f_j = j \cdot \frac{w}{\lambda L}$. Each Fourier coefficient is determined by the amplitude and phase of all the point sources separated by a distance $j \cdot w$. If only two such sources contribute to the interference pattern, the Fourier coefficient for f_j simplifies to $E_k E_{k-j} e^{i(\varphi_k - \varphi_{k-j})}$ and the phase difference between the two modes can be extracted as the phase of the Fourier peak, while the heaters are driven.

The experimental setup for this characterization method is portrayed schematically in figure 38. An image of the illuminated input ports was formed with a microscope objective. The image magnification was kept low (by choosing $q \approx 6p$), in order to satisfy the condition for far field interference at reasonable values of L . Directly beyond the image plane an adjustable slit was positioned, in order to select only the two modes whose phase difference we were interested in, to contribute to the interference pattern. Light was then propagated in free space for a distance L , where an image of the interference pattern was acquired with a CMOS camera. This spatial pattern was stored digitally and integrated along the coordinate z , which carried no information on the interference of the point sources. Finally, $\varphi_k - \varphi_{k-j}$ was estimated with the phase of the appropriate spatial frequency peak at f_j , by employing a fast Fourier transform algorithm. This procedure was synchronized with the control of each resistor with a varying voltage, and the elements of α were produced by a linear fit of the phase delay as a function of the Joule power, according to equation 63. An example of interference pattern analysis is reported in figure 39.

The following measurements allowed a full reconstruction of the matrix α describing the interconnection phase shifters. The 5th mode was chosen as the reference for the definition of each phase difference (the 5th waveguide was the only one without a resistor patterned directly above). Once again, this set of resistors was experimentally assessed to be decoupled from the other reconfigurable phase terms, so that α consisted of 16 elements.

- Coupling from OUT_3 : reconstruction of φ_α

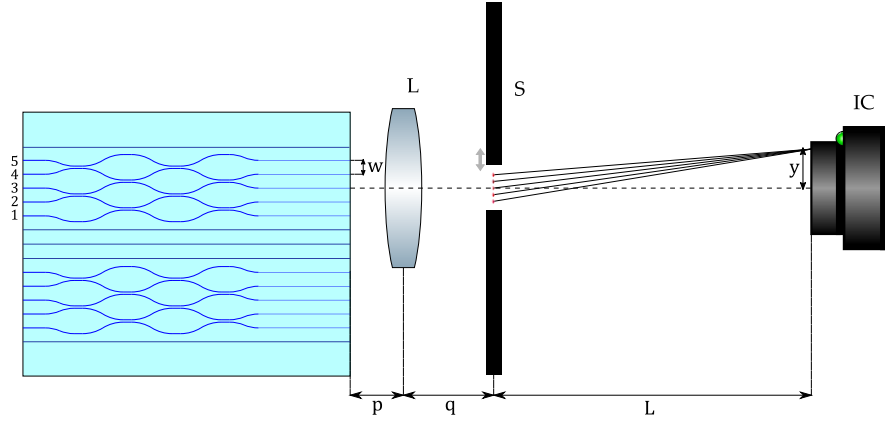


Figure 38: Experimental setup for the calibration of the phase shifters with the displacement of interference fringes. An image of the five interferometer modes is formed with a positive lens or microscope objective (L) (p is the distance between the sources and the lens, q is the distance between the lens and the image). A slit (S) with variable width is placed on the image plane in order to cut the modes that complicate the Fourier analysis of the fringe pattern. After the slit, light propagates in free space for a distance L , sufficient for the observation of far-field interference. There, an imaging camera (IC) is positioned and the fringe pattern is acquired.

- Coupling from OUT_4 : reconstruction of φ_b . The slit blocked the image of IN_1 .
- Coupling from OUT_2 : reconstruction of φ_c . The slit blocked the images of IN_1 and IN_2 .
- Coupling from OUT_2 : reconstruction of φ_d . The slit blocked the images IN_1 , IN_2 , IN_3 .

The modes in which to couple light were chosen with the purpose of optimizing the amplitude of the desired Fourier coefficient and improve its prominence in the spatial spectrum.

The reconstructed α matrices are reported below.

$$\alpha_8^j = \begin{pmatrix} 32.8 & 14.6 & 1.3 & -12.6 \\ 17.7 & 28.9 & 10.6 & -6.9 \\ 8.5 & 13.3 & 20.9 & 0 \\ 3.7 & 5.5 & 9.7 & 14.5 \end{pmatrix} \text{ rad/W} \quad (83)$$

$$\alpha_9^j = \begin{pmatrix} 31.3 & 13.7 & 2.6 & -14.8 \\ 16.1 & 27.5 & 7.2 & -7.8 \\ 7.8 & 13.3 & 24.6 & 0.7 \\ 3.4 & 6.2 & 10.1 & 15.1 \end{pmatrix} \text{ rad/W} \quad (84)$$

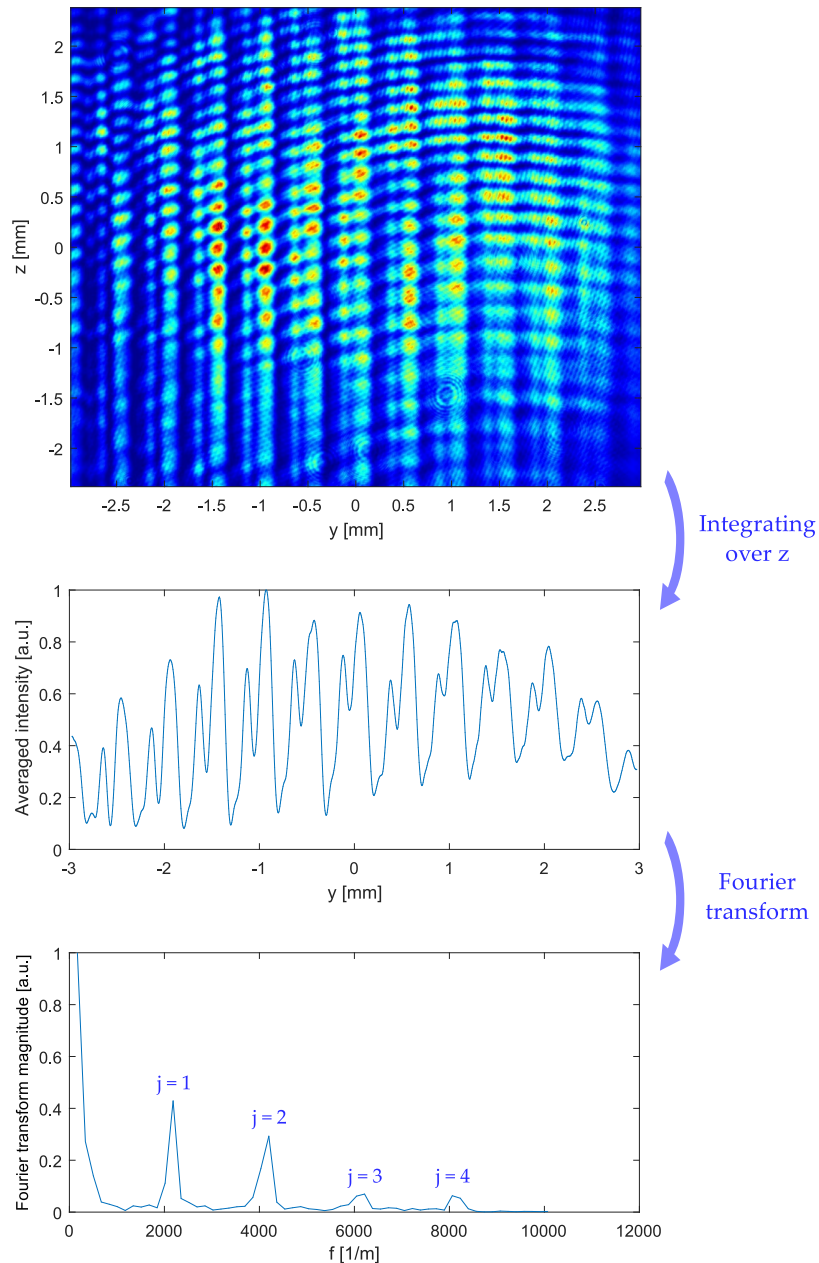


Figure 39: Far-field fringe pattern obtained by interference of five interferometer modes, by the measurement setup of figure 38. The intensity modulation in the z direction is probably due to interference with part of the coherent beam that did not couple inside the waveguides. Integrating over the z coordinate, perpendicular to the line connecting the light sources, produces the oscillating function portrayed in the central plot. In the lower graph, the magnitude of the Fourier-transformed averaged intensity is plotted. Four peaks at $f \neq 0$ are distinctly visible, corresponding to the four different spatial separation values between couples of sources. Monitoring, for example, the phase of the Fourier transform at the $j = 4$ spatial frequency, while the heaters dissipate different powers, allows to reconstruct their influence on φ_α , i. e. the first row of α .

These results are in strong agreement with the predictions of equation 73, when correcting with a ≈ 2.2 multiplicative factor. This discrepancy could be due to an imprecise estimation of n_T and k for our glass substrate. We remark that the numerical results of equation 73 are more accurate than the other figures reported in this work, since they account for the finite width of the resistors.

Finally, we remark that the α and $\vec{\varphi}_0$ values retrieved ensure that the adopted damage threshold $\mathcal{P}_{\max} = 0.7 \div 0.8 \text{ W}$ does not provide a fundamental restriction on the phase shifts that can be obtained in the interferometric arms. In fact, each phase term can be varied in the interval $[0; 2\pi]$ without exceeding \mathcal{P}_{\max} on any of the heaters.

5.2.4 *Interfacing the chips*

Once the integrated optical circuits were separately characterized, the feasibility of interconnecting them in cascade was examined. This layout is in fact one of the outlined configurations for Hamiltonian learning experiments (see chapter 4).

Two aluminum supports for the chips were designed, with the dual role of providing a large thermal capacitance and dissipating in the environment the heat generated by the resistive heaters, and of mounting the devices onto the translation stages that facilitated their mutual alignment.

We fixed the two chips on two different micrometric manual stages, providing all the translation and rotation degrees of freedom required for the optimization of the coupling efficiency between the waveguides inscribed in the different chips. The alignment procedure involved the maximization of the power transmitted by the straight waveguides surrounding the desired interferometers, introduced in section 5.1.3.

The insertion losses (IL) of the two cascaded chips were evaluated injecting light in the chip with a single-mode optical fiber and collecting the output light with a microscope objective (see the fiber butt-coupling technique described in section 3.3.2).

The losses measured in this configuration should provide a reliable indication of those occurring in experiments with quantum light. In fact, in the latter, photons will be launched in the devices with single-mode fiber arrays, supporting spatial mode profiles similar to the one carried by the single fiber in our setup, and collected with multi-mode fiber arrays. The latter provide indeed a collection efficiency similar to the microscope objective, being both inherently insensitive to the spatial pattern of the interferometer modes.

The position of the fiber tip and of the output and input ports of the multimode interferometers was micrometrically tuned in order to maximize the coupling efficiency. A picture of the coupling setup with the interconnected devices is reported in figure 40.

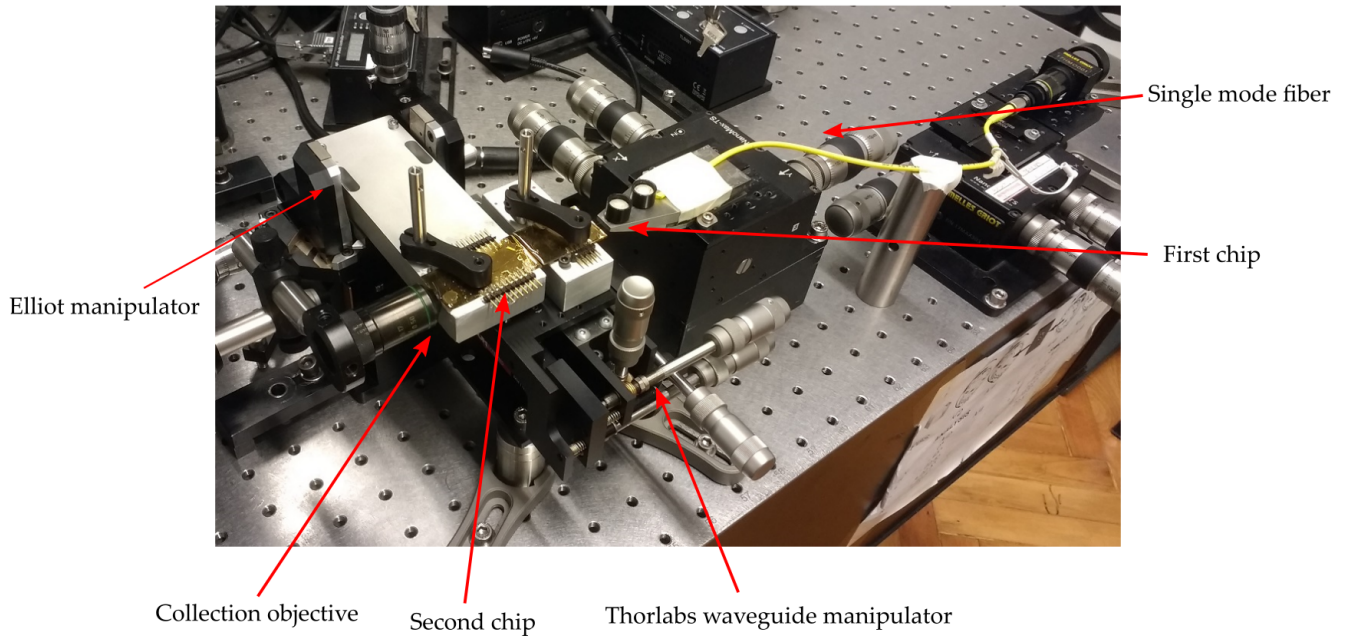


Figure 40: The two chips mounted on two different micrometric manipulators and coupled together. Light is coupled inside the first chip via one single-mode fiber.

On the whole, insertion losses of $IL = 14.4$ dB were retrieved. This figure includes the propagation and bending losses inside the devices, the Fresnel losses at each glass-air interface, the injection coupling losses due to imperfect overlap between the fiber and waveguide modes, and the losses due to coupling from the output ports of the direct interferometer to the input ports of the inverse. In fact, even if the relative positioning could be perfectly optimized, some losses could occur, owing to small waveguide properties variations and to beam divergence in the thin intermediate air gap. By contrast, in the first interferometer alone the insertion losses amounted to $IL_1 = 6.4$ dB.

CONCLUSIONS

The implementation of two reconfigurable, 5-modes interferometers for Hamiltonian learning demonstrations with quantum states of light was reported. The photonic devices can access a vast range of unitary transformations by regulating 4 controlled phase delays.

The scope of the unitary matrices set was studied as a fundamental preliminary task during this work. In particular, the second interferometer can invert the evolution realized by the first: the conditions for this inversion to take place were formulated and derived. The capability of demonstrating an inverse evolution is a critical requirement for the IQLE algorithm.

The interferometers were fabricated in alumino-borosilicate glass by Femtosecond Laser Micromachining (FLM). The fidelity of the power splitting distribution to the theoretical predictions was found to be excellent ($F > 0.99$). This result highlights the maturity reached by this fabrication technique, and the leading role it plays as a technological platform for Integrated Quantum Photonics.

Gold resistive heaters were patterned on top of the waveguides, enabling the thermo-optic tuning of four internal phases per interferometer and four interconnection phases in the initial tract of the second photonic structure. These devices are among the most complex reconfigurable circuits realized by FLM up to date.

The photonic devices have been brought to "La Sapienza" university, in the Quantum Optics research laboratories, to conduct experiments with single-photon sources. Currently, the interferometers are being extensively characterized with *quantum process tomography* techniques, with and without active phase control. Experiments concerning the demonstration and the quantitative assessment of the two variants of Hamiltonian learning will start soon.

In addition, the two integrated optical circuits are also well suited for realizing a quantum cryptography model called *quantum enigma machine* [91]. The latter is a method for efficient communication encryption: a message is encoded with the state of a qubit collection and an m -bit encryption key is mapped to one of 2^m unitary transformations, acting upon the qubits. The reconfigurable interferometers possess exactly the structure of the encryption and decryption stages of a quantum enigma machine.

BASIC QUANTUM INFORMATION CONCEPTS

A.1 QUBITS

A quantum bit, or *qubit* for short, is the extension of the concept of bit, the "primitive cell" of digital information storage and transmission, to quantum mechanical systems. Any two-level (or approximately two-level) quantum mechanical system can be described with the qubit mathematical abstraction.

Just as the classical bit has a state - either 0 or 1 - a qubit can have the quantum states $|0\rangle$ and $|1\rangle$. In fact, these states form an orthonormal basis for the vector space of the qubit. The substantial difference is that for the quantum bit linear combinations of these two states are also allowed, justified by the validity of the *superposition principle* in quantum mechanics. The most generic qubit superposition reads:

$$|\psi\rangle = \alpha|0\rangle + \beta|1\rangle \quad (85)$$

Unlike in classical computers, that can retrieve the content of classical bits by fetching data from their memory, it is not possible to examine a qubit and retrieve its quantum state (the values of α and β). Quantum mechanics asserts that we can acquire much less information about the state: when we measure a qubit we obtain $|0\rangle$ with a probability of $|\alpha|^2$ and $|1\rangle$ with a probability of $|\beta|^2$. The normalization condition $|\alpha|^2 + |\beta|^2 = 1$ holds, because probabilities must sum to one. It is not possible to copy the qubit on other two-level systems in order to statistically sample α and β , either: the no-cloning theorem [4] forbids the existence of such a copying machine for generic quantum states. This dichotomy between the infinite amount of possibilities for building a superposition state and the limited observations we can make lies at the heart of quantum computation and quantum information.

Let us consider a system of N qubits. The most generic state of this qubit collection is expressed as:

$$|\psi\rangle = \sum \alpha_{x_1 x_2 \dots x_N} |x_1 x_2 \dots x_N\rangle, \quad (86)$$

where the sum is carried out over all possible strings containing either 0 or 1 at each position x_i . Therefore, such a multiple-qubit superposition state is defined by 2^N amplitudes: this mathematical fact reinstates the enormous potential for computational power of a collection of qubits.

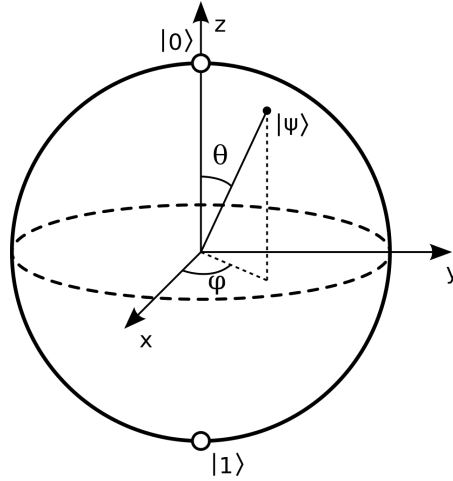


Figure 41: Bloch sphere representation of a qubit $|\psi\rangle$.

Because $|\alpha|^2 + |\beta|^2 = 1$, the superposition state in 85 can be rewritten as:

$$|\psi\rangle = \cos\left(\frac{\theta}{2}\right)|0\rangle + e^{i\phi}\sin\left(\frac{\theta}{2}\right)|1\rangle, \tag{87}$$

where θ and ϕ are real angles. We neglected the common phase factor between the amplitudes of $|0\rangle$ and $|1\rangle$. This notation corresponds to identifying a point $(\sin\theta \cos\phi, \sin\theta \sin\phi, \cos\theta)$ on the surface of a three-dimensional sphere of unit radius. This sphere, depicted in figure 41, is called *Bloch sphere* and is often adopted in quantum computation in order to visualize operations performed on single qubits.

A.2 QUANTUM CIRCUITS AND QUANTUM GATES

Quantum algorithms are often specified with the language of *quantum circuits*, assemblies of discrete sets of components (quantum operations, or *gates*) that describe computational procedures. This framework allows to estimate the computational cost associated to carrying out a certain procedure, by counting the number of gates appearing in the quantum circuit.

It has been proven that a limited set of operations is needed for performing *universal quantum computation*, i. e. being able to approximate any given unitary transformation of a generic multi-qubit state. One such set is composed of arbitrary single-qubit *rotation operations* and only one two-qubit controlled operation: the CNOT gate [4]. Since these gates are quite ubiquitous in quantum algorithms, we will provide the related definitions below.

Introducing the Pauli matrices (operating on single qubits):

$$\sigma_1 = \sigma_x = \begin{pmatrix} 0 & 1 \\ 1 & 0 \end{pmatrix} \quad \sigma_2 = \sigma_y = \begin{pmatrix} 0 & -i \\ i & 0 \end{pmatrix} \quad \sigma_3 = \sigma_z = \begin{pmatrix} 1 & 0 \\ 0 & -1 \end{pmatrix}$$

(88)

we define the rotation operations by exponentiation¹:

$$\begin{aligned} R_x(\theta) &= e^{-i\frac{\theta}{2}\sigma_x} = \begin{pmatrix} \cos\left(\frac{\theta}{2}\right) & -i\sin\left(\frac{\theta}{2}\right) \\ -i\sin\left(\frac{\theta}{2}\right) & \cos\left(\frac{\theta}{2}\right) \end{pmatrix} \\ R_y(\theta) &= e^{-i\frac{\theta}{2}\sigma_y} = \begin{pmatrix} \cos\left(\frac{\theta}{2}\right) & -\sin\left(\frac{\theta}{2}\right) \\ \sin\left(\frac{\theta}{2}\right) & \cos\left(\frac{\theta}{2}\right) \end{pmatrix} \\ R_z(\theta) &= e^{-i\frac{\theta}{2}\sigma_z} = \begin{pmatrix} e^{-i\frac{\theta}{2}} & 0 \\ 0 & e^{i\frac{\theta}{2}} \end{pmatrix} \end{aligned} \quad (89)$$

In the Bloch sphere representation (see figure 41), the operation $R_n(\theta)$ is equivalent to rotating the state vector about the n axis by an angle θ .

The *Hadamard gate* H is very commonly adopted in the construction of quantum circuits.

$$H = \frac{1}{\sqrt{2}} \begin{pmatrix} 1 & 1 \\ 1 & -1 \end{pmatrix} \quad (90)$$

It mixes with balanced weights the computational basis states and can be constructed by the composition of rotation operations (neglecting an innocuous common phase term): $H = e^{i\frac{\pi}{2}} R_x(\pi) R_y\left(\frac{\pi}{2}\right)$.

The *CNOT* (controlled-NOT) gate is a conditional operation that flips a *target* qubit depending on the state of a *control* qubit. If the control qubit is in the state $|0\rangle$, the target is left untouched, while if the control qubit is described by $|1\rangle$, the target is negated. In any case the state of the control qubit is not changed during the CNOT application. This behaviour is extended linearly to a generic superposition state of a two-qubit system, leading to the following transformation:

$$\alpha|00\rangle + \beta|01\rangle + \gamma|10\rangle + \delta|11\rangle \rightarrow \alpha|00\rangle + \beta|01\rangle + \gamma|11\rangle + \delta|10\rangle, \quad (91)$$

where the control qubit is listed first and the target qubit second in the state vectors.

A.3 THE DENSITY OPERATOR

The historical approach to quantum mechanics uses the language of state vectors. An alternative, powerful formulation adopts a tool called density matrix, or density operator. This restatement of the theory is particularly convenient in quantum information, for treating systems interacting with an environment and for the description of individual subsystems of a composite quantum system.

¹ We omit the hat symbol for operators, substituted here with their matrix representation

The density operator provides a language for describing systems whose state is not completely known. If a quantum system is in one of a number of states $|\psi_i\rangle$ with a respective probability p_i , its density operator is defined as:

$$\hat{\rho} = \sum_i p_i |\psi_i\rangle \langle\psi_i| \quad (92)$$

The time evolution of the density operator is described by a unitary transformation. If the quantum states underwent the evolution $|\psi_i\rangle \rightarrow \hat{U}|\psi_i\rangle$, then the density operator will transform like $\hat{\rho} \rightarrow \hat{U}\hat{\rho}\hat{U}^\dagger$. \hat{U} is in any case a unitary operator or matrix.

The expectation value of an observable quantity associated to the operator \hat{A} is calculated as

$$\langle\hat{A}\rangle = \text{tr}(\hat{\rho}\hat{A}), \quad (93)$$

where tr is the trace operation: if $|j\rangle$, $j = 1, 2, \dots$ is an orthonormal basis for the Hilbert space of state vectors, $\text{tr}(\hat{B}) = \sum_j \langle j|\hat{B}|j\rangle$.

A.4 QUANTUM STATE TOMOGRAPHY

An essential requirement for assessing the operation of a quantum algorithm is the capability to perform a reconstruction of the quantum state, or equivalently its density matrix. A family of techniques, called *state tomography*, have been devised for this purpose. Here, we will describe only the simplest formulation for the reconstruction of a single qubit state, for simplicity.

The density matrix of a single qubit can be expressed as [2]:

$$\rho = \frac{1}{2} \left(\mathbb{1} + \sum_{k=1}^3 r_k \sigma_k \right), \quad (94)$$

where $\vec{r} = (r_1 \ r_2 \ r_3)$ is a real-valued three-dimensional vector and σ_k are the Pauli matrices.

(We omit the hat symbol for operators, substituted here with their matrix representation).

Because of the trace orthogonality property of Pauli matrices,

$$\text{tr}(\sigma_k \cdot \sigma_j) = 2\delta_{jk}, \quad (95)$$

it follows that \vec{r} , and therefore ρ , can be reconstructed from the three measurement results:

$$r_k = \langle\sigma_k\rangle = \text{tr}(\rho\sigma_k) \quad (96)$$

(see equation 93). Pauli operators are easily implemented in every physical platform for quantum computation (e. g. with a beam splitter and a phase shifter in linear optics); therefore, the expectation

value $\langle \sigma_k \rangle$ can be estimated by averaging measurements on the related observable quantity on an ensemble of identical qubits.

An arbitrary density matrix of n qubits can be characterized in a similar fashion, by performing measurements of observables which are the product of Pauli matrices [4].

INTEGRATED OPTICS PRINCIPLES AND COMPONENTS

B.1 THE OPTICAL WAVEGUIDE

The fundamental element for any integrated optics structure is the dielectric waveguide. In its simplest form, the device consists of an elongated, wire-like region of high refractive index n_2 (core) enclosed in a dielectric presenting a lower refractive index n_1 (cladding), as in figure 42. Like optical fibers, the dielectric waveguide allows to confine light in a micrometric region and guide it along a desired path, due to *total internal reflection*, occurring if $n_2 > n_1$.

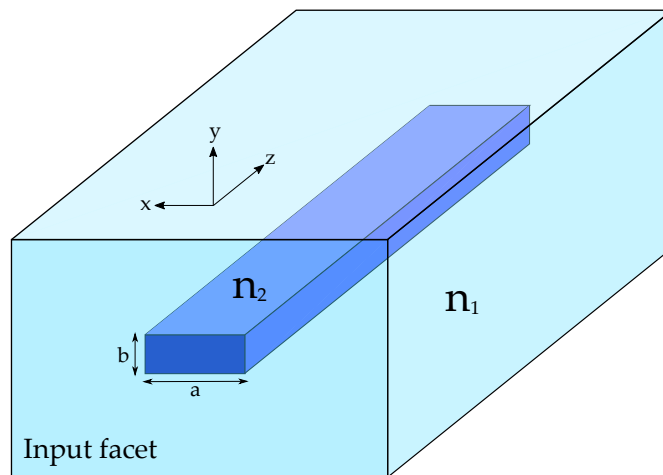


Figure 42: Schematic representation of a rectangular channel waveguide. A core region with refractive index n_2 is surrounded by a cladding n_1 . The waveguide extends along the direction z .

In general, it is not possible to solve analytically the Maxwell equations in the composite dielectric; approximate or numerical methods must be employed. However, in the case of low index contrast between core and cladding, i. e. $\frac{n_2 - n_1}{n_2} \ll 1$, some general features of the guided fields can be identified:

- the electric field is almost entirely polarized orthogonally to the waveguide axis and its scalar part can be written in the phasor form:

$$\mathcal{E}(x, y, z, t) = E(x, y)e^{i(\beta z - \omega t)}, \quad (97)$$

where $E(x, y)$ is the transverse spatial field profile, ω is the angular frequency and β is the component of the wavevector along the propagation direction z , also called *propagation constant*.

- the waveguide supports *guided* and *radiative* solutions (modes), the former being confined inside and in proximity of the core region and the latter extending outwards in the cladding. The guided modes form a discrete set and their propagation constants are quantized, according to the dispersion relation $\beta = \beta_{m,n}^p(\omega)$. The subscripts m and n are integer values that specify the mode order, while $p = \{1;2\}$ denotes the polarization state. The number of modes supported by the waveguide increases with increasing radiation frequency ω , lateral core dimensions a, b and refractive index contrast $\Delta n = n_2 - n_1$. The lowest order modes, corresponding to $m = n = 0$ are called *fundamental modes*. If the waveguide supports only these two (one for each polarization state) eigensolutions, then it is called "single-mode waveguide". Many integrated optics devices must be constructed out of single-mode waveguides, in order to avoid design complications arising interactions and power transfer among different modes.
- the mode transverse profile $E(x, y)$ extends outside of the core region and decays exponentially in the cladding. The lower the refractive index contrast Δn , the larger the extent of these exponential tails.

B.2 THE DIRECTIONAL COUPLER

When two single-mode waveguides are brought close enough that the evanescent tail of the mode supported by the first starts to overlap with the core of the second, power transfer between the two modes is observed, as the waves propagate along z .

This phenomenon of evanescent wave coupling is usually studied making the perturbative assumption that the power is transferred slowly between the two waveguides. Under this ansatz, the fields inside the waveguides have the same form of equation 97, but the amplitude of the spatial profile is modulated by a function $c(z)$ during propagation along z :

$$\mathcal{E}_j(x, y, z, t) = c_j(z) \cdot E_j(x, y) e^{i(\beta_j z - \omega t)}, \quad (98)$$

where the subscript $j = \{1;2\}$ denotes either of the waveguides.

The differential equations describing the evolution of $c(z)$ are formulated in the framework of *coupled mode theory* [92]:

$$\begin{cases} \frac{dc_1(z)}{dz} = -i\kappa e^{i\Delta\beta z} \cdot c_2(z) \\ \frac{dc_2(z)}{dz} = -i\kappa e^{-i\Delta\beta z} \cdot c_1(z) \end{cases} \quad (99)$$

In equations 99, the *detuning* $\Delta\beta = \beta_1 - \beta_2$ stands for the difference between the propagation constants of the two modes and κ is the

coupling coefficient, proportional to the overlap integral between the modes supported by the two waveguides:

$$\kappa = \frac{\omega\epsilon_0}{4}(n_2^2 - n_1^2) \cdot \iint_{\text{core}} E_1^* \cdot E_2 \, dx \, dy, \quad (100)$$

where the integration is performed on the core region of waveguide 1.

The solutions of equations 99, subject to light insertion in waveguide 1 only ($c_1(0) = c_0$, $c_2(0) = 0$), are:

$$\begin{cases} c_1(z) = c_0 e^{i\frac{\Delta\beta}{2}z} \left(\cos(\gamma z) - i\frac{\Delta\beta}{2\gamma} \sin(\gamma z) \right) \\ c_2(z) = -ic_0 e^{-i\frac{\Delta\beta}{2}z} \frac{\kappa}{\gamma} \sin(\gamma z) \end{cases} \quad (101)$$

with γ defined as:

$$\gamma = \sqrt{\left(\frac{\Delta\beta}{2}\right)^2 + \kappa^2} \quad (102)$$

Once the expression for the dependence of the amplitudes on z is found, it is possible to evaluate the trend of the power transfer between the waveguides by taking their square moduli: $P_j(z) = |c_j(z)|^2$. In particular, energy is exchanged with the (angular) frequency γ during propagation along z . Figure 43 shows power transfer curves for different values of $\Delta\beta$ and κ .

A particularly interesting case is the situation of identical propagation constants, $\Delta\beta = 0$. Here, for power initially localized to the first waveguide ($P_2(0) = 0$), the coupled mode equations produce the solutions:

$$\begin{cases} P_1(z) = P_1(0) \cdot \cos^2(\kappa z) \\ P_2(z) = P_1(0) \cdot \sin^2(\kappa z) \end{cases} \quad (103)$$

A complete power transfer from the first to the second waveguide is possible, happening for interaction lengths of $z_m = (m + \frac{1}{2})\frac{\pi}{\kappa}$ (with integer m).

Evanescent wave coupling is exploited in one of the fundamental building blocks of integrated optics circuits: the directional coupler. It is a four-ports device that allows to obtain a division of the power launched in the input ports at the outputs, with a fixed splitting ratio. In the most common design, two waveguides, initially spaced by a distance w , such that evanescent coupling is negligible, are brought closer together at an *interaction distance* d by curved joint sections. Here, power transfer can take place, the final distribution being determined by the interaction length L . In the last section of the device, the waveguides are once again split towards different output ports. The device geometry is sketched in figure 44.

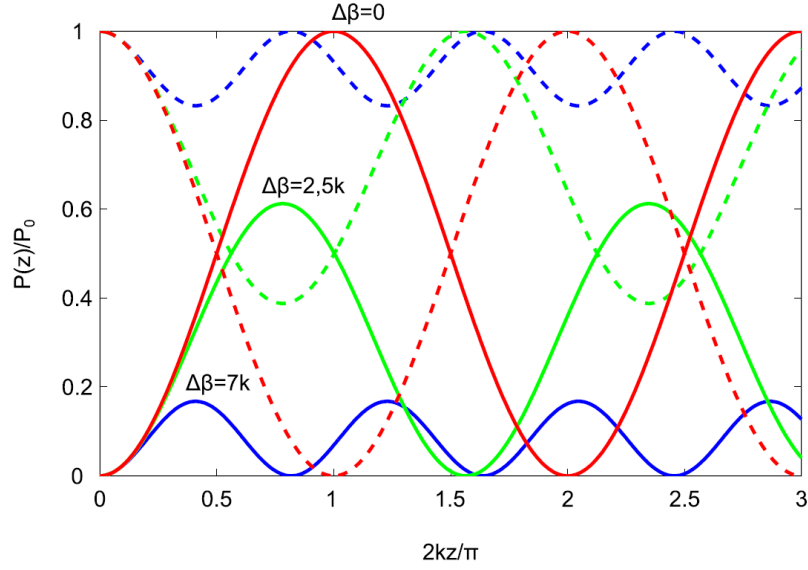


Figure 43: Optical power in two evanescently-coupled waveguides: power fraction left in waveguide 1 (dashed curves) and transferred to waveguide 2 (continuous curve). Light was initially launched in waveguide 1 only. Curves are plotted as a function of the coupling length, normalized to $\frac{\pi}{2k}$. For higher values of the detuning $\Delta\beta$, power transfer is faster but less efficient. In the case of perfect matching of the propagation constants ($\Delta\beta = 0$, red curves) a complete power transfer is periodically achieved. Image taken from [80].

The *reflectance* R and *transmittance* T of a directional coupler in which light is coupled from IN 1 are defined as:

$$R = \frac{P_{\text{bar}}}{P_{\text{bar}} + P_{\text{cross}}}, \quad T = \frac{P_{\text{cross}}}{P_{\text{bar}} + P_{\text{cross}}}, \quad (104)$$

where P_{bar} is the power left in the same waveguide in which light was initially launched (power flowing out of OUT 1) and P_{cross} is the power transferred to the other waveguide (power flowing out of OUT 2). These expressions hold also in case (balanced) losses affect propagation in the device: the quantities are normalized to the optical power flowing out of the device, instead of P_{IN1} .

As long as the device symmetry is not broken (e. g. by imbalanced losses), the reflectance and transmittance that describe power division of light initially coupled in IN 2 are the same. These considerations can be summarized by writing a linear transfer law relating the output to the input fields:

$$\begin{pmatrix} \mathcal{E}_{\text{OUT1}} \\ \mathcal{E}_{\text{OUT2}} \end{pmatrix} = \begin{pmatrix} \sqrt{R} & i\sqrt{T} \\ i\sqrt{T} & \sqrt{R} \end{pmatrix} \cdot \begin{pmatrix} \mathcal{E}_{\text{IN1}} \\ \mathcal{E}_{\text{IN2}} \end{pmatrix}, \quad (105)$$

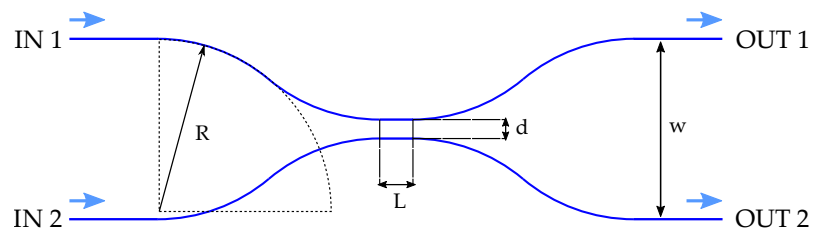


Figure 44: Schematic layout of a directional coupler. R is the radius of curvature of the bent waveguide tracts, w is the distance between input (output) ports, d and L are the interaction distance and length of the region where evanescent coupling takes place.

where the $\frac{\pi}{2}$ phase factor carried by fields that "crossed" the interaction region arises naturally from the solution of 99. This formalism outlines the perfect correspondence of a directional coupler to a bulk-optical beam splitter.

BIBLIOGRAPHY

1. Feynman, R. P. Simulating physics with computers. *International journal of theoretical physics* **21**, 467–488 (1982).
2. Benenti, G., Casati, G. & Strini, G. *Principles of Quantum Computation and Information. Volume I: Basic Concepts* (World Scientific Publishing Co Inc, 2007).
3. Shor, P. W. Polynomial-time algorithms for prime factorization and discrete logarithms on a quantum computer. *SIAM review* **41**, 303–332 (1999).
4. Nielsen, M. A. & Chuang, I. *Quantum computation and quantum information* 2002.
5. Georgescu, I., Ashhab, S. & Nori, F. Quantum simulation. *Reviews of Modern Physics* **86**, 153 (2014).
6. Aspuru-Guzik, A., Dutoi, A. D., Love, P. J. & Head-Gordon, M. Simulated quantum computation of molecular energies. *Science* **309**, 1704–1707 (2005).
7. Lanyon, B. P. *et al.* Towards quantum chemistry on a quantum computer. *Nature Chemistry* **2**, 106–111 (2010).
8. Reck, M., Zeilinger, A., Bernstein, H. J. & Bertani, P. Experimental realization of any discrete unitary operator. *Physical Review Letters* **73**, 58 (1994).
9. Crespi, A. *et al.* Integrated multimode interferometers with arbitrary designs for photonic boson sampling. *Nature Photonics* **7**, 545–549 (2013).
10. Matthews, J. C., Politi, A., Stefanov, A. & O’Brien, J. L. Manipulation of multiphoton entanglement in waveguide quantum circuits. *Nature Photonics* **3**, 346–350 (2009).
11. Flamini, F. *et al.* Thermally reconfigurable quantum photonic circuits at telecom wavelength by femtosecond laser micromachining. *Light: Science & Applications* **4**, e354 (2015).
12. Peruzzo, A. *et al.* A variational eigenvalue solver on a photonic quantum processor. *Nature communications* **5** (2014).
13. Griffiths, D. J. *Introduction to quantum mechanics* (Cambridge University Press, 2016).
14. Kempe, J. Quantum random walks: an introductory overview. *Contemporary Physics* **44**, 307–327 (2003).
15. Crespi, A. *et al.* Anderson localization of entangled photons in an integrated quantum walk. *Nature Photonics* **7**, 322–328 (2013).

16. Mohseni, M., Rebentrost, P., Lloyd, S. & Aspuru-Guzik, A. Environment-assisted quantum walks in photosynthetic energy transfer. *The Journal of chemical physics* **129**, 11B603 (2008).
17. Broome, M. A. *et al.* Discrete single-photon quantum walks with tunable decoherence. *Physical review letters* **104**, 153602 (2010).
18. Caruso, F., Crespi, A., Ciriolo, A. G., Sciarrino, F. & Osellame, R. Fast escape of a quantum walker from an integrated photonic maze. *Nature Communications* **7** (2016).
19. Deutsch, D. *Quantum theory, the Church-Turing principle and the universal quantum computer* in *Proceedings of the Royal Society of London A: Mathematical, Physical and Engineering Sciences* **400** (1985), 97–117.
20. Lloyd, S. Universal quantum simulators. *Science*, 1073–1078 (1996).
21. Grover, L. K. Quantum mechanics helps in searching for a needle in a haystack. *Physical review letters* **79**, 325 (1997).
22. Wittek, P. *Quantum machine learning: what quantum computing means to data mining* (Academic Press, 2014).
23. Lloyd, S., Mohseni, M. & Rebentrost, P. Quantum algorithms for supervised and unsupervised machine learning. *ArXiv e-prints*. arXiv: [1307.0411 \[quant-ph\]](#) (2013).
24. Narayanan, A. & Menneer, T. Quantum artificial neural network architectures and components. *Information Sciences* **128**, 231–255 (2000).
25. Li, Z., Liu, X., Xu, N. & Du, J. Experimental realization of a quantum support vector machine. *Physical review letters* **114**, 140504 (2015).
26. Cai, X.-D. *et al.* Entanglement-based machine learning on a quantum computer. *Physical review letters* **114**, 110504 (2015).
27. James, G., Witten, D., Hastie, T. & Tibshirani, R. *An introduction to statistical learning* (Springer, 2013).
28. Wiebe, N., Kapoor, A. & Svore, K. M. Quantum nearest-neighbor algorithms for machine learning. *Quantum Information and Computation* **15** (2015).
29. Dürr, C. & Høyer, P. A quantum algorithm for finding the minimum. *ArXiv e-prints*. arXiv: [quant-ph/9607014 \[quant-ph\]](#) (1996).
30. Wiebe, N., Kapoor, A. & Svore, K. Quantum algorithms for nearest-neighbor methods for supervised and unsupervised learning. *ArXiv e-prints*. arXiv: [1401.2142 \[quant-ph\]](#) (2014).
31. Friedman, J., Hastie, T. & Tibshirani, R. *The Elements of Statistical Learning: Data Mining, Inference, and Prediction* (Springer-Verlag New York, 2009).

32. Freund, Y. & Schapire, R. E. *A decision-theoretic generalization of on-line learning and an application to boosting in European conference on computational learning theory* (1995), 23–37.
33. Kim, K. *et al.* Quantum simulation of frustrated Ising spins with trapped ions. *Nature* **465**, 590–593 (2010).
34. Hauke, P., Cucchietti, F. M., Tagliacozzo, L., Deutsch, I. & Lewenstein, M. Can one trust quantum simulators? *Reports on Progress in Physics* **75**, 082401 (2012).
35. Wiebe, N., Granade, C., Ferrie, C. & Cory, D. G. Hamiltonian learning and certification using quantum resources. *Physical review letters* **112**, 190501 (2014).
36. Haake, F. *Quantum signatures of chaos* (Springer Science & Business Media, 2013).
37. Cucchietti, F. M., Pastawski, H. M. & Wisniacki, D. A. Decoherence as decay of the Loschmidt echo in a Lorentz gas. *Physical Review E* **65**, 045206 (2002).
38. Wang, J. *et al.* Experimental quantum Hamiltonian learning. *Nature Physics* **13**, 551–555 (2017).
39. Wang, J. *et al.* Chip-to-chip quantum photonic interconnect by path-polarization interconversion. *Optica* **3**, 407–413 (2016).
40. Pronko, P. *et al.* Machining of sub-micron holes using a femtosecond laser at 800 nm. *Optics communications* **114**, 106–110 (1995).
41. Davis, K. M., Miura, K., Sugimoto, N. & Hirao, K. Writing waveguides in glass with a femtosecond laser. *Optics letters* **21**, 1729–1731 (1996).
42. Gattass, R. R. & Mazur, E. Femtosecond laser micromachining in transparent materials. *Nature photonics* **2**, 219–225 (2008).
43. Osellame, R., Cerullo, G. & Ramponi, R. *Femtosecond laser micromachining: photonic and microfluidic devices in transparent materials* (Springer Science & Business Media, 2012).
44. Keldysh, L. *et al.* Ionization in the field of a strong electromagnetic wave. *Sov. Phys. JETP* **20**, 1307–1314 (1965).
45. Chan, J., Huser, T., Risbud, S. & Krol, D. Structural changes in fused silica after exposure to focused femtosecond laser pulses. *Optics letters* **26**, 1726–1728 (2001).
46. Sakakura, M., Shimizu, M., Shimotsuma, Y., Miura, K. & Hirao, K. Temperature distribution and modification mechanism inside glass with heat accumulation during 250 kHz irradiation of femtosecond laser pulses. *Applied Physics Letters* **93**, 231112 (2008).
47. Dekker, P., Ams, M., Marshall, G., Little, D. & Withford, M. Annealing dynamics of waveguide Bragg gratings: evidence of femtosecond laser induced colour centres. *Optics express* **18**, 3274–3283 (2010).

48. Kanehira, S., Miura, K. & Hirao, K. Ion exchange in glass using femtosecond laser irradiation. *Applied Physics Letters* **93**, 023112 (2008).
49. Shimotsuma, Y., Kazansky, P. G., Qiu, J. & Hirao, K. Self-organized nanogratings in glass irradiated by ultrashort light pulses. *Physical review letters* **91**, 247405 (2003).
50. Glezer, E. N. & Mazur, E. Ultrafast-laser driven micro-explosions in transparent materials. *Applied Physics Letters* **71**, 882–884 (1997).
51. Bhardwaj, V. *et al.* Optically produced arrays of planar nanostructures inside fused silica. *Physical review letters* **96**, 057404 (2006).
52. Cerullo, G. *et al.* Femtosecond micromachining of symmetric waveguides at 1.5 μm by astigmatic beam focusing. *Optics letters* **27**, 1938–1940 (2002).
53. Cheng, Y. *et al.* Control of the cross-sectional shape of a hollow microchannel embedded in photostructurable glass by use of a femtosecond laser. *Optics letters* **28**, 55–57 (2003).
54. Watanabe, W., Note, Y. & Itoh, K. Fabrication of multimode interference waveguides in glass by use of a femtosecond laser. *Optics letters* **30**, 2888–2890 (2005).
55. Schaffer, C. B., Brodeur, A., Garcia, J. F. & Mazur, E. Micromachining bulk glass by use of femtosecond laser pulses with nanojoule energy. *Optics letters* **26**, 93–95 (2001).
56. Minoshima, K., Kowalewicz, A. M., Hartl, I., Ippen, E. P. & Fujimoto, J. G. Photonic device fabrication in glass by use of nonlinear materials processing with a femtosecond laser oscillator. *Optics Letters* **26**, 1516–1518 (2001).
57. Marshall, G. D., Williams, R. J., Jovanovic, N., Steel, M. & Withford, M. J. Point-by-point written fiber-Bragg gratings and their application in complex grating designs. *Optics express* **18**, 19844–19859 (2010).
58. Ams, M., Marshall, G. D., Dekker, P., Piper, J. A. & Withford, M. J. Ultrafast laser written active devices. *Laser & Photonics Reviews* **3**, 535–544 (2009).
59. Yariv, A. & Yeh, P. *Photonics: optical electronics in modern communications* (Oxford University Press New York, 2007).
60. Eaton, S. M. *et al.* Telecom-band directional coupler written with femtosecond fiber laser. *IEEE photonics technology letters* **18**, 2174–2176 (2006).
61. Eaton, S. M. *et al.* Spectral loss characterization of femtosecond laser written waveguides in glass with application to demultiplexing of 1300 and 1550 nm wavelengths. *Journal of Lightwave Technology* **27**, 1079–1085 (2009).

62. Chen, W.-J., Eaton, S. M., Zhang, H. & Herman, P. R. Broadband directional couplers fabricated in bulk glass with high repetition rate femtosecond laser pulses. *Optics express* **16**, 11470–11480 (2008).
63. Osellame, R. *et al.* Fabrication of 3D photonic devices at 1.55 μm wavelength by femtosecond Ti: Sapphire oscillator. *Electronics Letters* **41**, 315–317 (2005).
64. Kowalevicz, A., Sharma, V., Ippen, E., Fujimoto, J. G. & Minoshima, K. Three-dimensional photonic devices fabricated in glass by use of a femtosecond laser oscillator. *Optics letters* **30**, 1060–1062 (2005).
65. Sansoni, L. *et al.* Two-particle bosonic-fermionic quantum walk via integrated photonics. *Physical review letters* **108**, 010502 (2012).
66. Crespi, A. *et al.* Three-dimensional Mach-Zehnder interferometer in a microfluidic chip for spatially-resolved label-free detection. *Lab on a Chip* **10**, 1167–1173 (2010).
67. Minoshima, K., Kowalevicz, A. M., Ippen, E. P. & Fujimoto, J. G. Fabrication of coupled mode photonic devices in glass by nonlinear femtosecond laser materials processing. *Optics Express* **10**, 645–652 (2002).
68. Li, G., Winick, K. A., Said, A. A., Dugan, M. & Bado, P. Waveguide electro-optic modulator in fused silica fabricated by femtosecond laser direct writing and thermal poling. *Optics letters* **31**, 739–741 (2006).
69. Knill, E., Laflamme, R. & Milburn, G. J. A scheme for efficient quantum computation with linear optics. *Nature* **409**, 46–52 (2001).
70. Politi, A., Cryan, M. J., Rarity, J. G., Yu, S. & O'Brien, J. L. Silicon-silicon waveguide quantum circuits. *Science* **320**, 646–649 (2008).
71. Marshall, G. D. *et al.* Laser written waveguide photonic quantum circuits. *Optics express* **17**, 12546–12554 (2009).
72. Sansoni, L. *et al.* Polarization entangled states measurement on a chip. *Physical Review Letters* **105**, 200503 (2010).
73. Crespi, A. *et al.* Integrated photonic quantum gates for polarization qubits. *Nature communications* **2**, 566 (2011).
74. Corrielli, G. *et al.* Rotated waveplates in integrated waveguide optics. *Nature communications* **5** (2014).
75. Heilmann, R., Gräfe, M., Nolte, S. & Szameit, A. Arbitrary photonic wave plate operations on chip: Realizing Hadamard, Pauli-X, and rotation gates for polarisation qubits. *Scientific reports* **4** (2014).
76. Owens, J. O. *et al.* Two-photon quantum walks in an elliptical direct-write waveguide array. *New Journal of Physics* **13**, 075003 (2011).

77. Poullos, K. *et al.* Quantum walks of correlated photon pairs in two-dimensional waveguide arrays. *Physical review letters* **112**, 143604 (2014).
78. Tillmann, M. *et al.* Experimental boson sampling. *Nature Photonics* **7**, 540–544 (2013).
79. Scheel, S. Permanents in linear optical networks. *ArXiv e-prints*. arXiv: [quant-ph/0406127 \[quant-ph\]](#) (2004).
80. Corrielli, G. *Integrated photonic circuits by femtosecond laser writing for qubit manipulation, quantum cryptography and quantum-optical analogies* PhD thesis (Politecnico di Milano, 2015).
81. Killi, A. *et al.* High-peak-power pulses from a cavity-dumped Yb: KY (WO₄)₂ oscillator. *Optics letters* **30**, 1891–1893 (2005).
82. Killi, A. & Morgner, U. Solitary pulse shaping dynamics in cavity-dumped laser oscillators. *Optics express* **12**, 3397–3407 (2004).
83. Hunsperger, R. G. *Integrated optics: theory and technology* 6th ed. (Springer-Verlag New York, 2009).
84. Szameit, A. *et al.* Two-dimensional soliton in cubic fs laser written waveguide arrays in fused silica. *Optics express* **14**, 6055–6062 (2006).
85. Clements, W. R., Humphreys, P. C., Metcalf, B. J., Kolthammer, W. S. & Walsmley, I. A. Optimal design for universal multiport interferometers. *Optica* **3**, 1460–1465 (2016).
86. Mezzadri, F. How to generate random matrices from the classical compact groups. *ArXiv Mathematical Physics e-prints*. arXiv: [math-ph/0609050](#) (2006).
87. Popović, M. A., Ippen, E. P. & Kärtner, F. X. Universally balanced photonic interferometers. *Optics letters* **31**, 2713–2715 (2006).
88. Eaton, S. M. *et al.* Heat accumulation effects in femtosecond laser-written waveguides with variable repetition rate. *Optics Express* **13**, 4708–4716 (2005).
89. Szameit, A., Dreisow, F., Pertsch, T., Nolte, S. & Tünnermann, A. Control of directional evanescent coupling in fs laser written waveguides. *Optics express* **15**, 1579–1587 (2007).
90. Crespi, A. *Integrated optical circuits for biosensing and quantum information by femtosecond laser microfabrication* PhD thesis (Politecnico di Milano, 2011).
91. Lloyd, S. Quantum enigma machines. *ArXiv e-prints*. arXiv: [1307.0380 \[quant-ph\]](#) (2013).
92. Yariv, A. & Yeh, P. *Optical waves in crystals* (Wiley, New York, 1984).